UNIVERSITY OF THE
WITWATERSRAND,
JOHANNESBURG

SUPERCAPACITIVE PERFORMANCE OF NICKEL(II) TETRAPYRAZINOPORPHYRAZINE MODIFIED TITANIUM CARBIDE NANOSHEETS

Thokozani Tsoari

1892706

Supervisor: Prof. Kenneth Ikechukwu Ozoemena

A dissertation submitted to the Faculty of Science, University of the Witwatersrand, in partial fulfilment of the requirements for the degree of Master of Science

April 2021

Johannesburg, South Africa

CANDIDATE'S DECLARATION

I declare that this dissertation is my own, unaided work. It is being submitted for the Degree of Master of Science at the University of the Witwatersrand, Johannesburg. It has not been submitted before for any degree or examination at any other University.

_____

(Signature of candidate)

28th day April of 2021 at Braamfontein, Johannesburg, Gauteng, South Africa

DEDICATIONS

To my loving parents Wonderboy Jacob Tsoari and Roseline Lindiwe Tsoari, whose unconditional love and endless sacrifices have enabled and propelled me to pursue my dreams. Mom and Dad, my expression of thanks will never be enough.

Thembekile Tsoari, my incredible, intelligent, beautiful, talented loving sister may this inspire you to believe in the beauty of your dreams and more and more as your soar higher and higher.

ALPHA & OMEGA

LORD YOU FINISH ALL THE GOOD WORK YOU START

CHI-EMEELA

ACKNOWLEDGEMENTS

I am utterly thankful to my Supervisor, Professor Kenneth Ikechukwu Ozoemena who has opened a door for me and allowed me the privilege of working under his guidance and expertise. Prof, your approach to work has challenged me and pushed me to personal growth in a manner I have never imagined. Thank you for your patience and sustained effort you have expended to expand me. Words can never fully express the role you have played in my life, Thank you Prof.

To my soulmate and lover, RefilweLerato Mokhatla, thanks so much babe for your presence throughout this journey. From the start you supported my intensions for doing it; within it, your encouragement and uplifting gestures when the going was tough; and right to the end your excitement for its completion as a success. You are amazing. I am super grateful to have you in my life.

Thembekile, this one is for you and me. Cheers to that. Thanks for your loving support, encouragement and pride in what I do. I have felt like an inspirational brother. Keep doing it, I love it! Honestly though, I love our love for education and support for each other. Dimpho Promise Motsepe, I do not think you know how helpful you were to me in making this a success. Your spaces and places were my definite backup when things were lit. Thanks for your chill and open arms. I appreciate you brother.

To my late brother and friend, Patrick Mahoana Leqola, I know you would have been glad to see the completion of this project. I miss you – may your soul rest in

eternal peace. This is my tribute. Your love for success and education was inspirational.

To my spiritual leadership, Bishop Tumo Isaac Mtimkhulu, servant of the Lord, your teachings gave me the courage and boldness to pursue this with definite faith that God finishes what He starts. Pastor Sonnyboy Mokoena, when you checked up on how I am doing with my studies and briefly quoted Philippians 4:13, reminding me that “I can do all things through Christ that strengthens me”, I was uplifted and got more strength to persevere through it all. Mpolokeng Mokoena, Boni & Oscar Maleke, thanks for rooting for me. To my youth leader and pastor, Dr Walter Phumzile Maqoma, my special thanks to you for understanding and always encouraging me to persist and finish off, to be honest, I felt accountable to you every time we would talk about my research. Your prayers in my lowest moments were a love gesture I keep and treasure in my heart, thank you so much.

To all my former National Petroleum Refiners of SA colleagues and Sasol Research and Technology role models and advisors, thank you for an instrumental role that you played in terms of exposure, advice and support. Dr. Nobuntu Mnqanqeni, Dr. Thabiso Phadi, Bongani Xaba, and Junino Moloto. Also, many thanks to the Air Products SA, Vanderbijlpark Laboratory team for the support. Mr Christo van der Mescht, Jabu Mabena, Lawrence Sithole and Kwesh Ramashapa, thank you.

My special thanks to my research group – Materials Electrochemistry and Energy Technologies & CATMAT - friends and associates I met along the way

- Postgrads: Dr. Funeka Nkosi – thanks so much my sister, Dr. Rasmita Barik, Dr. Guy Kabongo, I appreciate your assistance when I needed it most.
- Friends, associates, and colleagues who were helpful in many ways: Boitumelo Tlhaole, Lesego Gaolathle, Aderemi Haruna, Suhail Musa, Adam Schnier, Thomas Mongwe, Victor Mashindi, Prince, Pumza Mente, Tshwarela Kolokoto, Siwa Peteni, Dr Neo Pholosi, Palesa Mokoena, Lizzy Hadebe, Thalifane, Tsepo Tumedi, Irfan Habib, Thapelo Mofokeng, and many more.
- Special thanks to Dr. Sharonda Melchior who introduced me to MXenes and Nomthandazo Mabena for paving a way in working with Metallotetrapyrazinoporphyrazines

Nkosikhona 'Nazie' Nkosi, man I have found a friend and a brother in you. Dark days, bright days, all became good when we were together in person and over the phone during the hard lockdown. You're amazing bro!!!!

May I acknowledge the following academic leaders for the contribution to my work:

- Dr Carin Billing, for access to electrochemistry testing
- Prof Dave Billing, for access to the crystallography suite
- Dr Rudolf Erasmas, for Raman characterization
- Prof Alex Quandt for MERG sponsorship
- Prof. Neil Coville, for access to the CATMAT labs and equipment
- Prof. Yury Gogotsi, for the time you gave me and discussion of the MXene materials at the ISE 2019 Durban conference
- Drs Cebisa Linganiso, Zikhona Tetana, Manoko Maubane-Nkadimeng, MMU training for electron microscopy

- Mr David Moloto and Mr Famanda Valoyi for all the consumables and labware
- Ms Khwezi Ndawonde and Mary-Ann Xaba for administrative support
- Mrs Angel Kubheka and Manfred Molomo for finance allocation

I am grateful for the Materials of Energy Research Group (MERG) for their financial support through their scholarship.

ABSTRACT

Electrochemical capacitors are known to be energy storage devices with outstanding power delivery and uptake devices. Their prominent drawback is extremely low, and at best, modest energy density.. This research presents a new pathway into the exploration of two-dimensional materials as high energy electrode materials in symmetrical supercapacitor systems. We, for the first time in the reported history of MXenes and metallotetrapyrazinoporphyrazine complexes, report the combination of the lightest MXene, Ti_2CT_x, with nickel(II) tetrapyrazinoporphyrazine as active electrode material for supercapacitors in aqueous electrolyte to evaluate the resulting electrochemical performance. This novel composite was obtained by a simple intercalation of MXene via delamination by dissolved nickel(II) tetrapyrazinoporphyrazine. The rationale of this combination is to achieve synergized electrochemical performance through the intermix of unique respective properties from these materials: the metallic conductivity, capacitive, pseudocapacitive properties emanating from the surface physiochemistry of MXene nanosheets, and the redox catalytic activity of N4 metallo-macrocyclic complex. The electrochemical performance of alkaline, neutral, and acidic electrolyte systems is assessed by employing cyclic voltammetry, galvanostatic charge-discharge and electrochemical impedance spectroscopy. The highest obtained specific gravimetric capacitance is 109.5 F/g the nickel(II) tetrapyrazinoporphyrazine modified MXene. The broadest full cell operating window was 0.8 V for near-neutral based electrolyte. Full cells in basic media exhibited the most inferior performance in terms of stability as drastic capacitance fall off is observed after 2000 cycles.

TABLE OF CONTENTS

LIST OF FIGURES

Figure 7.8: Phase angle Bode plot of (a) MX, (b) MP-5/MX, (c) MP-15/MX, and (d) an overlay of respective materials in 1 M LiOH systems

LIST OF TABLES

LIST OF ABBREVIATIONS AND ACRONYMS

ESS:	Energy Storage Systems
EES:	Electrochemical Energy Storage
2D:	Two-Dimensional
SC:	Supercapacitor
EC:	Electrochemical Capacitor
EDLC:	Electric Double Layer Capacitor
PC:	Pseudo Capacitor
HC:	Hybrid Capacitor
Redox:	Reduction-Oxidation
RuO_2:	Ruthenium Oxide
GE:	General Electric
SOHIO:	Standard Oil Company of Ohio
NEC:	Nippon Electric Company
UPS:	Uninterruptable Power Systems
DC:	Direct Current
SMES:	Superconducting Magnetic Energy Storage
MN4:	Transition Metal-N_4 Complex
MX:	MXene (Ti_2CTx)
MP:	Metallotetrapyrazinoporphyrazine (NiTpyzTz)
MP-5:	5% Metallotetrapyrazinoporphyrazine (NiTpyzTz)
MP-15:	15% Metallotetrapyrazinoporphyrazine (NiTpyzTz)
MAX:	Metal A-Group Carbides/ Nitrides/ Carbonitrides
MXene:	Metal Carbides/ Nitrides/ Carbonitrides

EG: Ethylene Glycol

DMF: Dimethylformamide

NMP: N-Methyl-2-pyrrolidone

EtOH: Ethanol

PVDF: Polyvinylidene fluoride

CB: Carbon Black

AM: Active Material

MW: Microwave

PXRD: Powder X-ray Diffraction Spectroscopy

FTIR: Fourier-Transform Infrared Spectroscopy

UV: Ultraviolet

UV/Vis: Ultraviolet/Visible Spectroscopy

EPSW: Electrolyte Potential Stability Window

MW: Microwave

PXRD: Powder Diffraction X-Ray Spectroscopy

FTIR: Fourier-Transform Infrared Spectroscopy

XPS: X-Ray Photoelectron Spectroscopy

EDS: Elemental Dispersive X-Ray Spectroscopy

SEM: Scanning Electron Microscopy

TEM: Transmission Electron Microscopy

HR-TEM: High-Resolution Transmission Electron Microscopy

BET: Brunauer-Emmet Teller

TGA: Thermo-Gravimetric Analyzer

CV: Cyclic Voltammetry

GCD: Galvanostatic Charge-Discharge

CCCD: Constant Current Charge-Discharge

EIS: Electrochemical Impedance Spectroscopy

ESR: Equivalence Series Resistance

PEIS: Potentio-Electrochemical Impedance Spectroscopy

IUPAC: International Union of Pure and Applied Chemistry

JCPDS: Joint Committee on Powder Diffraction Standards

PDF: Powder Diffraction File

CPE: Carbon Paper Electrode

UNITS AND SYMBOLS

V	-	volt
F	-	farad
W	-	watt
Wh	-	watt-hour
J	-	joule
A	-	ampere
s	-	second
g	-	gram
kg	-	kilograms
h	-	hour
A.u.	-	Arbitrary Units
Ω	-	ohm
˚C	-	degrees Celsius
Å	-	angstrom
Hz	-	hertz
mm	-	millimetre
ω	-	angular frequency
eV	-	electronvolt

LIST OF EQUATIONS

(3.8) Symmetrical specific gravimetric capacitance

(3.9) Equivalence series resistance computation from constant current charge-discharge plots

(3.10) Cell energy density

(3.11) Cell power density

(3.12) Cell maximum power

CHAPTER 1

INTRODUCTION

1.1. Research Motivation and Significance – Energy Transformation

The rapid evolution of technology, urbanization and current electrification progress have led up to a power-hungry and energy-dependent global society. The modern-day society relies hugely on various mobile and stationary power devices for transportation systems, construction equipment, industrial tools and residential electronic devices. Cumulatively, the insatiable appetite and indisputable reliance, coupled with the fast-growing global population, has caused a remarkable increase in the world's ever-growing energy consumption as presented on figure 1.1. This remarkable increase in consumption is projected to further increase in the near future. As a result of increased consumption and rising demand, power generation has rose to supply and meet the world's electrification needs. Unfortunately, in the global quest of developing a clean future, this increased generation is dominated by conventional power generation. These are power plants that use fossil fuels as their primary energy source creating a fossil fuel dominated energy mix that is non-renewable and has a set of negative impact and destructive implications for the society it aims to cater for [1-3].

(a) (b)

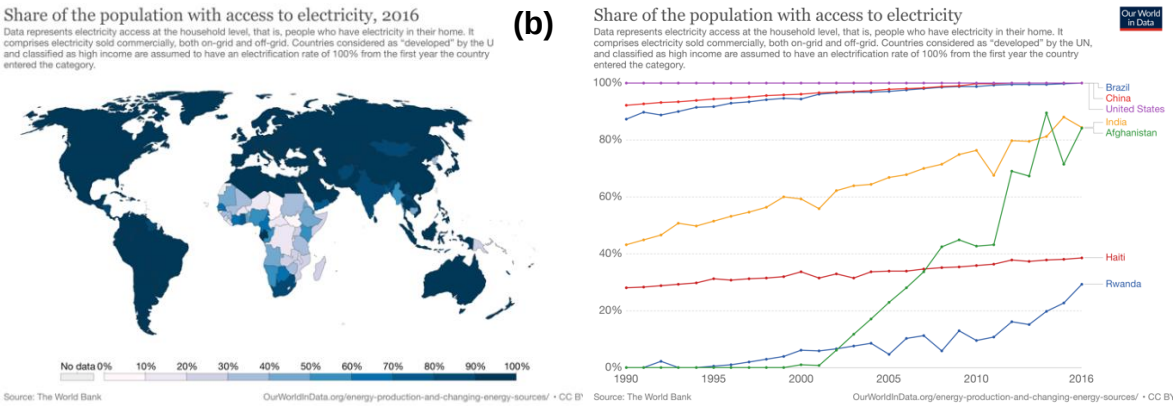

Figure 1.1: Share of the population with access to electricity at a household level in 2016 (a) map, (b) chart (Source: OurWorldInData.org/energy-production-and-changing-energy-sources)

The dominance of fossil fuel derived energy is a crucial concern for several reasons. Firstly, from an energy economics point of view, global crude oil and coal reserves are getting depleted whereas consumption is increasing [4]. This implies more demand and less supply; therefore, it is becoming more difficult and expensive for consumers to access power affordably. Secondly, with regards to the environment and sustainability, the pollution emitted by conventional generation systems threaten the health of the society and has adverse impacts on the ecosystem leading to global warming [3,5]. Thirdly, geopolitically, the abundance and lack of fossil fuel across different parts of the world has resulted to a socio-economic imbalance because of divisive political turmoil and volatile international relations - the powerful exploit and monopolize natural resources to oppress technically lacking countries and deprive the less privileged societies from having power resulting in socio-economical plagues propagated by energy-poverty [5,6].

To overcome this set of challenges, a viable solution is not possible without exploring and advancing renewable and sustainable energy. To minimize pollution,

the harnessing of decarbonized energy is necessary [3]. For socio-economical inclusion of the energy-impoverished societies and covering their increasing energy deficit, decentralized power generation through locally harvested energy from the free wind and sun is a propitious avenue. Moreover, efficient energy management for the growing generation and demand requires digitization of the power grid.

These three pushes - decarbonization, decentralization, digitization - also referred to as ‘energy transformation mega-trends’ as shown on Figure 1.2, are effectively advancing the transformation of the energy landscape. The need for energy devices that can optimally facilitate the implementation of renewable energy sources as viable power producers and complement their intrinsic intermittent characteristics is thus urgent [7].

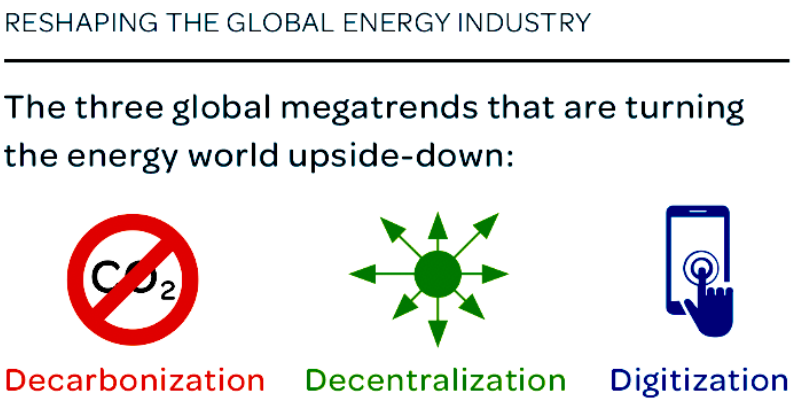

Figure 1.2: Three Ds of energy (source: https://inform.tmforum.org/features-and-analysis/2016/11/enabling-smart-energy-communities/)

1.2. Energy Storage Systems

Energy storage plays a crucial role in the renewable and sustainable energy supply chain. The primary function of energy storage systems (ESS) for renewable energy application is to capture the energy harvested from the wind, sun, hydropower and tidal power amongst other sources at the time of production and release it when there is a demand. The secondary function is their broad application in grid stability, improvement of energy management efficiency, and facilitation of renewable energy harnessed power merge with conventional power as a step towards mitigating the adverse environmental effects of fossil fuels [8].

ESSs may be divided into 5 main categories [9,10] such as

1. Electrical,
2. Mechanical,
3. Thermal energy storage,
4. Chemical, and
5. ***Electrochemical*** - this work is focussed on this class.

The above classes of energy storage systems have unique roles in terms of application based on their respective capabilities, properties and different levels of maturity as applicable cost-effective technological solutions. In the past, almost three decades ago, the scientific effort to advance renewable and sustainable energy has spurned extensive research and development into exploring electrochemical energy storage (EES) technologies. This class of energy storage and delivery technology is comprised of batteries, fuel cells, and electrochemical

capacitors. EES devices store electrical energy in chemical form and release it as electrical energy [10]. They have become a hot research subject and have attracted a great deal of research attention because of the central role devices in this class already play in addressing the energy transformation megatrends and the potential they undertake to revolutionize the energy landscape.

In decarbonization, the environmentally friendly electrochemical generation as well as the storage of renewable energy harvested power for stable load transmission - not characteristic of the intermittency in the wind and sun energy generation - is made possible by these powerful energy devices. Also, in decentralization, fast harvesting and portable, remote, off the grid storage of renewable energy is made possible by EES. Lastly, in digitization, the regulation of power supply at peak demand requires technologically controllable, fast, powerful, high energy advanced devices [7,8].

In the array of EES technologies, batteries and electrochemical capacitors find application widely in consumer electronics, transportation, and wearable technology to name a few. Batteries and electrochemical capacitors convert chemical energy into electrical energy. This conversion process occurs when two chemical reaction partners undergo a chemical reaction. Electric current results as these chemical reactions occur and can be defined at a specific time and voltage [10,11].

In the pursuit of overcoming the low density and high-cost challenge of pseudocapacitors, cost-effective, new two-dimensional (2D) nanomaterials have attracted significant attention due to their large electrochemically active surface

areas [12]. Their electroactive nature can be developed to apply them as pseudocapacitive electrode materials for supercapacitors. On this basis, this research is focused on improving the pseudocapacitive storage activity of two-dimensional titanium carbide (Ti_2CT_x) obtained by in-situ HF wet-chemical etching and introducing nickel(II) tetrapyrazinoporphyrazine into the layered material matrix for pseudocapacitive electrode material in aqueous media.

We hypothesize that: if the physiochemical modification of two-dimensional nanomaterials used as supercapacitor electrodes can improve the electrochemical performance of supercapacitors, MXene layered material modified with a metallotetrapyrazinoporphyrazine complex as an intercalant will exhibit a structural, chemical, electronic and mechanical synergistic effect for better electrochemical performance when used as supercapacitor electrodes in various aqueous electrolyte.

1.3. Research Questions

This research work is set out to answer the following questions:

I. How does the nickel(II) tetrapyrazinoporphyrazine incorporated Ti_2CT_x compare to the pristine Ti_2CT_x in terms of electrochemical performance in supercapacitors?
II. What effect does the nitrogen-rich organic macrocyclic dopant have on the crystal structure of MXene?
III. Can a correlation between the structural properties, physiochemical properties, and electrochemical performance be established from the nickel(II) tetrapyrazinoporphyrazine/MXene composites?

1.4. Research Aim and Objectives

Aim

To investigate the supercapacitive effects of MN4 macrocyclic complex integrated MXene nanosheets on the electrochemical performance for supercapacitors

Objectives

The overarching objectives of this research are:

I. High quality synthesis of nickel(II) tetrapyrazinoporphyrazine integrated Ti_2CT_x

II. To investigate the effect of nickel(II) tetrapyrazinoporphyrazine on MXene physiochemical properties

III. To investigate the electrochemical performance of nickel(II) tetrapyrazinoporphyrazine-modified MXene used when used as electrodes in symmetric supercapacitors

IV. To establish a correlation between the material structural properties, and electrochemical performance

V. To investigate the effects of acidic, neutral, and alkaline aqueous electrolyte on electrochemical performance

1.5. Reference List

[1] United States Department of Energy. (2019). 'International energy outlook 2019 with projections to 2050', pp32. Available at: https://www.eia.gov [accessed at 19 November 2019].

[2] United Nations Development Programme. (2016). 'UNDP support to the implementation of sustainable development goal 7 – affordable and clean energy', pp 1-97 Available at: https://www.undp.org [accessed at 13 October 2018].

[3] Gielena, D., Boshella, F., Saygin,D., Bazilian, M.D., Wagnera, N., and Gorini, R., (2019) 'The role of renewable energy in the global energy transformation', *Energy Strategy Reviews*, 24(January), pp. 38–50. doi: 10.1016/j.esr.2019.01.006.

[4] Dunn, B., Kamath, H., and Tarascon, J.-M. (2011) 'Electrical Energy Storage for the Grid: A Battery of Choices', *Science*, 334(6058), pp. 928–935. doi: 10.1126/science.1212741.

[5] World Energy Council (2017) 'World Energy Issue Monitor 2017', p. 156. Available at: https://www.worldenergy.org/wp-content/uploads/2017/04/1.-World-Energy-Issues-Monitor-2017-Full-Report.pdf [accessed at: 13 October 2018].

[6] Lloyd, P., Cowan, B., and Mohlakoana, N. (2004). 'Improving access to electricity and stimulation of economic growth and social upliftment', *Improving Access to Modern Energy Services through CDM and Technology Transfer conference*. Eskom Conference Centre, 27-29 July 2004. University of Cape Town: Energy Research Centre.

[7] Di Silvestre, M. L., Favuzza, L., Sanseverino, E.L., and Zizzo, G. (2018). 'How Decarbonization, Digitalization and Decentralization are changing key power infrastructures', *Renewable and Sustainable Energy Reviews. Elsevier*, 93(February), pp. 483–498. doi: 10.1016/j.rser.2018.05.068.

[8] Aneke, M. and Wang, M. (2016). 'Energy storage technologies and real-life applications – A state of the art review', *Applied Energy. Elsevier*, 179, pp. 350–377. doi: 10.1016/j.apenergy.2016.06.097.

[9] Koohi-Fayegh, S. and Rosen, M. A. (2020). 'A review of energy storage types, applications and recent developments', *Journal of Energy Storage. Elsevier*, 27(July 2019), p. 101047. doi: 10.1016/j.est.2019.101047.

[10] Schougaard, S. B., and Bélanger, D. (2014). 'Electrochemical energy storage systems' In: *Functional Materials: For Energy, Sustainable Development and Biomedical Sciences* (Edited by M. Leclerc and R Gauvin), De Gruyter, Berlin, Germany, 2014, Chapter 8, pp.171-188. doi.org/10.1515/9783110307825.171

[11] Simon, P., Gogotsi, Y., and Dunn, B. (2014) 'Where Do Batteries End and Supercapacitors Begin?', *Science*, 343(6176), pp. 1210–1211. doi: 10.1126/science.1249625.

[12] Kumar, P., Abuhimd, H., Wahyudi, W., Li, M., Ming, J., and Li, L-J. (2016) 'Review—Two-Dimensional Layered Materials for Energy Storage Applications', *ECS Journal of Solid State Science and Technology*, 5(11), pp. Q3021–Q3025. doi: 10.1149/2.0051611jss.

CHAPTER 2

LITERATURE REVIEW

2.1. Supercapacitors

Supercapacitors, also known as ultracapacitors or electrochemical capacitors, are an important and evolving class of energy storage devices. Their incredible properties distinguish them as important for advancing the global clean energy agenda. Therefore, extensive research has been concerted in their direction for establishing new knowledge and elevating their design for better performance and advanced application [1-5]. In the following subsections, the classification, properties, brief history, and fundamentals of supercapacitor devices will be laid out.

2.1.1. General Classification of Supercapacitors

Supercapacitors are a class of energy storage systems comprised of electrochemical double layer capacitors, pseudocapacitors and hybrid capacitors [1]. Figure 2.1 shows the common classes of capacitors and the electrode materials commonly applied for each class [5].

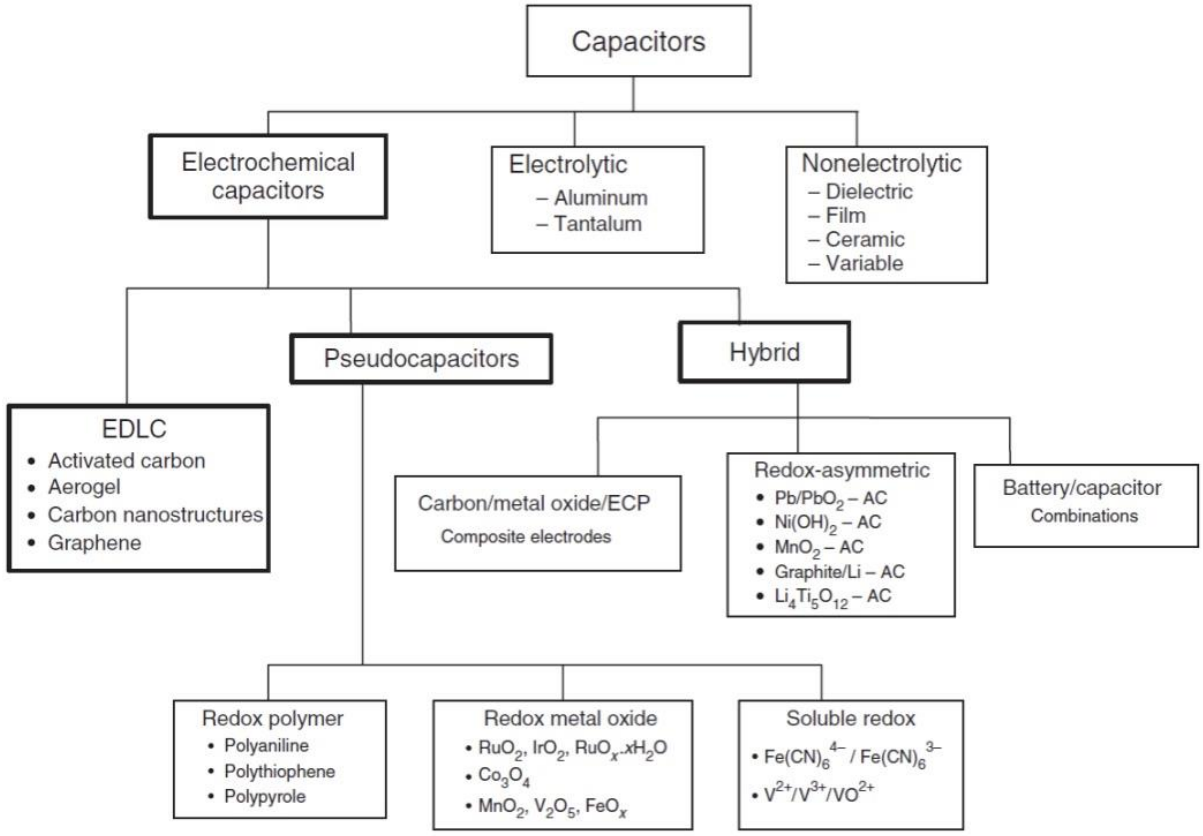

Figure 2.1: Common classes of capacitors [5]

The classification of these devices is based on the charge storage mechanisms which to a great extend depends on electrode material and electrolyte [1-3]. Primarily, these mechanisms emerge as a result of the type of electrode materials used in the device and their interaction with electrolyte species. Figure 2.1 also shows commonly used materials for respective capacitor categories. Section 2.4 is devoted for the discussion of supercapacitor energy storage mechanisms. In table 2.1, a general comparison of electric double layer capacitors (EDLCs) and pseudocapacitors (PCs) is made in terms of electrode material, stability, and characteristic energy storage feature.

Table 2.1: Comparison between EDLCs and PCs

Comparison Parameters	**Electric Double Layer Capacitors**	**Pseudocapacitors**
Electrode Material	High specific surface area	Conducting polymers, metal oxides
Stability	High chemical and cycling stability	Poor mechanical stability
Energy Storage	Electrostatic	Faradaic reactions

2.1.1.1. Electric Double Layer Capacitors

Electric double layer capacitors are commonly constructed with high surface area, electrically conductive and electrochemically stable materials such as activated carbon, carbon nanostructures, graphene and aerogel [4]. EDLC are based on an electric double layer capacitance mechanism. This mechanism type is a physical phenomenon that occurs when two charged layers are formed at the electrically charged electrode surface and the electrolyte interface. Electric double layer happens when a charged object is immersed into a liquid and counter charged ions in the liquid are adsorbed on the surface of the electrode [2-3]. This mechanism will be further expounded on in section 2.5.1.

2.1.1.2. Pseudocapacitors

Pseudocapacitors are a class of supercapacitors that store charge based on fast, reversible reduction-oxidation (redox) reactions that occur on the electrolyte/electrode interface. Common materials used as electrode materials are

transition metal oxides and redox polymers [3]. An excellent, electroactive electrode material which is commercially and widely used for pseudocapacitors to date is ruthenium oxide (RuO_2) because of its impressive properties such as good conductivity and redox reversible surfaces when hydrated. Unfortunately, its high cost, toxicity and unsuitability for microscale device applications has directed research into the exploration of other electroactive, mechanically strong, high surface area materials such as electronically conducting polymers, doped graphite-based materials, and transition metal dicalchogenides, carbides, nitrides and carbonitrides as alternatives [1-3].

2.1.1.3. Hybrid Capacitors

Hybrid capacitors (HCs) are supercapacitors that employ an asymmetric electrode configuration to store charge. This configuration enables these devices to synergize on the properties of both EDLC and PC for an extended operation potential and capacitance [2-5].

2.1.2. History of Supercapacitors

Historically, the invention of capacitors dates back to the 1745-1746. In fact, the invention of the battery was in 1800 had its origin in the use of the then capacitors known as Leyden jars. Leyden jars were known as electrical energy sources invented at the University of Leyden in Holland. It consisted of a glass jar that had a thin layer of silver coated inside and outside. When the outer foil was grounded, electrostatic generators or any source of static electricity could charge the inner foil and produce an electrical discharge [5]. Around 1920 a new class called electrolytic capacitor was invented. Between the period 1880 and 1924, three

models were developed through studies by von Helmholtz, Gouy-Chapman, and Stern to conceptualize charge storage in electrochemical capacitors. In 1957 the first electrochemical double layer capacitor for practical use was demonstrated and patented by H.I. Becker of General Electric (GE). This EDLC used activated charcoal as electrode material. In 1966, the Standard Oil Company of Ohio (SOHIO) established EDLC charge storage. In 1971, Nippon Electric Company (NEC) bought the licence and pseudocapacitance was discovered. A decade before the end of the 20th century, electrochemical capacitor research grew intensively due to the need of high-power energy storage devices for various technological developments at the time [5]. Since then, till today, as illustrated on Figure 2.2 [6] their application, research and development are on the rise to further develop the new generation devices that offer advanced power charge and discharge solutions.

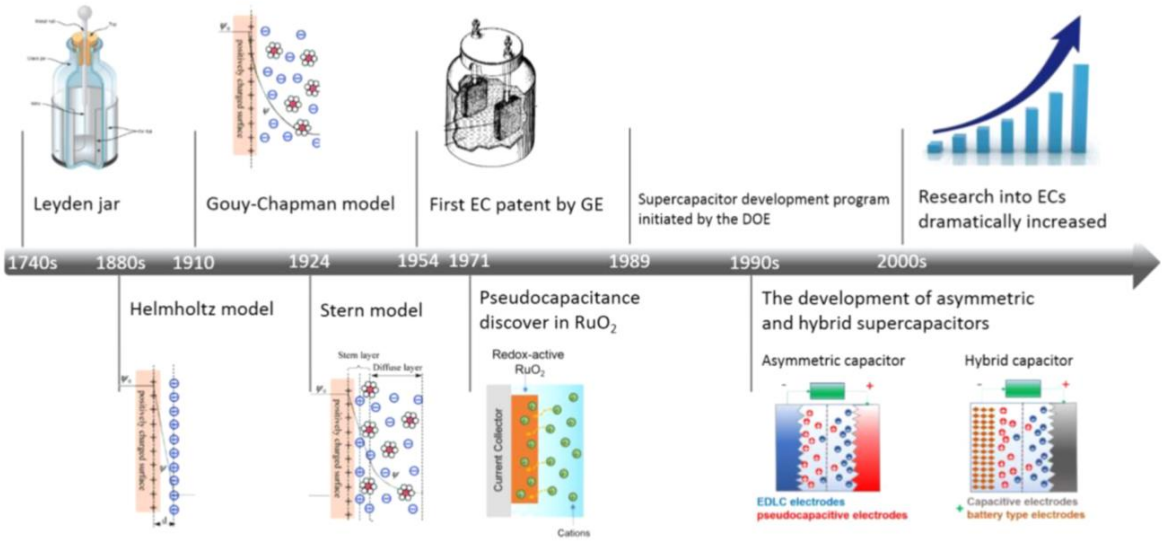

Figure 2.2: Historic timeline of supercapacitor development [6]

2.1.3. Supercapacitor Applications, Properties and Energy Storage Performance

2.1.3.1. Key Properties

Supercapacitors are known for their safety, reliability, extremely high-power density, long cycle life, low to no maintenance needs, and potentially developable energy density of supercapacitors [1-3].

2.1.3.2. Application Areas

Automotive: electric vehicle battery recharge, regenerative braking system, and start-stop systems [3].

Solar systems: power harvesting and load management (equalizer components) [3;7]

Military: Laser weapons, hybrid warfare vehicles, and electromagnetically controlled projectiles [8].

Power grid: power utility quality control (voltage and frequency) [3].

Household: uninterruptable power systems (UPS) and consumer electronics (digital cameras, laptops, phones, communication devices, tools) [9].

These areas of application are but an example and not an exhaustive list of important areas of supercapacitor applications. Commonly, supercapacitors are

used in complementary configurations with batteries. An example for such a complementation is: in a solar system when high power harvesting of energy from the sun is enabled by a supercapacitor-photovoltaic cell integrated system that stores energy in high energy density batteries is illustrated on Figure 2.3 [10].

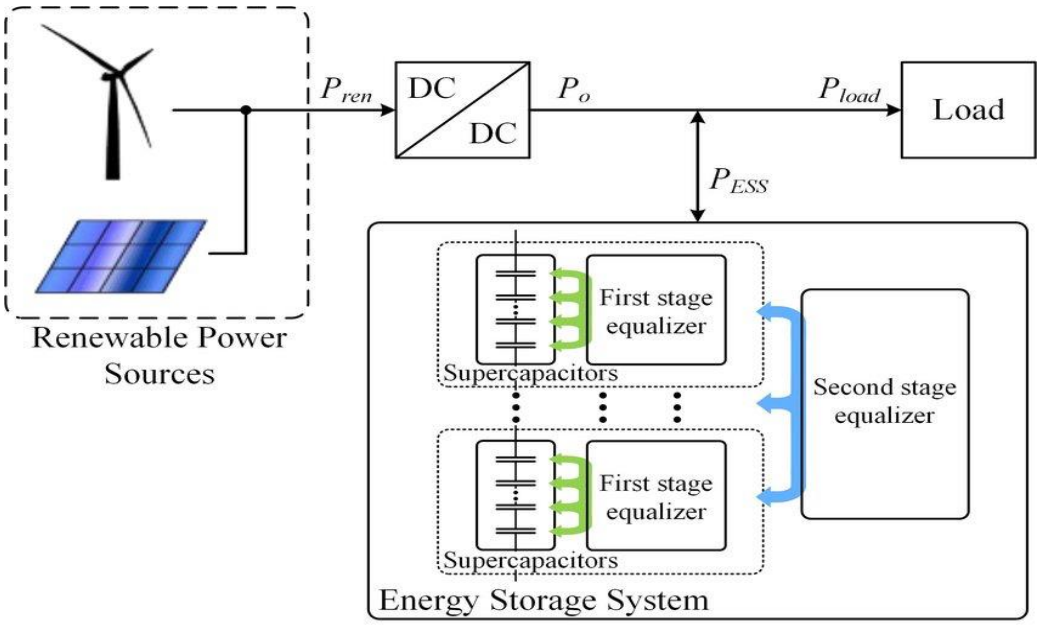

Figure 2.3: A schematic representation of the role supercapacitor play with equalizers in renewable energy storage systems [10]

2.1.3.3. Energy Storage Performance

The energy storage performance of supercapacitors is distinct from the features of other ESS, namely, batteries and conventional dielectric capacitors. Supercapacitors are positioned as intermediate power-energy density performers between conventional capacitors and batteries. Conventional capacitors have high power density but lower energy density while batteries have high energy density but relatively low power density. SC performance – energy density and power density - can be calculated using the following equations:

$$E = \frac{CV^2}{2} \qquad \textbf{(2.1)}$$

The energy (Wh/kg) stored in an electrochemical capacitor is expressed as proportional to the square root of the cell's operating voltage (V) and its capacitance (F)

$$P = \frac{V^2}{4R} \qquad \textbf{(2.2)}$$

P, Power maximum (W), according to equation 2.2 is proportional to V the square of the cells operating voltage window (V), and is inversely proportional to the product of the system's R, resistance (Ohms).

The below Ragone plots on Figure 2.4a [11] and 2.4b [12] depict the energy performance of various energy storage devices and the position that supercapacitors hold in the landscape of energy storage devices in terms of specific power and specific energy.

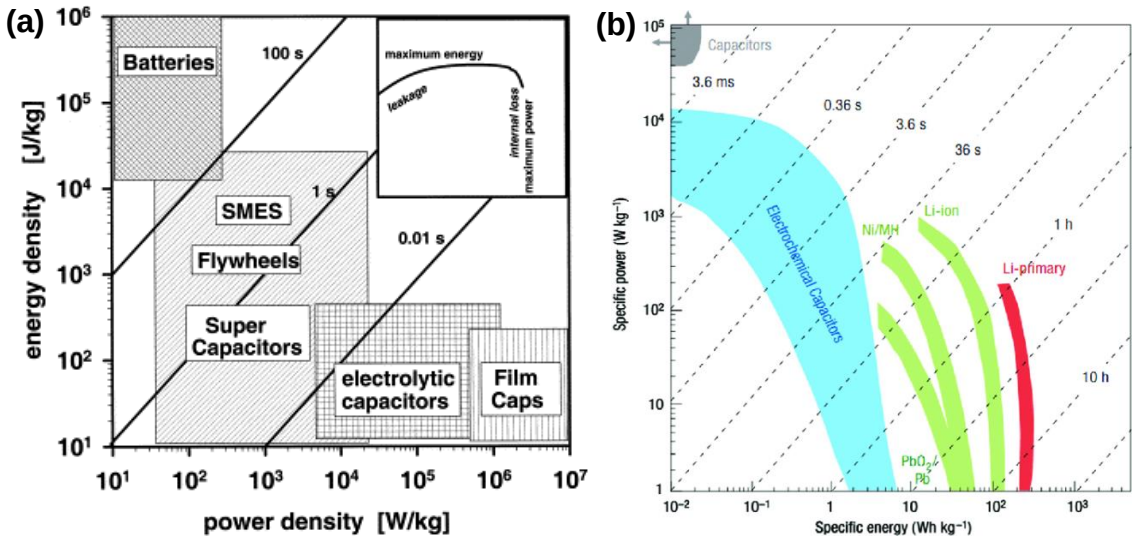

Figure 2.4: (a) Ragone plot: Different types of energy storage devices located in different regions with characteristic times corresponding to lines with unity slope [11]; (b) Ragone plot of different energy storage devices [12]

The energy storage performance metrics of supercapacitors compared to batteries are shown on table 2.2 as adapted from the work of. The specific energy density of supercapacitors is an order lower than that of batteries but has a higher specific power than batteries, and a longer lifecycle. Table 2.3 shows the summarized comparison in terms of the storage mechanism involved in energy storage, the source of power cycle life limitation, and the charge rate.

Table 2.2: Comparison table of Supercapacitors against and Batteries

Characteristics	**Supercapacitor**	**Battery**
Specific power (W/kg)	500 to 10 000	<1 000
Specific energy (Wh/kg)	1 to 10	10 to 100
Discharge time	s to min	0.3 to 3 h
Charge time	s to min	1 to 5 h
Coulombic efficiency (%)	85 to 98	70 to 85
Cycle-life	>500 000	About 1 000
Operating temperature (^{o}C)	-25 to +70	-20 to +60

Adapted from [2]

Table 2.3: Comparison of Batteries with Supercapacitors

Comparison Parameters	**Supercapacitor**	**Battery**
Storage Mechanism	Physical	Chemical
Power Limitation	Electrolyte conductivity	Mass transport, kinetics of the reaction
Energy Storage	Limited - surface area	High - bulk
Charge Rate	High charge and discharge rate	Limited by the kinetics
Cycle Life Limitation	Parasitic reactions	Mechanical instability, and irreversible cyclability

Based on the performance comparison metrics, the preferred use of batteries is applications that require high-energy; while for supercapacitors, it is for high power-demand applications as earlier showed on Figures 2.4. Alternatively, and often, as mentioned in the preceding subsection, the application of both devices – batteries and supercapacitors – [13] is a complementary one for applications that require a hybridized approach such as electric cars - both supercapacitors and batteries are complementary and central for the vehicle's energy supply amongst other functions.

The limitations of SCs, particularly EDLCs, mainly result from the electrical double layer charge storage mechanisms which is strictly limited to high surface area and specific pore sizes of the electrodes [2-4,9,15]. Another group of SCs are commonly known as pseudocapacitive supercapacitors or pseudocapacitors

(PCs). Unlike their EDLC counterparts where the storage of charge is predominantly achieved electrostatically, PCs, more like batteries, provide higher capacitance and energy due to their fast, reversible redox reactions at the electrode surface. However, this faradaic mechanism introduces mechanical changes to the electrode material such as swelling and shrinking resulting to chemical and physical instability, as well as capacity fading [2-4;6;9].

2.2. Supercapacitor Components

A supercapacitor cell is fundamentally comprised of four components, graphically illustrated on Figure 2.5:

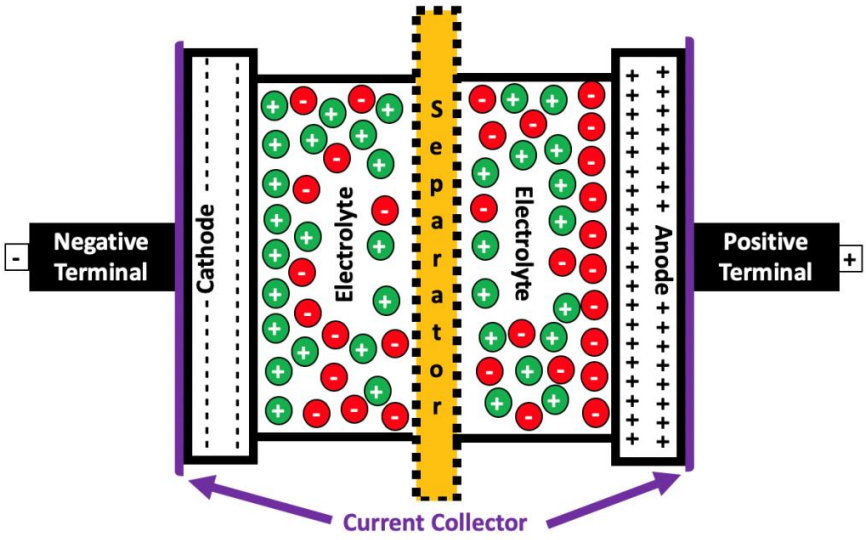

.

Figure 2.5: Supercapacitor cell schematic diagram

Electrodes

Electrodes play an extremely critical role in the substantial performance improvement of supercapacitor energy systems. These are advanced energy storage nanomaterials that are highly conductive. In a full cell configuration, they

can be symmetric or asymmetric. Their role is highly noticeable on capacitance, capacity, the energy and power density they effect on batteries and supercapacitors. Their chemistry, structural properties, electronic properties and surface morphology can be designed, optimized, and nanostructured to accentuate properties that make energy storage systems to be more efficient and powerful. Ideal electrodes materials are nanoporous materials with high electronic conductivity and high surface areas. [12]

Separator

A separator is an ion permeable, ion conductive, electron insulative material through which electrolyte ions charge transfer between electrodes. Separators prevent an electrical short circuit between electrodes and facilitate the balancing of charge between electrode materials. Commonly, ceramic or glass fiber separators are used for aqueous electrolyte-based systems, and polymers or paper for organic electrolyte systems [14].

Electrolyte

An electrolyte is a solution containing mobile ionic species. Electrolyte in supercapacitor systems play a crucial role that facilitates ion movement, as well as charge transfer and balancing between electrodes. Ideally, electrolytes should have high ionic conductance, wide voltage window, low solvated ionic radius, low viscosity, low toxicity, low volatility and availability at high concentrations.

They can be classified into three broad categories as presented on Figure 2.6. Our focus in this work is on all three subcategories of aqueous electrolyte: acidic (H_2SO_4), neutral (Li_2SO_4), and alkaline (LiOH).

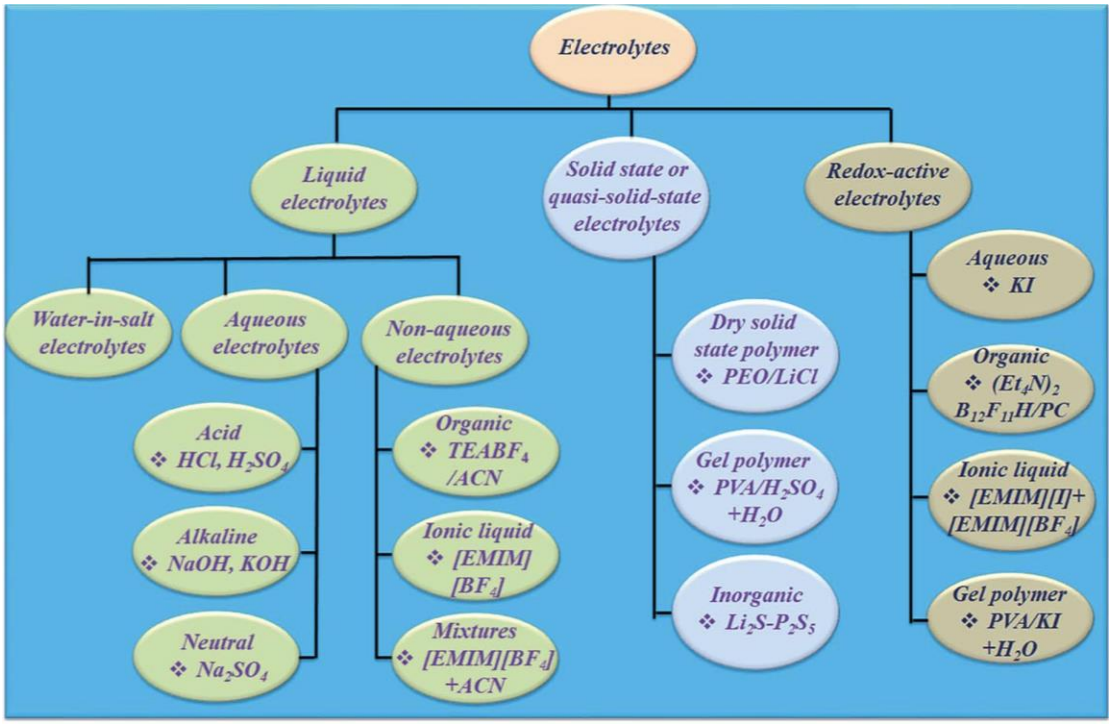

Figure 2.6: Classification of electrochemical capacitors electrolytes [17]

Aqueous electrolyte can be further classified into three categories: acidic, neutral, and alkaline. These three media have different effects on the charge storage mechanisms in electrochemical capacitors because of their chemistry, electronic and physical properties. In electrochemical capacitors-electrolyte studies, the ion interaction with the active material pores and deep-trap sites, the conductivity, ion size, and pH are properties that contribute to the redox and capacitive properties of electrochemical cells.

Aqueous electrolytes are a safer, environmental-friendly alternative to their non-aqueous counterparts. They are non-flammable, cost effective, have high-ionic conductivity, easy to synthesize, convenient to fabricate, and less harmful to the environment. However, the drawback to aqueous electrolyte is their narrow potential window in supercapacitor systems. It is known that water easily electrolyzes in aqueous electrolyte at 1.23 V thermodynamic potential window to form gases. Studies have shown that in certain materials, a synergistic effect can be observed as the chemistry of aqueous solvents combined with the hydrophilicity of materials to extend the electrolyte decomposition voltage. Voltage window in supercapacitor is an important parameter that determines energy storage as the storage of charge is proportional to the square of applied voltage.

Because electrochemical processes that govern charge storage and device performance largely depend on the electrolyte/electrode interaction, finding a well-suited electrolyte for materials employed as electrode materials in search of novelty is a crucial step [14-17].

Current Collectors

Materials serving as a power connection between the electrode and external terminals of an electric circuit. Materials used as current collectors range from overcapacitive carbon fiber, to nickel foam, and aluminum foil [3;9].

2.3. Supercapacitor Operating Principles

Electrochemical capacitors operate on the same principles as conventional dielectric capacitors. The most fundamental understanding of supercapacitors is

that they are an electrochemical energy storing energy devices that operate on a simple, general mechanism of electrolyte ions adsorbing onto the electrode surface [3]. On application of a voltage between the supercapacitor electrodes, charge is stored on the polarized electron rich and electron deficient electrodes by adsorption of bulk electrolyte solution ions. This charge is balanced by the migration of anions and cations to their counter polarized electrode surface. The uniqueness of supercapacitors is underpinned by this highly reversible adsorption/desorption process.

Basically, the operation mechanism for supercapacitors can either be electrostatic (non-faradaic) or redox (faradaic) [4]. In practice, both mechanisms are at play and contribute to different extents to energy storage and discharge. A schematic depiction on Figure 2.7 illustrates what happens upon charge and discharge.

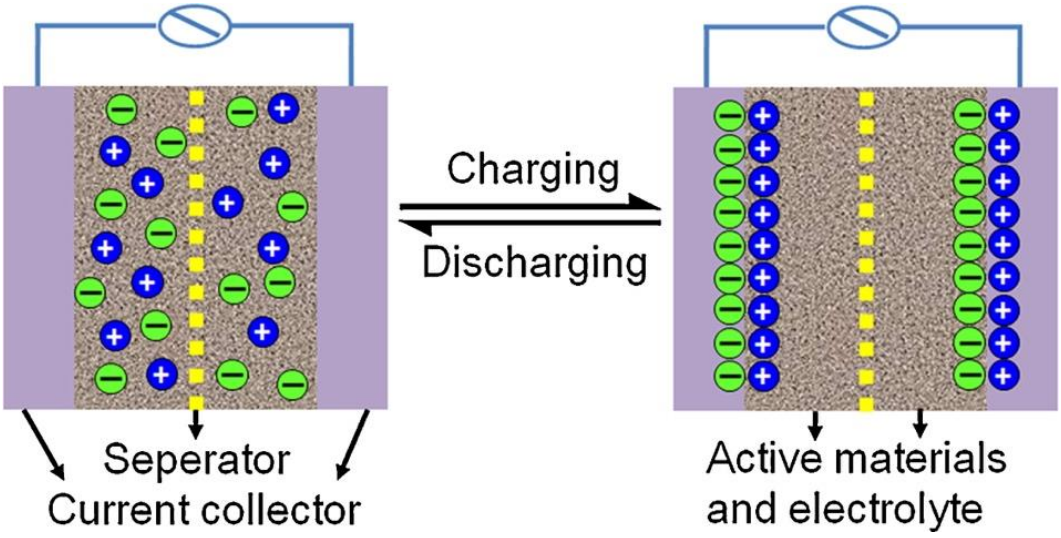

Figure 2.7: Schematic representation of what happens upon supercapacitor charge/discharge process [18]

Upon charge, a potential difference is applied across the electrodes. The applied voltage effects a migration of positive and negative charges towards electrode

surfaces of opposite polarities. For discharge, an external circuit allows a capacitor device to release energy at a voltage instantaneously.

According to first principles of supercapacitor energy storage, energy density depends on capacitance and the operational voltage of the cell [1]. Hence, to improve the efficiency of cell performance, two approaches can be taken, (i) design of novel materials to improve capacitance, or (ii) broaden the cell potential by employing electrodes of different voltage properties in suitable electrolyte. These two approaches are not exclusive as the combination of both approaches is more wholistic in designing a cell. Fittingly, the key features that are vital for the electrode of a supercapacitor are cyclability, stability, high surface area and electronic conductivity should be well matched with current collectors and electrolyte that maximize the performance of the overall cell [1-6].

2.4. Supercapacitor Mechanisms

Surface reactions of electrode materials determine the capacitance of supercapacitors. These reactions occurring at the electrode/electrolyte interface can be classified as two behaviours (faradaic or non-faradaic). Although these mechanisms co-exist in a supercapacitor device, the extent to which they do determines the categorization of supercapacitors and can further be classified into three (the third one being the combination of the first two). Figure 2.8 [51] shows the capacitive and pseudocapacitive storage systems and their respective electrochemical responses [9,19].

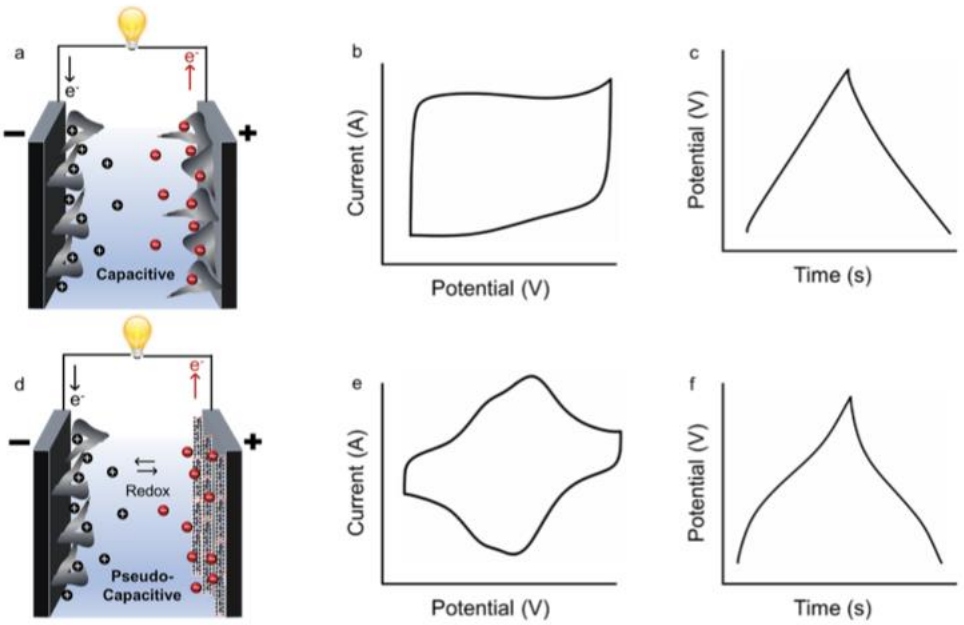

Figure 2.8: Charge storage mechanism and their electrochemical response in (a-c) EDLCs; (d-f) pseudocapacitors [51]

2.4.1. Electric Double Layer Capacitance Mechanism

In the electrostatic charge storage mechanism, ion charge is accumulated and stored at the electrode-electrolyte interface as ***electric double layer capacitance*** by the reversible adsorption/desorption of the electrolyte ionic species. No faradaic reactions are involved in this process. This type of capacitance is specific surface area dependent. As a result, capacitance in EDLC is limited and much lower than in pseudocapacitors. Materials with high surface area such as porous carbon have found extensive use for EDLC application [1-5].

Capacitance (C) is a proportionality constant that relates the Charge (Q) stored on each electrode to Potential difference (V) that exists between them. This relationship describes EDLC and is expressed as:

$$C_{dl} = \frac{Q}{V} = \frac{\varepsilon_r \varepsilon_o A}{d} \qquad \textbf{(2.3)}$$

Where: Cdl is the EDL capacitance of a single electrode in Farads (F), Q is the total charge in Coulombs (C), V is potential in Volts (V), Er is the dielectric constant, Eo is the vacuum dielectric constant, d is the distance between two electrode surfaces, and A is the electrode surface area

The charge current response *I* can be derived from equation 2.3 when Cdl is constant according to the following equation:

$$I = \frac{dQ}{dt} = Cdl\ \frac{dV}{dt} \qquad (2.4)$$

Where t is the charge time. The relationship between the applied voltage and its linear variation with time is known to be expressed as V = V0 + Vt (V0: initial voltage, and Vt: final voltage)

There are three models that conceptualize EDLC: (i) Helmholtz, (ii) Gouy-Chapman, and (iii) Stern model (graphically illustrated on Figure 2.9). These models are below discussed in the order of their chronological development and scientific correct description of the interphase structural processes involved in EDLC.

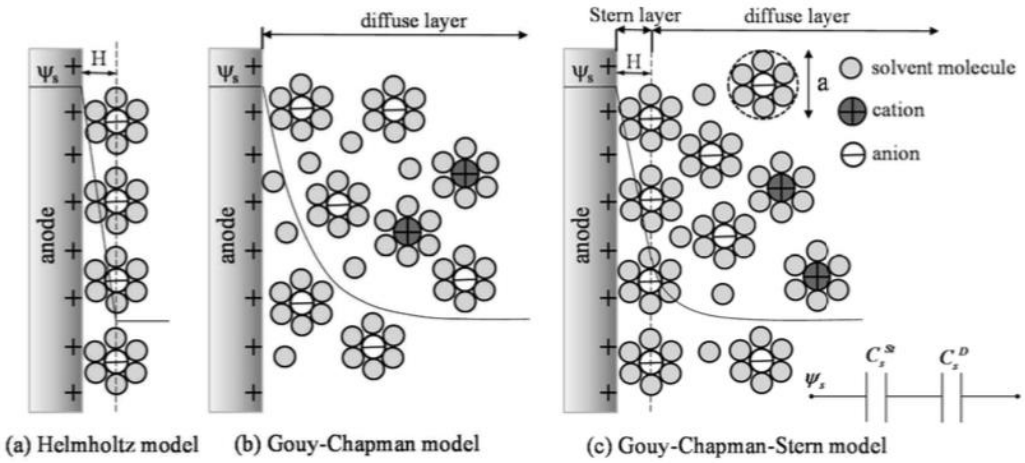

Figure 2.9: Schematics of the electric double layer structure showing the arrangement of solvated anions and cations near the electrode/electrolyte interface in the Stern layer and the diffuse layer. (a) Helmholtz model; (b) Gouy–Chapman model; and (c) Gouy–Chapman–Stern model. [20]

2.4.1.1. Helmholtz Model

The Helmholtz model is known to be the first, dated 1853, and simplest model to be developed for the purpose of providing insight of how energy is accumulated and discharged in EDLC. Helmholtz suggested that when an electrode is immersed in an ionic electrolyte solution, a double layer will form between the electrode and electrolyte surface as described on Figure 2.4a. This layer is based on the redistribution of electrolyte charged species as they adsorb on the oppositely charged electrode to balance the charge density of the electrode. As a result, a non-faradaic double layer is formed, there is a potential difference established between the surface of the electrode and the electrolyte inner boundary. The separation between the adsorbed electrolyte ions and the electrode surface is atomic thin as the ions lose the solvation shell as they adsorb onto the surface of material. According to Gouy-Chapman this model was not sufficient to conceptualize the

charge/discharge mechanism of EDLC as it did not consider the adsorption of water molecules and electrolyte ions. This proposed model was centred on 'Diffusion layer' [20-22].

2.4.1.2. Gouy-Chapman Model

In their work, Gouy and Chapman, a model to further develop the interfacial mechanism that occurs on the electrode/electrolyte interface in capacitors was proposed. This is also known as a diffusion layer model and refers to the thermal motion of the electrolyte bulk solution near a charged electrode surface. As opposed to the Helmholtz model, counterions of the electrolyte solution are proposed to not be closely lined up on the oppositely charged electrode but are randomly diffused in the solution bulk depending on amongst other factors, temperature. This distribution is referred to as the Botzmann-Poisson distribution equation. So, the general assumption in this model is that ions are point charges and exists in the diffuse layer. Therefore, the distribution of capacitance is not constant but varies as function of potential. The inaccuracy with this method is it led to an overestimated capacitance [20-22].

2.4.1.3. Stern Model

The Stern model was developed in 1924. This model, simply put, describes charge storage as a combination of the Helmholtz and Gouy-Chapman model. It has been considered as the most realistic and scientifically correct model to explain the charge storage mechanism involved in EDLC and is also known as Gouy-Chapman-Stern model. In theory, this model forms basis and is known to be the cornerstone of modern theoretical electrochemistry for over a century. As

a result, it has been accepted to approximate that the total capacitance (C_t) of EDL arises from both the Helmholtz layer capacitance (C_H) and Gouy-Chapman layer capacitance (C_{diff}), mathematically expressed in equation 2.5 [1,20-22]

$$\frac{1}{C_t} = \frac{1}{C_H} + \frac{1}{diff} \qquad \textbf{(2.5)}$$

where C_t is the total capacitance, C_H is the Helmholtz layer Capacitance, and C_{diff} is the diffuse double layer capacitance according.

2.4.2. Pseudocapacitance Mechanism

In the faradaic mechanism, charge is stored by thermodynamically and kinetically favoured reversible, fast reduction-oxidation and/or electrosorption reactions at or near the surface of the electrode/electrolyte interface as ***pseudocapacitance***. Pseudocapacitance refers to a capacitance that has similar likelihood of capacitance but differs to it on how capacitance is produced. This type of mechanism leads to a higher energy density. Materials that are known to demonstrate pseudocapacitance have been transition-metal oxides and conductive polymers over the years. Interestingly, pseudocapacitive materials have provided significantly more specific capacitance than capacitive materials [24].

Pseudocapacitance can be classified into three categories as depicted in Figure 2.10 [25]: (i) underpotential deposition, (ii) redox pseudocapacitance, and (iii) intercalative pseudocapacitance.

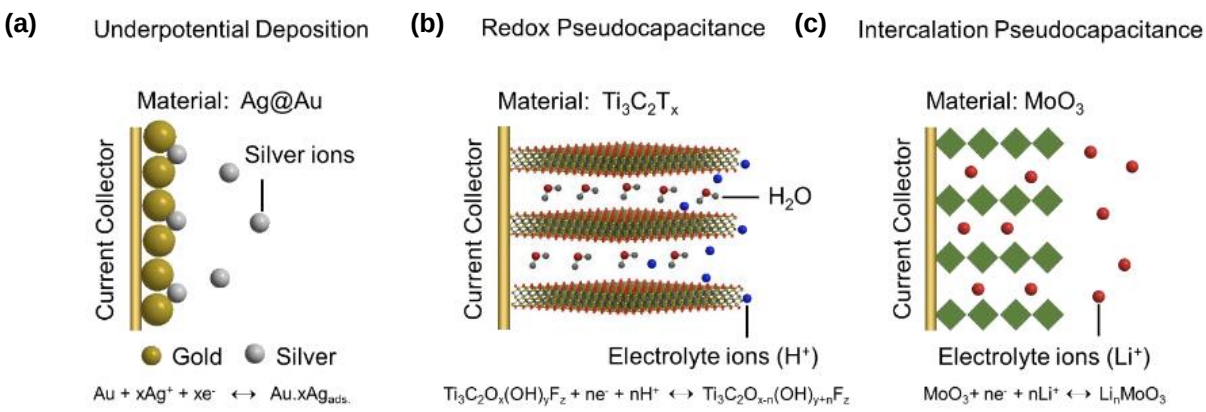

Figure **2.10: [51] Reversible redox reactions that can cause pseudocapacitance: (a) underpotential deposition, (b) redox pseudocapacitance, and (c) intercalative pseudocapacitance.**

2.4.2.1. Underpotential Deposition

The underpotential deposition mechanism refers to the reversible deposition of metal adatoms onto a different metal surface at potentials higher than the Nernst potential of the electrode material. This mechanism is not broadly explored in supercapacitor applications yet. An example is provided on Figure 2.10a where Ag ions are deposited as monolayer on Au metal [1, 24, 26].

2.4.2.2. Redox Pseudocapacitance

Redox pseudocapacitance is the most common mechanism for supercapacitor applications. This mechanism occurs when ion adsorption, accompanied by a faradaic charge transfer arises primarily from a potential energy force. An example of redox pseudocapacitance in Figure 2.10b is the titanium carbide, MXene, undergoing redox reactions with hydronium ions [1, 24, 26].

2.4.2.3. Intercalative Pseudocapacitance

Intercalative pseudocapacitance mechanism is a mechanism that takes place within the bulk of the electrode material when electrolyte ions intercalate/deintercalated without changing the crystallographic phases of the material. Example on Figure 2.10c, Lithium cations intercalating within the MoO_3 crystal structure [1, 24, 26].

2.5. Supercapacitor Optimizable Components for Improved Performance

Over the recent years, concerted research has been directed at materials and electrolyte solutions that show the potential to synergize and effect the high energy density of batteries with the long lifecycle and high-power capabilities of supercapacitors. It was established that the electrochemical performance of supercapacitors hugely depends on intercalation mechanisms, surface of electrode material, electronic conductivity of electrode material and the overall cell design. Therefore, to enhance electrochemical performance, studies have shown that the development of electrode materials merged with suitable electrolyte can provide improved supercapacitive electrochemical performance.

2.6. Two Dimensional (2D) Materials

Nano-structured materials are classified according to dimensions [27]. 2D nanostructured materials have been proven to be more efficient as materials for energy storage than their 0D, 1D, and 3D counterparts because of their unique properties [28]. Beyond graphene various 2D materials have been developed and used for electrochemical energy storage systems due to the surface area and possible combinations that can be configured to tailor hybrid 2D material with

unique structure [29]. Moreover, 2D materials have unique properties such as mechanical stability, transparency, strength, flexibility, and chemical stability [30]. These superior qualities make them useful in electrochemical energy storage. In the huge, branched family of 2Ds. MXene has come forward as a material with great potential for electrochemical energy storage applications [31].

2D materials can be layered together due to weak van de Waals forces on their sheets to improve the electrochemical performance of electrode material. They can also be improved by introducing different functionalities on their surface and between their layers to tailor their properties for enhanced interactions with ions in energy systems [28-30].

2.7. MXenes

MXenes, are a new family of two dimensional (2D) materials incepted in 2011. These materials - also known as transition metal carbides/nitrides or carbonitrides have - Many 2D nanomaterials boast incredible chemical and physical properties. So, like their counterpart 2D nanomaterials such as graphene, transition metal dichalcogenides, graphene oxide, transition metal oxides, transition metal hydrides, hexagonal boron nitride, phosphorenes, germanene and silicenes, MXenes have found application in water purification, biosensing, gas storage, electrocatalysis, electromagnetic shielding to name a few [31,32,36]. The reason for such wide MXene materials application is their chemical and physical properties. MXenes such as Ti_3CT_2 have enthused interest for energy storage applications and showed exciting promise as potential electrode material in batteries, fuel cells, biosensors, and supercapacitors [31-35]. The elevated

attention for energy storage applications, particularly for supercapacitors is based on the unique material composition and structure. Their layered hexagonal structure enables short ion intercalation and shorter ionic transport pathways for charge storage. As a result, MXenes show high cycling rates in batteries and outstanding capacitance in supercapacitors. Also, MXenes have excellent conductivity, and a rich chemistry that can be tuned to accentuate the intrinsic material features based on desired electrode chemistry and electrochemical performance. Figure 2.11 [36] well presents the progressive historic timeline of the inception and development of MXenes.

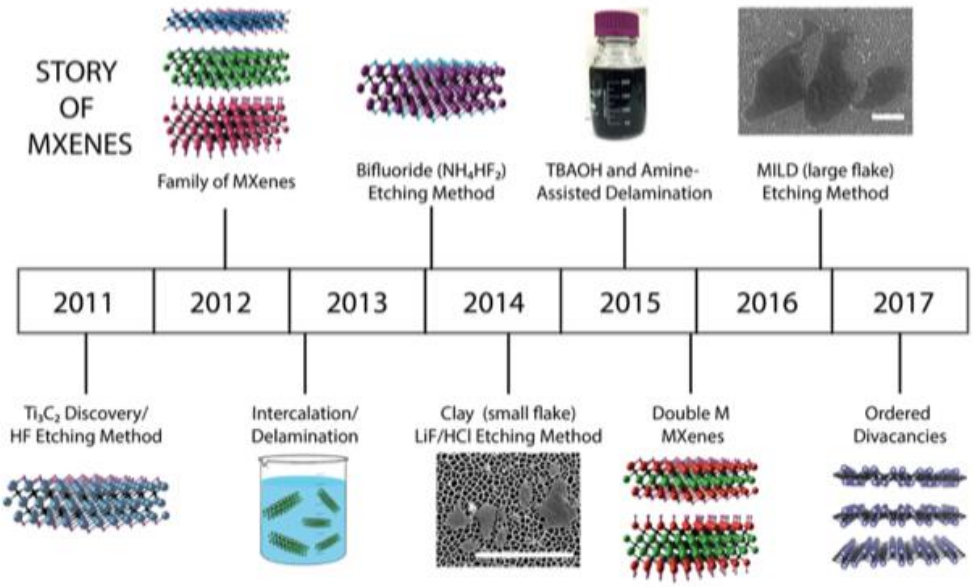

Figure 2.11: Historic timeline of MXenes from inception in 2011, and progress on the material's modification methods from then till 2017 [36]

Fundamentally, at inception, MXenes were produced from their crystal bulk precursors known as 'MAX-phases'. MAX-phases are a group of ternary metal carbides and/or nitrides with a layered hexagonal polycrystallic structure [32]. A simplified description of their structural composition is that of 'mortar and layer' where the bulk material 'MAX' is a composite of the 'M-X' bricks held together by

‘A’ mortar. An assortment of bonds holds the bulk ‘MAX’ together. ‘M-X’ layers are held by strong covalent bonds, while metallic bonds hold M-A atoms relatively weaker forming the MAX crystal from which MXenes can be synthesized. $M_{n+1}AX_n$ is the general composition formula of MAX phases while $M_{n+1}X_nT_x$ is the corresponding general formula for MXenes.

In these general formulas, the following are the representations as presented on the periodic table of elements on Figure 2.12:

M – early transition metals: Ti, V, Ta, Cr, Zr, Mo, Hf, Nb and Sc,

A – A-group elements: Al, Si, S, P, Ga, Al, Ge, Tl, Pb, and Sn,

X – Carbide, Nitride or Carbonitrides,

T_x – Surface termination or surface functional groups: F, Cl, O, and OH,

n: 1-3.

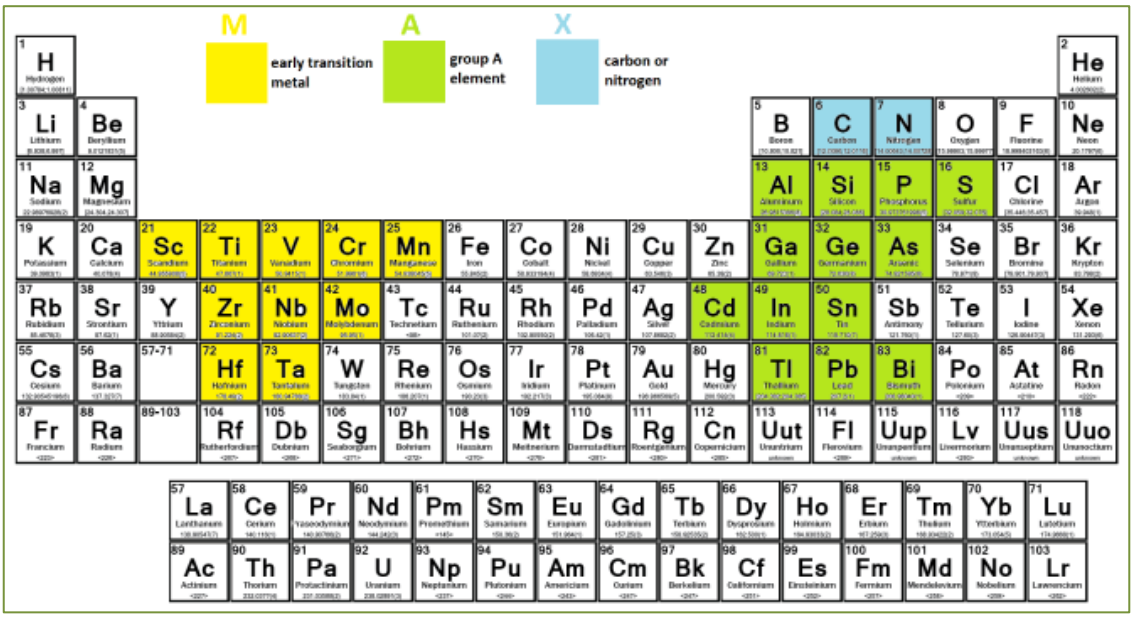

Figure 2.12: MAX elements on the periodic table

The synthesis process of MXenes involves selective chemical etching of the A group atomic layers from the MAX phase precursor by immersing the MAX

powders in etching solutions. This etching process is made possible by the chemically active and weaker, ceramic-like, M-A bond. Figures 2.13 and 2.14 show the MXene stoichiometries that have been “A” group etched by wet-chemical etching protocol involving sonication as a physical technique to separate the MXene sheets subsequent to etching [36].

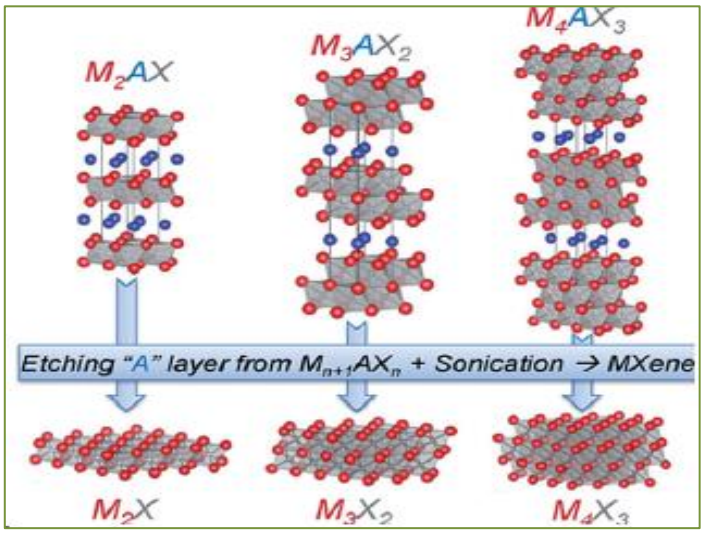

Figure 2.13: MXene etching [52]

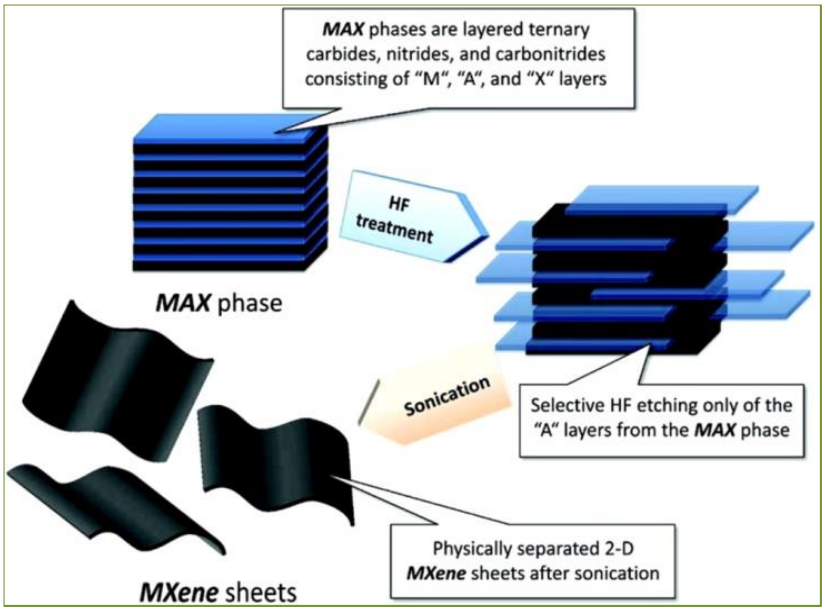

Figure 2.14: Description of the MXene synthesis process [53]

This preferential etching of the M–A bond in $M_{n+1}AX_n$ phases with Al may be summarized according to the following reaction equations:

$$\text{“}M_{n+1}AlX_n + 3HF \rightarrow M_{n+1}X_n + AlF_3 + 1.5H_2\text{”} \quad \textbf{(2.6)}$$

$$\text{“}M_{n+1}X_n + 2H_2O \rightarrow M_{n+1}X_n(OH)_2 + H_2\text{”} \quad \textbf{(2.7)}$$

$$\text{“}M_{n+1}X_n + 2HF \rightarrow M_{n+1}X_nF_2 + H_2\text{”} \quad \textbf{(2.8)}$$

A several wet-chemical etchants have been reported in literature. The type of chemical etchant used induces various effects on the resulting MXene layers. Generally, the most used etchants are HF, or in-situ HF acidic solutions made of fluoride salts such as lithium fluoride (LiF) reacted with a strong acid like hydrochloric acid (HCl) to form in-situ HF. The in-situ method was lately developed and is preferred for its safety and easy preparation than the harsh, high risk, expensive HF.

Wet-chemical etching, whether by highly concentrated HF or mild, in-situ HF method for exfoliating the A group atoms influences the as-synthesized MXenes quality – e.g., surface defects and their concentration. The first advantage of wet-chemical etching is that the resulting $M_{n+1}X_nT_x$ nanosheets are functionalized by randomly distributed hydroxyl, fluoride, oxygens and rarely chloride surface terminations replacing the removed A atomic layer and establishing van der Waals forces that keep the nanosheets loosely held together. This functionalization primarily stems from the presence of water and halide salt cations. The composition and/or surface termination groups can be tuned to design desired surface chemistries and electronic properties for potential application. Secondly, the weak bonds caused by the cations intercalation during etching makes MXenes to be

capable of exfoliation and delamination for modified interlayer spacing. This variable is useful and necessary for electrode architecture and design for energy storage applications where the intercalation and deintercalation process play a crucial role in the electrochemical performance of the energy storage processes. Thirdly, from an important step that follows etching - the delamination step – is useful for weakening the compact multilayer of MXenes. Delamination via intercalation can be facilitated by the introduction of polymers or polar organic molecules followed by mild sonication [32, 36,37].

On synthesis, although the etching of MAX phases is the mostly widely used method, it is also possible to synthesize MXenes from non-MAX phase compounds and high temperature method. Attention is not focused to those methods because of their higher inefficiencies in synthesizing high quality MXene nanosheets.

In summary, MXenes standout as 2D materials because [32-36]:

i. they can be synthesized to have high surface hydrophilicity (providing sites for ionic absorption).
ii. they have high electronic conductivity.
iii. they are chemically and mechanically stable.
iv. a diverse form of monolayer, few layers, and multilayers of MXenes can be formed.
v. their electronic functionality and mechanical stability can be enhanced because possible combinations of heavy and light metals as “M” groups of MXenes allows valence electron tuning.
vi. the thickness of MXene monolayers is controllable.

vii. a variety of chemical groups can be used to modify the surface properties of MXenes; and

viii. like graphene, some of MXenes exhibit massless Dirac dispersions in their band structures near the Fermi level.

The inaugural MXene materials' reports on the interesting chemistries and properties these newly discovered 2D class of materials demonstrate have rapidly drew energy storage materials research to the investigation, exploration and application of these novel materials. For supercapacitors, where both power and energy density increments are sought, mono- and diatomic titanium metal MXenes have showed great promise as presented on table 2.5.

Table 2.4: Titanium carbide MXene based half-cell devices

Electrode Materials	**Electrolyte**	**Cell Configuration**	**Operational Voltage Window (V)**	***SR (mV/s) or **CD (A/g)**	**Capacitance (F/g)**	**Ref.**
$Ti_3C_2T_x$	3M H_2SO_4	3 electrode	0.9	10 mV/s	299	[38]
$Ti_3C_2T_x$	3M KOH	3 electrode	0.9	2.5 A/g	71.2	[39]
$Ti_3C_2T_x$	3M H_2SO_4	3 electrode	0.9	2 mV/s	360	[40]
$Ti_3C_2T_x$	1M KOH	3 electrode	0.8	2 mV/s	135	[40]
$Ti_3C_2T_x$	1M H_2SO_4	3 electrode	0.5	1 mV/s	244	[41]
KOH-$Ti_3C_2T_x$	1M H_2SO_4	3 electrode	0.6	1 mV/s	348	[41]
400-KOH-$Ti_3C_2T_x$	1M H_2SO_4	3 electrode	0.6	1 mV/s	500	[41]

*SR: Scan Rate, ** CD: Current Density

2.8. Chemical modification of 2D materials using redox-active molecules for energy storage (Metallotetrapyrazinoporphyrazine)

From a materials science perspective, MXene can serve as an important unit in nano-structuring, nanomaterials design, composites and hybrids materials synthesis [30-32]. Of direct relevance to this work, is the intercalation of metallo-organocyclic [42] complex into and on the lightest MXene reported in literature, Ti_2CT_x [43], via delamination. The electrochemical performance of nickel(II) tetrapyrazinoporphyrazine integrated MXene (Ti_2CT_x) has never been studied. The choice of these materials for this study was motivated by the reports that material like graphene and transition metal oxides can exhibit improved electrochemical performance when integrated with nitrogen-rich pyrrolic materials [44-46].

2.9. Metallotetrapyrazinoporphyrazines

Metallotetrapyrazinoporphyrazines, are a unique class metallo-heterocyclic complexes analogous of metallophtalocyanines [47]. In their structural composition, they have four pyrazino-fused pyrrolic rings held together by aza nitrogen atoms. These macro-heterocyclic molecules are highly aromatic. The aza nitrogens or meso-nitrogen atoms (as presented on Figure 2.15) that act as bridges that keep the four pyrroles together. Macrocyclic tetrapyrrole ring systems such as porphyrins, tetraazaporphyrins, porphyrazine and phtalocyanines compounds have found application: in the dye and pigmentation industry; in biology - cell respiration, photosynthesis, and electron transport; in medicine as active agents in photodynamic therapy (PDT); in optical data storage technologies; in applied electrochemistry, they have been used as electrocatalysts in gas sensing amongst other applications. They are low-cost and have a rich chemistry that is stable

against oxidation and highly electromagnetic active in the ultraviolet-visible range, absorbing long wavelengths intensely. A metallotetrapyrazinoporphyrazine is highly electronegative due to eight nitrogen in its outer macrocyclic system. This makes it to be a good δ donor and π acceptor. [48-49]

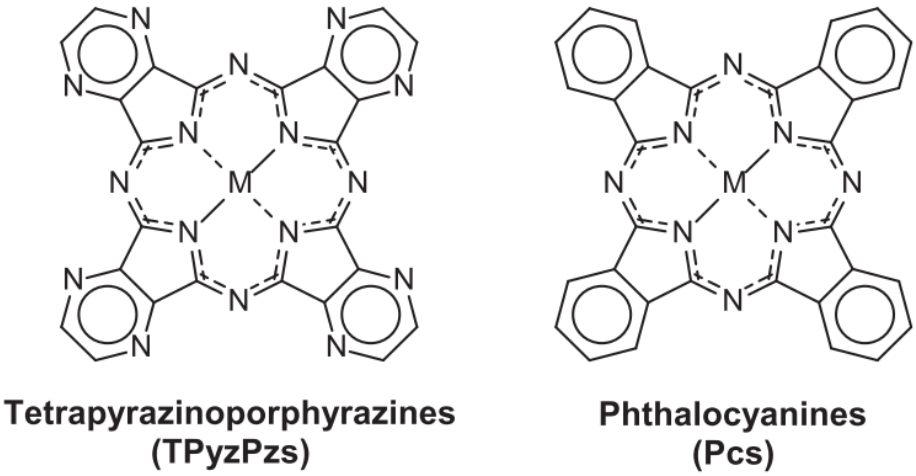

Figure 2.15: Chemical structures of tetrapyrazinoporphyrazine and phthalocyanines with a metal [48]

2.10. Integration of Metallotetrazinoporphyrazine Material onto MXene (Titanium Carbide, Ti_2C)

According to literature, redox active organic materials and metal ions can be intercalated into layered MXene and lead to modified properties of MXene for better electrochemical performance. To achieve advanced electrochemical performances, it is recorded that conducting organic active compounds like polypyrrolic polymers and polyanalines can play an important role in the pseudocapacitive intercalation process in energy storage devices [47,50]. These MXene composites exhibit improved gravimetric capacitance as well as excellent capacitance retention at both low and high scan rates due to the improved accessibility of protons to the surface of MXene layers.

2.11. Reference List

[1] Conway, B.E., (1999). '*Electrochemical Supercapacitors: Scientific Fundamentals and Technological Applications'*. New York: Kluwer Academic/Plenum.

[2] González, A., Goikolea, E., Barrena, and J.A. Mysyk, R. (2016). 'Review on supercapacitors: Technologies and materials', *Renewable and Sustainable Energy Reviews*, 58, pp. 1189–1206. doi: 10.1016/j.rser.2015.12.249.

[3] Wang, Y., Song, Y. and Xia, Y. (2016). 'Electrochemical capacitors: mechanism, materials, systems, characterization and applications', *Chem. Soc. Rev. Royal Society of Chemistry*, 45(21), pp. 5925–5950. doi: 10.1039/C5CS00580A

[4] Simon, P., Brousse, T. and Favier, F. (2017)., *Supercapacitors Based on Carbon or Pseudocapacitive Materials, Volume 3*. United Kingdom: ITSE Ltd / Wiley & Sons, Inc. doi: 10.1002/9781119007333.

[5] Pandolfo, T., Ruiz, V., Sivakkumar, T., and Nerkar, J., *'*General Properties of Electrochemical Capacitors', In: Supercapacitors Materials, Systems, and Applications (Edited by: Lu, M., Béguin, F. and Frackowiak, E.), Wiley-VCH Verlag GmbH & Co. KGaA pp. 69-109.

[6] Shao, ., El-Kady, M.F., Sun, J., Li, Y., Zhang, Q., Zhu, M., Wang, H., Dunn, B., and Kaner, R.B. (2018) 'Design and Mechanisms of Asymmetric Supercapacitors', *Chemical Reviews. American Chemical Society*, 118(18), pp. 9233–9280. doi: 10.1021/acs.chemrev.8b00252.

[7] Kim, B.K., Sy, S., Yu, A., and Zhang, J. (2015) 'Electrochemical Supercapacitors for Energy Storage and Conversion', *Handbook of Clean Energy Systems*, pp. 1–25. doi: 10.1002/9781118991978.hces112.

[8] Végvári, Z. (2020) 'Supercapacitors and their military applicability'*, Honvédségi Szeml*e, 147(1–2), pp. 38–49. doi: 10.35926/hdr.2019.1-2.3.

[9] Yu, A., Chabot, V. and Zhang, J. (2017) *'Electrochemical supercapacitors for energy storage and delivery: Fundamentals and applications, Electrochemical Supercapacitors for Energy Storage and Delivery: Fundamentals and Applications'*. Roca Raton, Flourida: CRC Press. pp. 1-355doi: 10.1201/b14671.

[10] Li, L., Huang, Z., Li, H., and Lu, H. (2016). 'A high-efficiency voltage equalization scheme for supercapacitor energy storage system in renewable generation applications', *Sustainability*, 8(6). doi: 10.3390/su8060548.

[11] Christen, T., and Carlen, M. W. (2000). 'Theory of ragone plots', *Journal of Power Sources*, 91(2), pp. 210–216. doi: 10.1016/S0378-7753(00)00474-2.

[12] Simon, P. and Gogotsi, Y. (2008) 'Materials for electrochemical capacitors', *Nature Materials*, 7(11), pp. 845–854. doi: 10.1038/nmat2297.

[13] Simon, P., Gogotsi, Y., and Dunn, B. (2014) 'Where Do Batteries End and Supercapacitors Begin?', *Science*, 343(6176), pp. 1210–1211. doi: 10.1126/science.1249625.

[14] Schneuwly, A. and Gallay, R. (2000). 'Properties and applications of supercapacitors from the state-of-the-art to future trends', *Thirty-seventh International Intelligent Motion Conference: PCIM 2000 Europe,* Nürnberg, Germany, June 6-8, 2000

[15] Balducci, A. (2016) 'Electrolytes for high voltage electrochemical double layer capacitors: A perspective article', *Journal of Power Sources*. Elsevier B.V, 326, pp. 534–540. doi: 10.1016/j.jpowsour.2016.05.029.

[16] Gao, Y., Wang, L., Li, Z., Zhang, Y., Xing, B., Zhang, C., and Zhou, A. (2015). 'Electrochemical performance of Ti_3C_2 supercapacitors in KOH electrolyte', *Journal of Advanced Ceramics*, 4(2), pp. 130–134. doi: 10.1007/s40145-015-0143-3.

[17] Pal, B., Yang, S., Ramesh, S., Thangadurai, V. and Jose, R. (2019) 'Electrolyte selection for supercapacitive devices: A critical review', *Nanoscale Advances. Royal Society of Chemistry*, 1(10), pp. 3807–3835. doi: 10.1039/c9na00374f.

[18] Chen, T. and Dai, L. (2013) 'Carbon nanomaterials for high-performance supercapacitors', *Materials Today. Elsevier Ltd*., 16(7–8), pp. 272–280. doi: 10.1016/j.mattod.2013.07.002.

[19] Guan, L., Yu, L. and Chen, G. Z. (2016) 'Capacitive and non-capacitive faradaic charge storage', *Electrochimica Acta. Elsevier Ltd*, 206, pp. 464–478. doi: 10.1016/j.electacta.2016.01.213.

[20] Wang, H. and Pilon, L. (2011) 'Accurate simulations of electric double layer capacitance of ultramicroelectrodes', *Journal of Physical Chemistry C*, 115(33), pp. 16711–16719. doi: 10.1021/jp204498e.

[21] Bard, A.J., and Faulkner, L.R., (2004). *'Electrochemical methods: fundamentals and applications',* Second edition. New York: John Wiley & Sons, Inc.

[22] Brett, C. (2008). *'Fundamentals of electrochemistry'*, Second edition. Hoboken, New Jersey: John Wiley & Sons, Inc. doi: 10.1007/978-3-540-77508-9_8.

[23] Kant, R. and Singh, M. B. (2013) 'Generalization of the Gouy-Chapman-Stern model of an electric double layer for a morphologically complex electrode:

Deterministic and stochastic morphologies', *Physical Review E - Statistical, Nonlinear, and Soft Matter Physics,* 88(5), pp. 1–16. doi: 10.1103/PhysRevE.88.052303.

[24] Wang, J., Dong, S., Ding, B., Wang, Y., Hao, X., Dou, H. Xia, Y., and Zhang, X. (2017) 'Pseudocapacitive materials for electrochemical capacitors: From rational synthesis to capacitance optimization', *National Science Review*, 4(1), pp. 71–90. doi: 10.1093/nsr/nww072.

[25] Boota, M. (2017). *Redox-active Hybrid Materials for Pseudocapacitive Energy Storage*, Ph.D Thesis. Drexel University. Available at: https://idea.library.drexel.edu/islandora/object/idea%3A7597 [accessed at: 30 June 2019].

[26] Augustyn, V., Simon, P. and Dunn, B. (2014) 'Pseudocapacitive oxide materials for high-rate electrochemical energy storage', *Energy and Environmental Science,* 7(5), pp. 1597–1614. doi: 10.1039/c3ee44164d.

[27] Pokropivny, V., Hussainova, I. and Vlassov, S. (2007). 'Introduction to nanomaterials and nanotechnology', *Introduction in Nanomaterials and Nanotechnology*, pp. 1–138. Available at: https://www.tyk.ee [accessed at: 23 November 2018]

[28] Yu, Z., Tetard, L., Zhai, L., and Thomas, J. (2015) 'Supercapacitor electrode materials: Nanostructures from 0 to 3 dimensions', Energy and Environmental Science. *Royal Society of Chemistry,* 8(3), pp. 702–730. doi: 10.1039/c4ee03229b.

[29] Butler, S.Z., Hollen, S.M., Cao, L., Cui, Yi., Gupta, J.A., Gutiérrez, H.R., Heinz, T.F., Hong, S.S., Huang, J., Ismach, A.F., Johnston-Halperin, E., Kuno, M., Plashnitsa, V.V., Robinson, R.D., Ruoff, R.S., Salahuddin, S.S., Sham, J., Shi,

L.Spencer, M.G., Terrones, M., Windl, W., and Goldberger, J.E. (2013) 'Progress, challenges, and opportunities in two-dimensional materials beyond graphene', *ACS Nano*, 7(4), pp. 2898–2926. doi: 10.1021/nn400280c.

[30] Mendoza-Sánchez, B. and Gogotsi, Y. (2016) 'Synthesis of Two-Dimensional Materials for Capacitive Energy Storage', *Advanced Materials*, 28(29), pp. 6104–6135. doi: 10.1002/adma.201506133.

[31] Hong Ng, V.M.,Huang, H., Zhou, K., Lee, P.L., Que, W., Xu J.Z., and Kong, L.B. (2017) 'Recent progress in layered transition metal carbides and/or nitrides (MXenes) and their composites: synthesis and applications', *Journal of Materials Chemistry A*, 5(7), pp. 3039–3068. doi: 10.1039/c6ta06772g.

[32] Anasori, B., Lukatskaya, M. R. and Gogotsi, Y. (2018) '2D metal carbides and nitrides (MXenes) for energy storage', *Nature Review Materials*, 2(2), pp 1-17. doi: 10.1038/natrevmats.2016.98.

[33] Er, D., Li, J., Naguib, M., Gogotsi, Y., and Shenoy, V.B. (2014) 'Ti_3C_2 MXene as a highcapacity electrode material for metal (Li, Na, K, Ca) ion batteries', *ACS Applied Materials and Interfaces*, 6(14), pp. 11173–11179. doi: 10.1021/am501144q.

[34] Lorencova, L., Bertok, T., Dosekova, E., Holazova, A., Paprckova, D., Vikartovska, A., Sasinkova, A., Filip, J., Kasak, P., Jerigova, M., Velic, D., Mahmoud, K.A., and Tkac,J. (2017) 'Electrochemical performance of $Ti_3C_2T_x$ MXene in aqueous media: towards ultrasensitive H_2O_2 sensing', *Electrochimica Acta. Elsevier Ltd*, 235, pp. 471–479. doi: 10.1016/j.electacta.2017.03.073.

[35] Wang, Y., Li, Y., Qiu, Z., Wu, X., Zhou, P., Zhou, T., Zhao, J., Miao, Z., Zhou, J., and Zhuo, S. (2018) 'Fe_3O_4@Ti_3C_2 MXene hybrids with ultrahigh volumetric capacity as an anode material for lithium-ion batteries', *Journal of Materials*

Chemistry A. Royal Society of Chemistry, 6(24), pp. 11189–11197. doi: 10.1039/c8ta00122g.

[36] Alhabeb, M., Maleski,K., Anasori, B., Lelyukh, P., Clark, L., Sin, S., and Gogotsi, Y. (2017) 'Guidelines for Synthesis and Processing of Two-Dimensional Titanium Carbide ($Ti_3C_2T_x$ MXene)', *Chemistry of Materials*, 29(18), pp. 7633–7644. doi: 10.1021/acs.chemmater.7b02847.

[37] Rasid, Z.A.M., Omar, M.F., Nazeri, M.F.M., A'ziz, M.A.A., and Szota, M. (2017). 'Low Cost Synthesis Method of Two-Dimensional Titanium Carbide MXene', *IOP Conference Series: Materials Science and Engineering*, 209(1). doi: 10.1088/1757-899X/209/1/012001.

[38] Chen, C., Boota,M., Urbankowski, P., Anasori, B., Miao, L., Jiang, J., Gogotsi, Y. (2018) 'Effect of glycine functionalization of 2D titanium carbide (MXene) on charge storage', *Journal of Materials Chemistry A*, 6(11), pp. 4617–4622. doi: 10.1039/c7ta11347a.

[39] Gao, Y., Wang, L., Li, Z., Zhang, Y., Xing, B., Zhang, C., and Zhou, A. (2015). 'Electrochemical performance of Ti_3C_2 supercapacitors in KOH electrolyte', *Journal of Advanced Ceramics*, 4(2), pp. 130–134. doi: 10.1007/s40145-015-0143-3.

[40] Shao, H. Lin, Z., Xu, K., Taberna, P-L., and Simon, P. (2019). 'Electrochemical study of pseudocapacitive behavior of $Ti_3C_2T_x$ MXene material in aqueous electrolytes', *Energy Storage Materials. Elsevier* 18(December 2018), pp. 456–461. doi: 10.1016/j.ensm.2018.12.017.

[41] Li, J., Yuan, X., Lin, C., Yang, Y., Xu, L., Du,X., Xie, J., Lin, J., and Sun, (2017) 'Achieving High Pseudocapacitance of 2D Titanium Carbide (MXene) by Cation

Intercalation and Surface Modification', *Advanced Energy Materials*, 7(15). doi: 10.1002/aenm.201602725.

[42] Tuncer, S., Koxa, A., Gü, A., and Avciata, U. (2012). 'Synthesis, characterization, electrochemistry and spectroelectrochemistry of novel soluble porphyrazines bearing unsaturated functional groups', *Dyes and Pigments*, 92(1), pp. 610–618. doi: 10.1016/j.dyepig.2011.05.023.

[43] Naguib, M., Come, J., Dyatkin, J., Presser, V. Taberna, P-L., Simon, P., Barsoum, M.Q., and Gogotsi, Y. (2012) 'MXene: A promising transition metal carbide anode for lithium-ion batteries', *Electrochemistry Communications*, 16(1), pp. 61–64. doi: 10.1016/j.elecom.2012.01.002.

[44] Lekitima, J.N., Ozoemena, K.I., and Kobayashi, N. (2013) 'Electrochemical Capacitors Based on Nitrogen-Enriched Cobalt (II) Phthalocyanine/Multi-walled Carbon Nanotube Nanocomposites', *ECS Transactions*, 50 (43) 125-132. doi: 10.1149/05043.0125ecst

[45] Makgopa, K., Ejikeme, P. M. and Ozoemena, K. I. (2016) 'Graphene oxide-modified nickel(II) tetra-aminophthalocyanine nanocomposites for high-power symmetric pseudocapacitor', *Electrochimica Acta. Elsevier Ltd*, 212, pp. 876–882. doi: 10.1016/j.electacta.2016.07.027.

[46] Boota, M., Pasini, M., Galeotti, F., Porzio,W., Zhao, M-Q., Halim, J., and Gogotsi, Y. (2017) 'Interaction of Polar and Nonpolar Polyfluorenes with Layers of Two-Dimensional Titanium Carbide (MXene): Intercalation and Pseudocapacitance', *Chemistry of Materials*, 29(7), pp. 2731–2738. doi: 10.1021/acs.chemmater.6b03933.

[47] Novakova, V., Donzello M.P., Ercolani, C., Zimcik, P., and Stuzhin, P.A. (2018) 'Tetrapyrazinoporphyrazines and their metal derivatives. Part II: Electronic

structure, electrochemical, spectral, photophysical and other application related properties', *Coordination Chemistry Reviews. Elsevier*, 361, pp. 1–73. doi: 10.1016/j.ccr.2018.01.015.

[48] Donzello, M.P., Ercolani, C., Novakova, V., Zimcik, P., and Stuzhin, P.A. (2016) 'Tetrapyrazinoporphyrazines and their metal derivatives. Part I: Synthesis and basic structural information', *Coordination Chemistry Reviews. Elsevier*, 309, pp. 107–179. doi: 10.1016/j.ccr.2015.09.006.

[49] Rodríguez-Morgade, M. S. and Stuzhin, P. (2004) 'The chemistry of porphyrazines: an overview', *Journal of Porphyrins and Phthalocyanines*, 08(09), pp. 1129–1165. doi: 10.1142/S1088424604000490.

[50] Boota, M., Anasori, B., Voigt, C., Zhao, M-Q, Barsoum, M.W., and Gogotsi, Y. (2016) 'Pseudocapacitive Electrodes Produced by Oxidant-Free Polymerization of Pyrrole between the Layers of 2D Titanium Carbide (MXene)', *Advanced Materials,* 28(7), pp. 1517–1522. doi: 10.1002/adma.201504705.

[51] Boota, M. (2017). *Redox-active Hybrid Materials for Pseudocapacitive Energy Storage*, Ph.D Thesis. Drexel University. Available at: https://idea.library.drexel.edu/islandora/object/idea%3A7597 [accessed at: 30 June 2019].

[52] Naguib, M., Mochalin, V.N., Barsoum, M.W., and Gogotsi, Y. (2014) '25th anniversary article: MXenes: A new family of two-dimensional materials', *Advanced Materials*, 26(7), pp. 992–1005. doi: 10.1002/adma.201304138.

[53] Naguib, M., Mashtalir, O., Carle, J., Presser, V., Lu, J., Hultman, L., Gogotsi, Y., and Barsoum, M.W. (2012). 'Two-dimensional transition metal carbides', *ACS Nano,* 6(2), pp. 1322–1331. doi: 10.1021/nn204153h.

CHAPTER 3
RESEARCH METHODOLOGY
MATERIALS, EXPERIMENTAL PROCEDURES AND TECHNIQUES

In this chapter, the chemicals used, procedures followed for the synthesis of materials, techniques employed for material characterization and electrochemical performance evaluation will be listed and briefly explained.

3.1. Reagents and Materials

All reagents and chemicals used were purchased from different suppliers. The de-ionized and ultrapure water used in this research was treated using the Direct-Q® 3 UV Water Purification System at room temperature. Figure 3.1 shows the purification system for ultrapure water treatment. This water purification system consists of three water treatment technology components: (i) pre-treatment media, (ii) reverse osmosis membrane – organic matter destruction and chlorine oxidation occurs at this point, and (iii) ion exchange membrane – the treated water is deionized at this stage prior to irradiation with a 185 and a 254 nm ultraviolet beam to remove or minimize all organics by destroying the bonds in organics and the subsequent final filtration system to ensure particulate filtration of the water [1]. Organics and suspended particles are undesired for aqueous electrolyte application because they can compromise the electrolyte purity and negatively affect the electrolyte potential stability window (EPSW) and introduce a source of error to the electroactive and resistance of materials and electrolyte under study [2].

Figure 3.1: Direct-Q® 3 UV water purification system

Chemicals: salts and solvents used for the synthesis of electrode materials, electrolyte, electrode preparation and coating are respectively listed in the succeeding sections.

3.1.1. Synthesis of Materials

Table 3.1: List of chemicals used for material synthesis

Compound	**Formula**	**Purity**	**Manufacturer**
Lithium fluoride	LiF	99.99%	Merck, Germany
Hydrochloric acid	HCl	32%	Sigma, Germany
MAX phase (Maxthal ® 211)	Ti_2AlC	> 90%	Kanthal, Sweden
2,3-Pyrazinedicarbonitrile	$C_6H_2N_4$	98%	Sigma, Germany
Nickel(II) chloride hexahydrate	$NiCl_2.6H_2O$	99.9%	Sigma, Germany
Ethylene glycol, anhydrous	$C_2H_6O_2$	99.8%	Sigma, Germany
Methanol	CH_4O	> 99.8%	Merck, Germany
Ethanol	C_2H_6O	96%	Sigma, Germany

3.1.2. Electrolyte Preparation and pH Measurements

Table 3.2: List of chemicals used for electrolyte preparation

Compound	Formula	Purity	Manufacturer
Lithium sulphate monohydrate	$Li_2SO_4.H_2O$	>99.0%	Sigma, Germany
Lithium hydroxide	LiOH	>98.0%	Sigma, Germany
Sulphuric acid	H_2SO_4	97.0%	Sigma, Germany
Deionized and Ultrapure water	H_2O	Ultrapure	JW, South Africa

3.1.3. Cell Fabrication Materials

Table 3.3: List of chemicals and materials used for cell fabrication

Compound	Formula	Purity/Grade	Manufacturer
Carbon black additive, Timcal C45	C	99.99%	MTI Corp., USA
Polyvinyldiene fluoride (PVDF)	$-(C_2H_2F_2)_n-$	>99.5%	MTI Corp., USA
N-Methyl-2-pyrrolidone (NMP)	C_5H_9NO	>99.5%	MTI Corp., USA
Carbon paper, multilayer porous sheet	N/A	P75	AvCarb, USA
Glass fiber filter paper, Whatmann ®	N/A	GF/F	Sigma, Germany
MTI ® two and three electrode split cells	Material: stainless steel		MTI Corp., USA

3.2. Synthesis Procedures

A three-step synthesis protocol was employed, as schematically illustrated on Figure 3.2, where the MAX phase, Ti_2AlC, was exfoliated by wet-chemical etching to obtain MXene, Ti_2CT_x. The obtained MXene was then subsequently intercalated via delamination with a metallotetrapyrazinoporphyrazine complex.

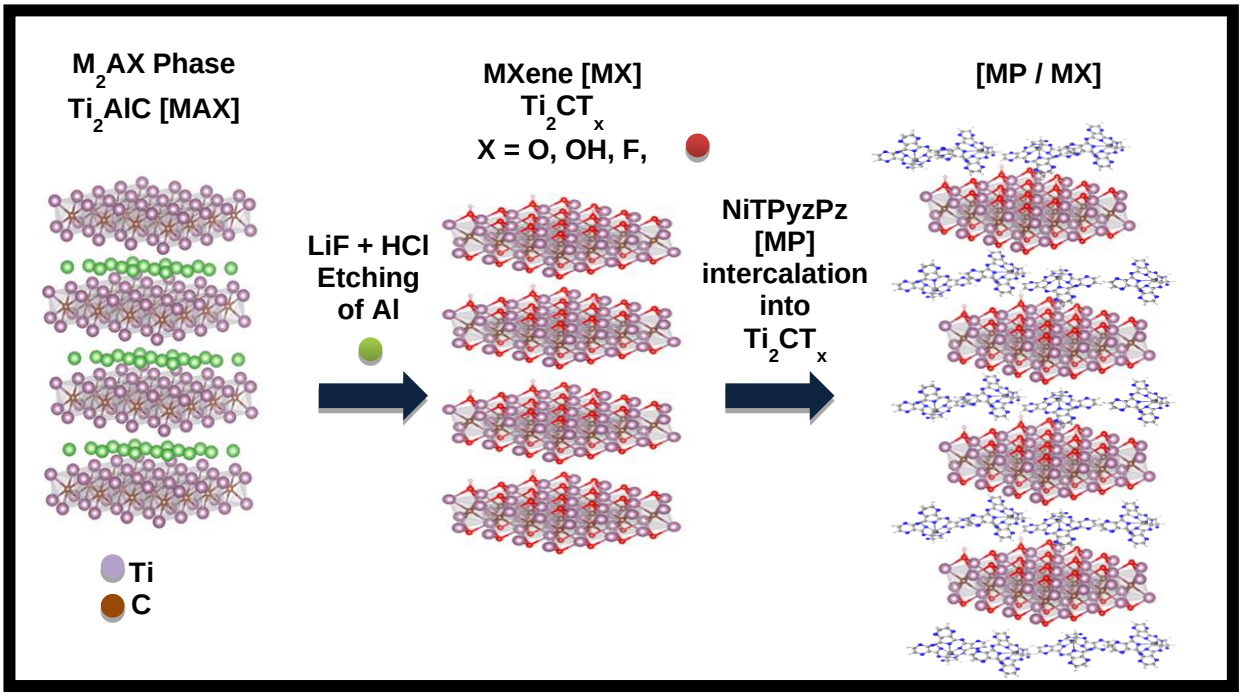

Figure 3.2: Schematic diagram of in-situ HF exfoliation of Ti_2AlC followed by NiTPyzPz intercalation

3.2.1. Synthesis of MXene (Ti_2CT_x)

MXene, Ti_2CT_x, was synthesized by wet chemical exfoliation of the commercial Ti_2AlC, Maxthal® 211, powder following the in-situ HF procedure [3]. An in-situ HF etching method was used because of safer conditions and less aggressive nature as compared to concentrated HF [4]. The mild LiF+HCl (in situ HF) solution was prepared by dissolving two grams of LiF salt into 40 mL of 6 M, HCl solution. To ensure complete dissolution of salt in solvent, the solution was sonicated for 15

minutes. After sonication, two grams of Ti_2AlC powders were gradually added to the in-situ HF solution. The gradual addition of the MAX bulk was necessitated by an exothermic nature of the exfoliation reaction. As soon as two grams of Ti_2AlC was completely immersed into the in-situ HF solution, the mixture was stirred for 2 minutes and heated to 40 degrees Celsius for 48 hours while stirring. Subsequently, after 48 hours, the mixture was centrifuged and washed with deionized water and rinsed with ethanol a couple of times until the supernatant reached a pH of approximately 6. Finally, after washing and rinsing, the obtained powder Al etched Ti_2AlC powders were dried in a vacuum oven for 48 hours at 45 degrees Celsius.

3.2.2. Synthesis of Nickel(II) tetrapyrazinoporphyrazine (NiTpyzPz)

Exactly 4 millimoles of 2,3-dicarbonitrile mixed with 1 millimole of Dinickel chloride hexahydrate were added to 30 mL of ethylene glycol. The resulting solution was stirred for 5 minutes at room temperature. After the dissolution of solids in ethylene glycol by magnetic stirring, the solution was transferred into a microwave vessel and then ultimately put into the microwave and irradiated for 6 minutes at a ramp temperature of 190 degrees Celsius. Thereafter, the microwave irradiated solution was left in air at room temperature to cool before centrifugation for washing. Deionized water and methanol were used to wash the yielded solids. After the washing process, the nickel(II) tetrapyrazinoporphyrazine was dried in an oven for 48 hours. For purification, the obtained solid was cleaned with 6 M of Sulphuric acid for 72 hours followed by further rinsing with 10% warm ethanol for three days using the Soxhlet extraction system. Figure 3.3 show the synthesis route for the formation of NiTpyzPz

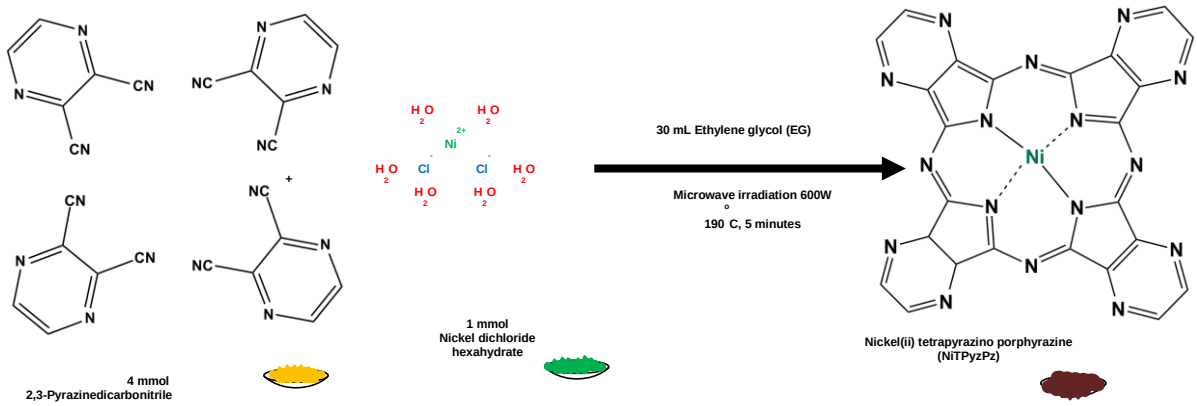

Figure 3.3: Schematic diagram of the microwave assisted synthesis of NiTpyzPz

3.2.3. Synthesis of NiTpyzPz/Ti_2CT_x (MP/MX) Composite

To tune the properties of Ti_2CT_x, 5 and 15 wt% nickel(II) tetrapyrazinoporphyrazine (NiTpyzPz) were intercalated into the layered matrix of the MXene. Ti_2CT_x, 5% NiTpyzPz, and 15% NiTpyzPz are denoted as MX, MP-5/MX, and MP-15/MX respectively. These composites were synthesized by dispersing the as-synthesized MXene powder in DMF by sonication, dissolving the NiTpyzPz solid in DMF and mixing the two mixtures as outlined on Figure 3.4 so as to delaminate and intercalate the MX layered with MP-5 and MP-15.

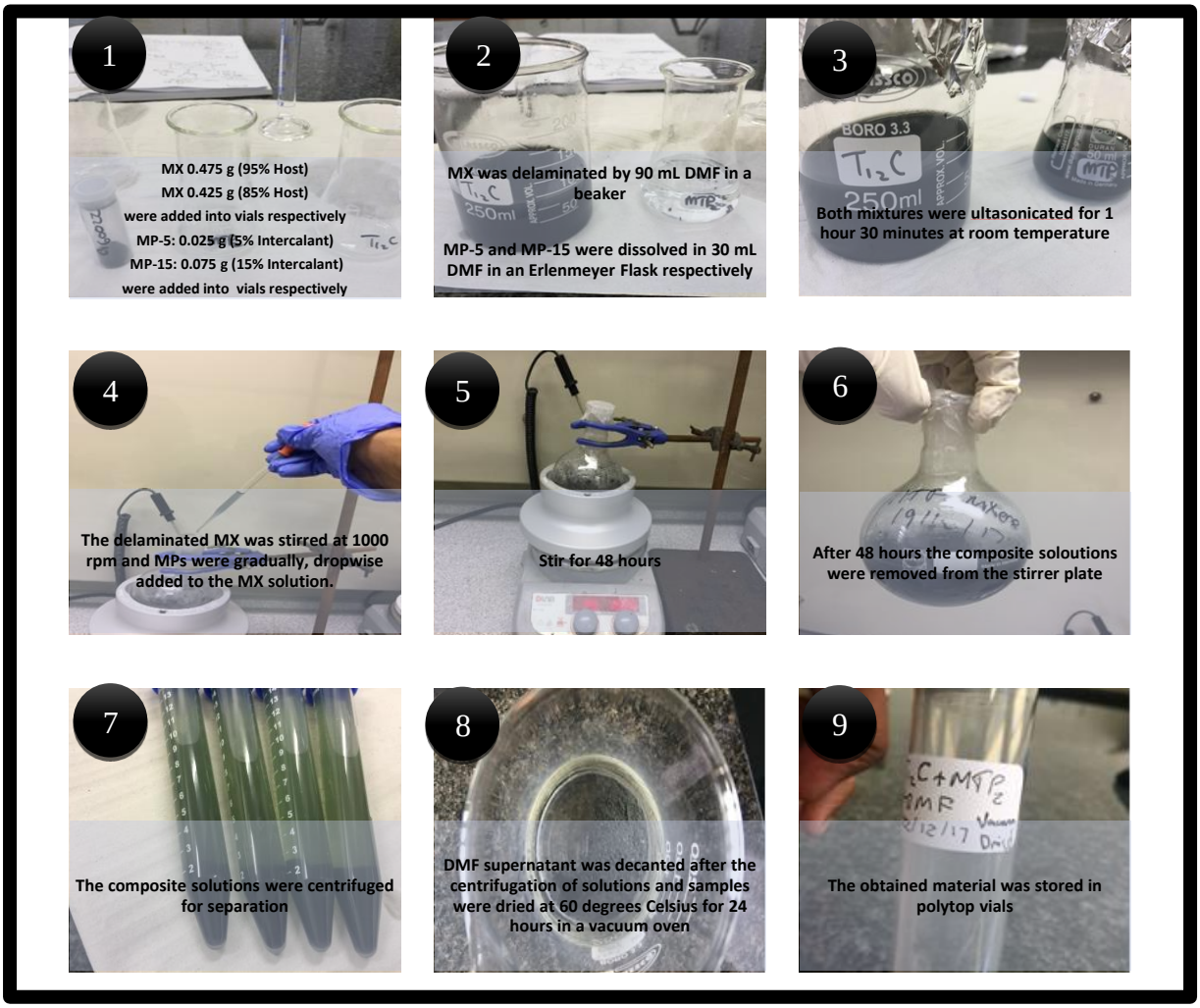

Figure **3.4: Flow diagram of MP/MX composite synthesis - Wits School of Chemistry, Lab C112**

3.3. Material Characterization Techniques

3.3.1. Spectroscopic Characterization

3.3.1.1. Powder X-ray Diffraction Spectroscopy

Powder X-ray Diffraction (PXRD) spectroscopy is a powerful, non-destructive spectroscopic technique that can be employed to understand the crystallinity, interlayer spacing, and phase changes of the material [5]. This technique has its origin in a 1912 observation of the interaction of crystalline materials with X-ray radiation. In this observation, crystalline substances were identified to have an interference with a passed radiation beam. The crystal matter acted as three-dimensional x-ray wave dispersing elements for X-ray with dispersions that are similar to the planes in a crystal lattice. The relationship between the electromagnetic wave and the diffraction angle and the crystal lattice spacing is related according to the Bragg's law below expressed as equation 3.1:

$$n\lambda = 2d\ sin\ \theta \qquad \textbf{(3.1)}$$

where n is an integer (the order of the diffracted beam), λ is the wavelength of the incident X-ray beam, d is the interplanar spacing between the atomic scale crystal planes, and θ is an angle of incidence [5-6]

In this work, X-Ray diffraction patterns were recorded with a Bruker, D2 Phaser X-ray diffractometer (Figure 3.5) equipped with a Cobalt tube x-ray source, Co Kα (λ = 1.79 Å), at a 0.026^o step size and dwell time 0.01 sec/step over a 7^o ≤ 2θ ≤ 100^o range operated at 40kV and 10ma.The diffractometer was operated with a Bruker.Diffrac software and Diffrac.EVA was used to identify the crystal phases.

(a) (b)

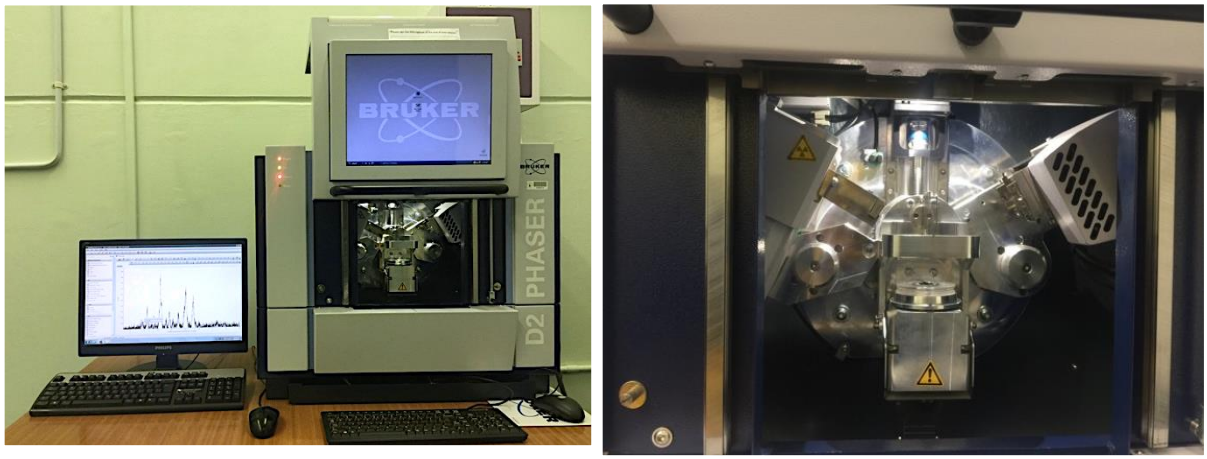

Figure 3.5: (a) Bruker D2 Phaser and PC controller; (b) sample chamber - *Wits Microscopy and Microanalysis Unit*

3.3.1.2. Fourier-Transform Infrared Spectroscopy

Fourier-transform infrared (FTIR) spectroscopy is a simple, fast, non-destructive spectroscopic technique. It is widely used in nanomaterials for obtaining the characteristic molecular fingerprint of materials. An electromagnetic radiation in the mid-infrared region (4000 - 400cm^{-1} wavelengths) is radiated to the sample of study and characteristic measurements are obtained according to the mid-IR interaction with the atomic and molecular vibrational bonds. Samples that absorb mid-IR have induced dipole moments with unique band positions that can be measured and translated to an electric signal with specific intensities on the spectrum at respective wavenumbers to give an insight on the molecular interactions present in the sample and the respective functional structures [8-9]. The Bruker Tensor 27 Fourier-Transform IR spectrometer (Figure 3.6) was used to characterize the functional groups of the synthesized MXene before and after nickel(II) tetrapyrazinoporphyrazine intercalation.

(a) (b)

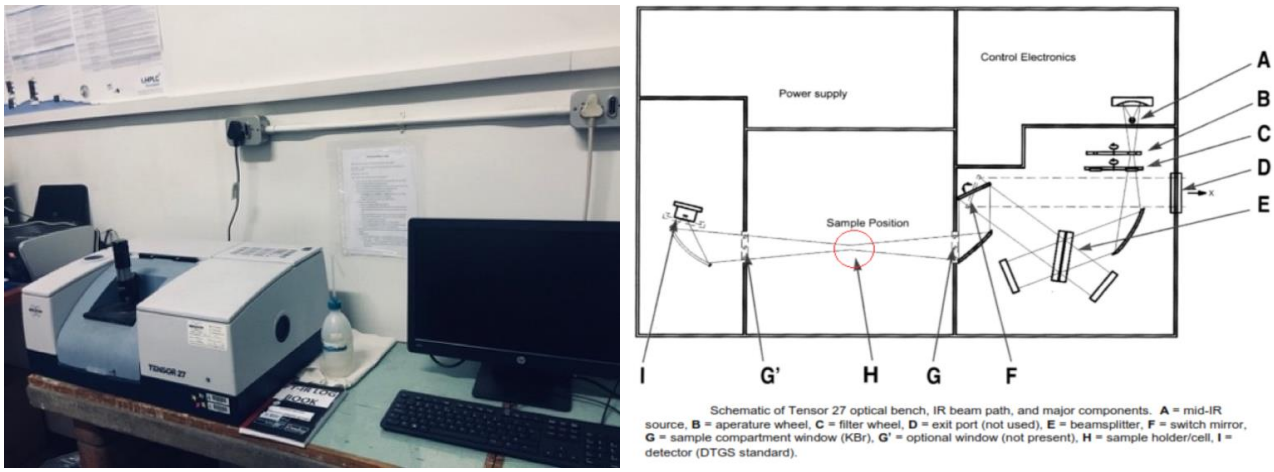

Figure 3.6: (a) Bruker Tensor 27 FTIR spectrometer and (b) schematic description of the major components of Bruker Tensor 27 FTIR spectrometer [9]

3.3.1.3. Raman Spectroscopy

Raman spectroscopic is a spectroscopic analytical technique based on the scattering phenomena of electromagnetic waves in the 4000-10 cm^{-1} range upon interacting with molecular vibration of matter. The Raman spectrum is an output of the scattered and vibrational modes at specific wavenumbers [10]. In this work, this technique was employed to probe chemical bonding information within the molecules of the material using the Horiba LabRAM HR micro-Raman. The laser used was Ar ion excited with 514.5 nm and 0.5 mW power at the sample. The microscope used was the Olympus BX41 fitted with a 100x lens. The LabSpec v5 was the software used to process the spectra. Figure3.7 shows the LabRamHR micro-Raman equipment.

Figure 3.7: Horiba LabRAM HR Raman spectrometer [11] – Same model as Wits Physics instrument

3.3.1.4. Ultraviolet/Visible Spectroscopy

Ultraviolet-visible (UV/vis) spectroscopy is an analytical spectroscopic technique based on the interaction of UV/vis light with matter. When some materials interact with the UV/vis electromagnetic radiation they absorb it. So, this absorbed light can be recorded as a signal to characterize the absorption on specific wavelengths [12]. Beers law states that the absorption of the UV/vis beam is proportional to the concentration of the absorbing species as expressed on equation 3.2.

$$A = \varepsilon bc \qquad \textbf{(3.2)}$$

where ε is absorbtivity as a proportionality constant, b is the pathlength, and c is the concentration of the absorbing species. The Cary 100 double beam spectrometer was used to study the valence transitions of the MX, MP, MP-5/MX and MP-15. Figure 3.8(a) shows the Agilent Technologies Cary 100 UV/Vis Spectrophotometer used in this work, and (b) its schematic diagram (b).

(a) (b)

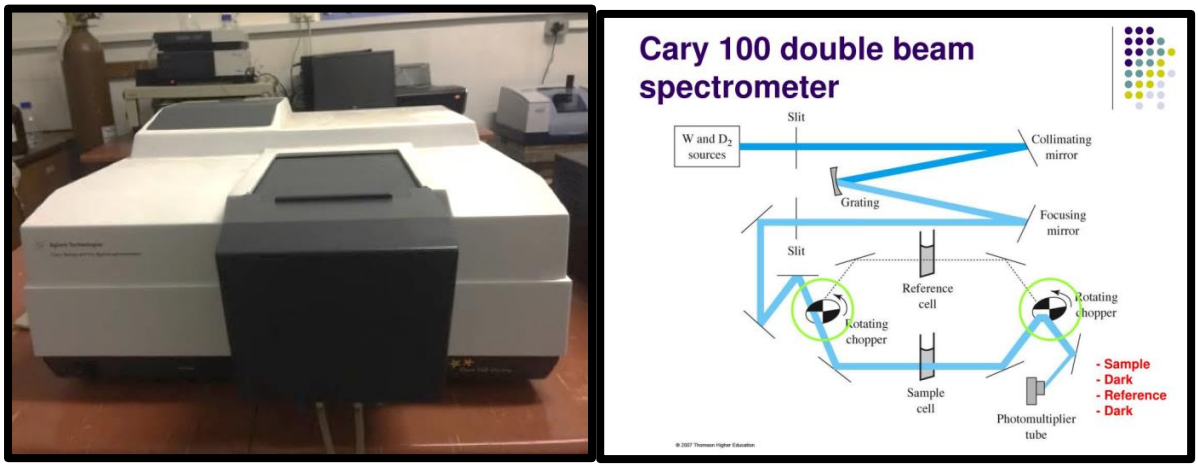

Figure 3.8: Agilent Technologies Cary 100 UV/Vis spectrophotometer (a) photo, and (b) schematic diagram [13]

3.3.1.5. X-ray Photoelectron Spectroscopy

X-ray photoelectron spectroscopy (XPS) is an expensive, quantitative, surface analytical technique that provides information on the elemental composition and chemical bonding of materials. Its principle of operation is based on the photoelectric effect. Fundamentally, when a sample is irradiated with x-rays, the kinetic energy and the number of electrons ejected from the core levels of the atoms are used to study the chemistry and electronic state of the present elements [14-15]. Thermo Scientific ESCAlab 250Xi (Figure 3.9) with a monochromatic Al Ka (1486.7 eV) source operated at 300 W under a 10^{-8} mBar vacuum pressure was used to analyse samples to determine chemical bonding and composition. The Thermo Scientific Avantage XPS Software was used for data processing.

Figure 3.9: Thermo scientific ESCAlab 250Xi XPS Microprobe [16]

3.3.1.6. Elemental Dispersive X-ray Spectroscopy

Elemental dispersive x-ray spectroscopy (EDS) is a technique commonly coupled with SEM or TEM for a qualitative and semi-quantitative detection of elements present in the sample by using the emitted secondary and backscattered electrons from the SEM or TEM microstructural image forming process. Various detectors are then used to quantify the presence of different elements [12, 14, 17]

3.3.2. Electron Microscopy Characterization

3.3.2.1. Scanning Electron Microscopy

A scanning electron microscopy (SEM) is an electron microscope technique used to obtain the surface morphology of a specimen. The surface morphology of the sample microstructure is obtained. It does so by generating a beam of electrons by an electron gun at 1-30 eV energies within in a vacuum chamber. These electrons are focused with various magnetic lenses within the

chamber to the sample/specimen stage where an interaction occurs between the sample and the electron beam. Upon interaction, the specimen can absorb reflect, and release secondary electrons which can then be detected and processed to generate an image of the surface of the sample [12, 14, 17, 18]. In this work, the FEI Nova Nanolab 600 was used for surface morphology imaging on a SEM equipped with EDS for quantitative mapping distribution of elements. Figure 3.10a shows the FEI Nova Nanolab SEM instrument that was used in this work and a corresponding schematic diagram on Figure 3.10b of the SEM instrument core components.

(a) **(b)**

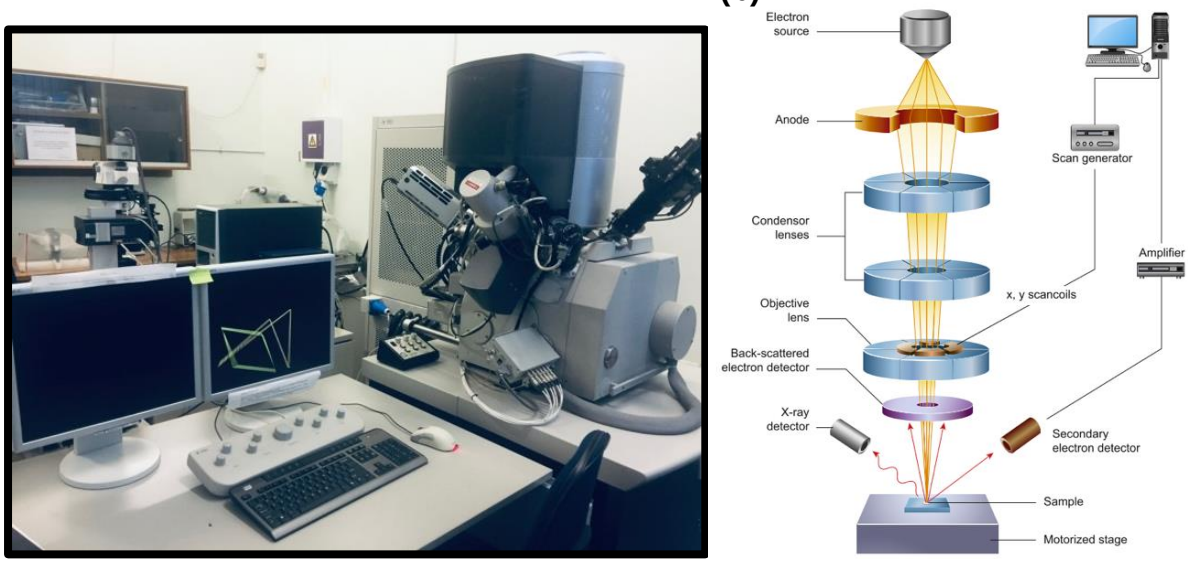

Figure 3:10: (a) FEI Nova Nanolab 600 SEM - *Wits Microscopy and Microanalysis Unit*; and (b) schematic diagram of the core components of the SEM equipment [17]

3.3.2.2. Transmission Electron Microscopy

Transmission electron microscopy (TEM) is an electron microscope technique used for the microstructural imaging of a sample at a nanoscale for obtaining the size of the particle size, microstructure, crystallinity, elemental mapping and shape of the sample. TEM uses a higher speed, high energy electron gun than SEM. The electron gun radiates the electron beam at high

energies to a thin sample for a good transmission of electrons. A charge-coupled device camera is used to form an optical image of the transmitted electrons [12,17-19]. Figure 3.11a shows the TEM equipment used in this work and Figure 3:11b shows the general schematic layout of TEM instrumentation.

(a)

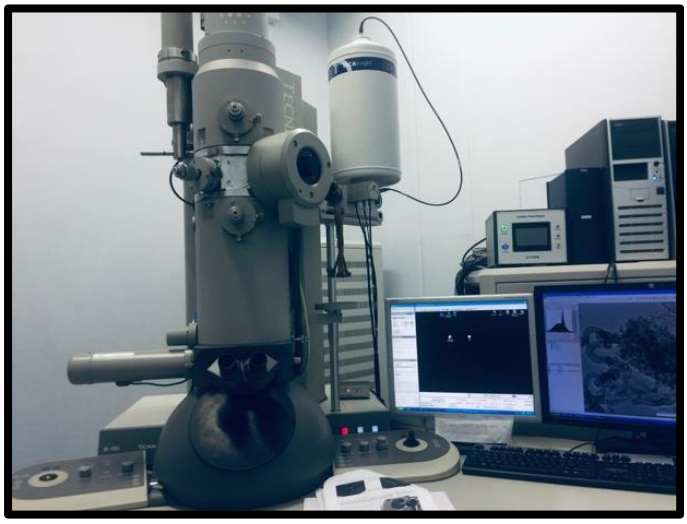

(b)

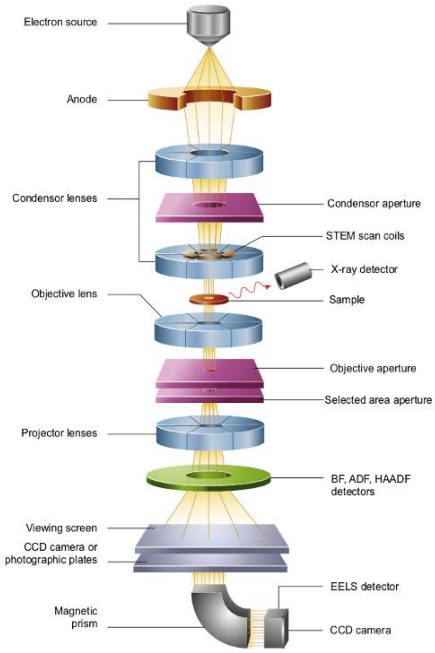

Figure 3:11: (a) FEI Tecnai T12 TEM - *Wits Microscopy and Microanalysis Unit*; and (b) schematic diagram of the core components of the TEM equipment

The FEI Tecnai T12 and the JEM-2100 JEOL field emission were used for TEM and HRTEM respectively for scoping and obtaining the microstructural features of the MAX, MX, MP-5/MX, and MP-15/MX materials. Both these instruments were operated at a 200kV acceleration voltage and the HRTEM was fitted with EDS detectors for elemental identification.

3.3.3. Physical Characterization

3.3.3.1. Brunauer-Emmet Teller Analysis

The surface area and porosity analyser used for the Brunauer-Emmet Teller (BET) analysis of the material where pore size, pore distribution and surface area were determined by the material's absorption of nitrogen gas in specified temperatures and pressure. Figure 3.12 shows the Micrometrics TriStar 3000 surface area and porosity analyser that was used under nitrogen at -196 degrees Celsius in this work. Samples were degassed for 6 hours at 80 degrees Celsius.

Figure 3.12: Micrometrics TriStar Surface Area and Porosity Analyzer

3.3.3.2. Thermo-Gravimetric Analysis

Thermal gravimetric analyser (TGA) was used to determine the thermal stability, decomposition, ash and dehydration of the material with a known gravimetry as a function of time and temperature. Figure 3:13a shows the PerkinElmer TGA400 Themogravimetric Analyzer that was used in this work

with the corresponding general schematic diagram of a TGA on Figure 3.13b. The TGA analysis was performed from 30 to 900 degrees Celsius.

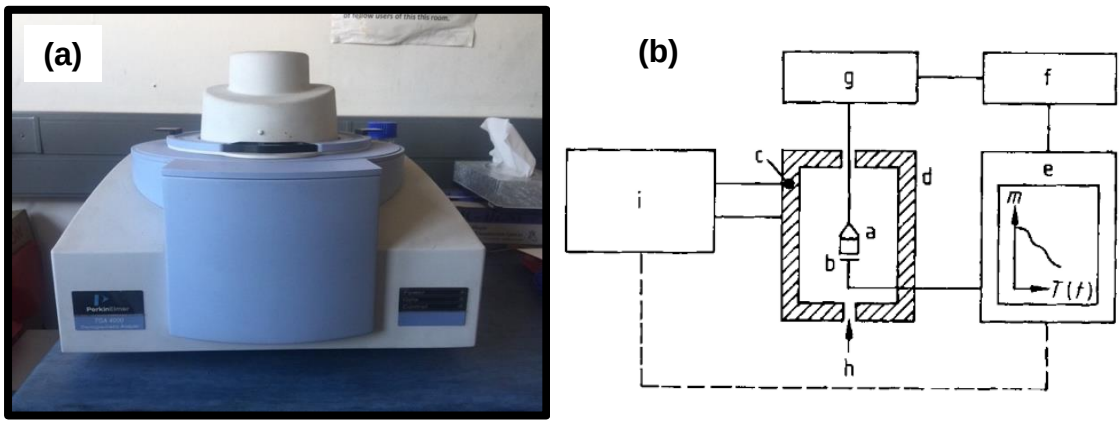

Figure 3.13: (a) PerkinElmer TGA400 Themogravimetric Analyzer, and (b) general schematic diagram of a thermobalance {a} Sample; {b} Sample temperature sensor; {c} Furnace temperature sensor; {d} Furnace; {e} Recorder or computer, logging sample mass, temperature, and time; {f} Balance controller; {g} Recording microbalance; {h} Gas; {i} Furnace temperature programmer [20]

3.3.4. Electrochemical Performance Evaluation

Commonly, to characterize electrochemical performance, two types of cell configurations are used:

i. Three-electrode cells for supercapacitor electrodes, and

ii. Two-electrode cells for supercapacitor devices.

Electrochemical performance evaluation tests were performed on a Bio-Logic® VMP300 potentiostat (Biologic, France) operated with EC-Lab software. Figure 3.14(a) shows the actual used instrument and a corresponding illustration of the workstation Figure 3.14(b). MTI three-, and two- electrode Swagelok split cells were used for testing cells.

(a) **(b)**

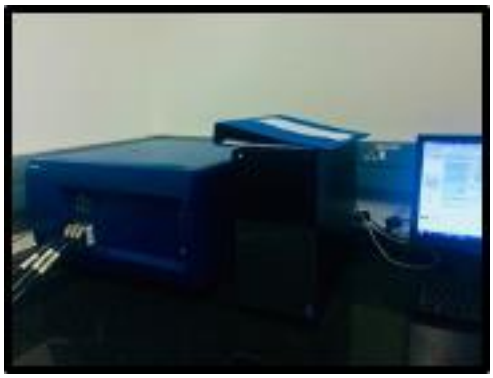

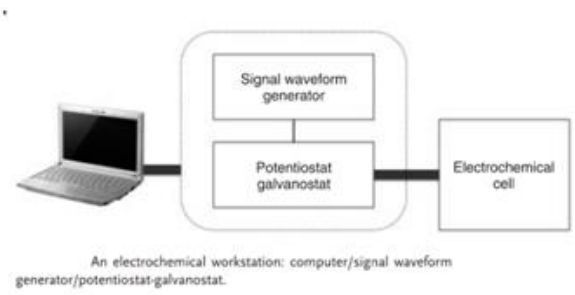

An electrochemical workstation: computer/signal waveform generator/potentiostat-galvanostat.

Figure 3.14: (a) Bio-Logic VMP300 potentiostat - *Wits Gatehouse 8th Floor;* and (b) an illustration of an electrochemical workstation [24]

The key metrics for the overall supercapacitor cell performance are: (i) Capacitance, (ii) Operation Potential, and (iii) Equivalent Series Resistance. From these key metrics, Power and Energy, Cyclic Stability and Time Constant can be established. Capacitance is the measurement of the charge stored in a device. Resistance is a general term to characterize the losses in a cell circuit – it could be from the electrode material, cell casing, current leakage, etc. Calculations of electrochemical performance evaluation of the fabricated cells were computed with data obtained from CV, GCD and PEIS [21].

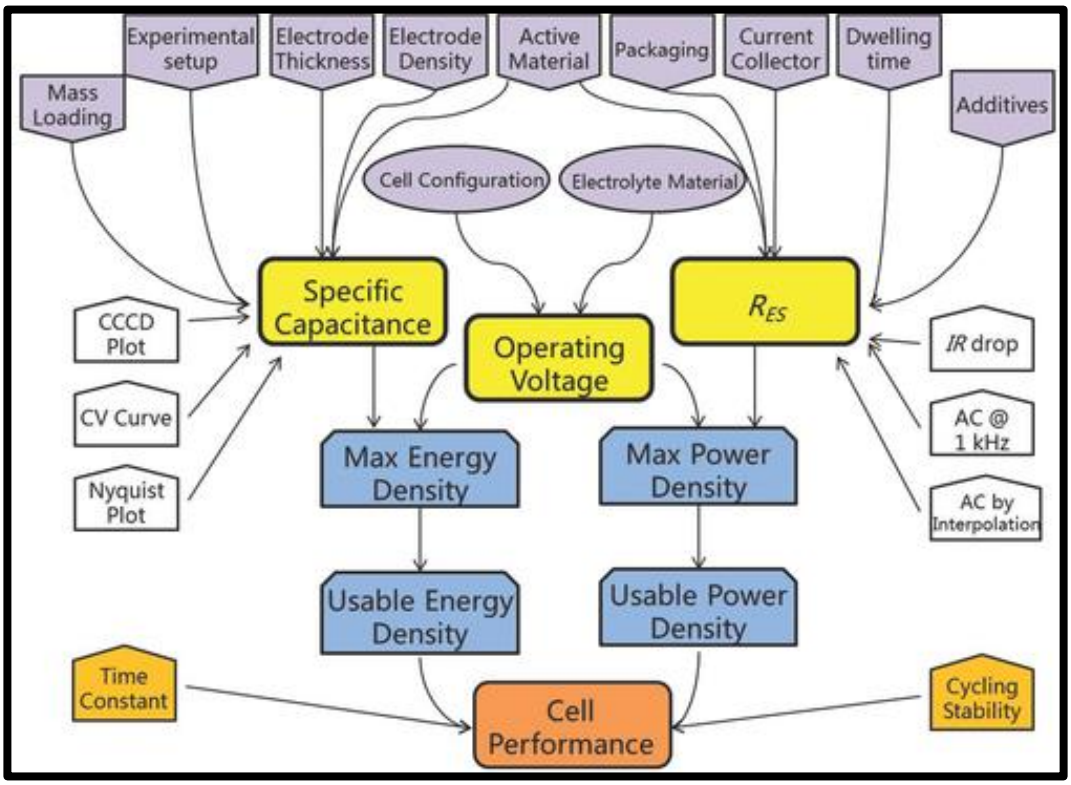

Figure 3.15: An illustration of key performance metrics, test methods, major affecting factors for the evaluation of SCs [21]

3.3.4.1. Cyclic Voltammetry

Cyclic voltammetry (CV) is a transient electrochemical performance evaluation technique that finds popular and wide application in electrochemistry research because of its versatility and efficiency [22,24] for a qualitative investigation of kinetic differences of storage mechanisms exhibited by different electrode materials when undergoing electrochemical processes and reactions, as well as quantitative computation from the obtained data. The fundamental operating principle of this technique is the application of a linear voltage ramp to a cell or an electrode between two voltage limits and then measures the current response effected by the voltage sweep. These electrochemical processes have a current response that is recorded over the duration of a reaction and are graphically recorded [24].

This chronopotentiometry technique accurately profiles the reaction kinetics of cells or electrode materials by sweeping voltage linearly at a various scan rates to induce current response which translates into a cyclic voltammogram (Figure 3.16) where current is plotted against voltage. The cyclic voltammogram's shape, curves and voltage range gives us insight of the reactions – physical and chemical – taking place at specific voltages and scan rates. The IUPAC convention standardized CV curves to represent the positive current region of the current as anodic (oxidation), and the negative current region as cathodic (reduction).

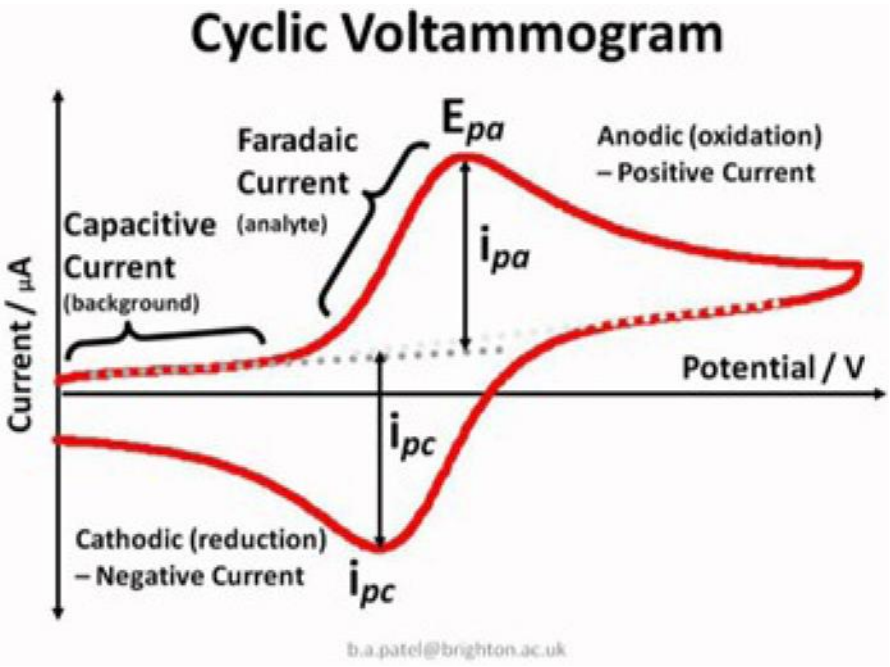

Figure 3.16: Labelled cyclic voltammograms [23]

For the quantitative interpretation of the charge storage mechanism at play, data was extracted from the peaks of the three-electrode CV curves. The aim was to separate the contributions electric double layer capacitance from pseudocapacitance. Notwithstanding the limitations of this approach, what is known is employed to reach the differentiation of these mechanisms. In EDLC

mechanism, the induced current is proportional to the scan rate. In PC mechanism, the semi-infinite diffusion cation adsorption is proportional to the square root of the scan rate [25]. So, to explore this, because the power law as expressed in equation 3.3, is used to relate the current (í) and scan rate (v), to distinguish non-diffusion limited component from diffusion controlled component where *a* and *b* are adjustable parameters.

$$í = av^b \qquad \textbf{(3.3)}$$

This distinguishing is achieved by determining the *b*-values obtained at different potentials. When *b = 1*, the process is non-diffusion limited (capacitive), when *b = 0.5*, the process is diffusion controlled.

To have a deeper understanding of the energy storage mechanisms taking place according to the cyclic voltammograms, two components of the charge storage mechanisms were deconvoluted from the obtained CV curved scanned at different scan rates. The method employed for this was developed by Conway and Dunn. In their work, the two components (pure capacitive processes, and diffusion controlled faradaic processes) were related to the corresponding a and b values stated on equation 3.3. So, the total measured current as a function of potential i(V) is equal to the sum of two components, such that:

$$i(V) + k_1v + k_2v^{1/2} \qquad \textbf{(3.4)}$$

where i is the current intensity, v is the scan rate, k1 and k2 are independent constants. Thus, the linear dependency of the current intensity, as a function of potential, to the scan rate of k1 constitutes capacitive contribution while the linear dependency of the current intensity, as a function of potential, to the

square root of scan rate provides the diffusion-controlled faradaic contribution [26].

Additionally, CV can provide insight on what an optimal cell voltage window is, the reaction reversibility and capacitive/pseudocapacitive behaviour of the electrodes.

Capacitance from CV can be calculated according to these equations:

$$C_T = \frac{\Delta Q}{\Delta V} = \frac{\int_0^{2Vo/V} |i| dt}{2Vo} \qquad \textbf{(3.5)}$$

$$C_{sp} = \frac{\mathrm{C}}{\mathrm{S}} \qquad \textbf{(3.6)}$$

Where C_T is capacitance (F),

3.3.4.2. Galvanostatic Charge-Discharge

The galvanostatic charge-discharge (GCD) technique is a chronoamperometric also known as the constant current charge-discharge (CCCD) technique. It employs the application of a controlled current and measures voltage to characterize the cell or electrode performance. Key parameters that are obtainable from this technique are capacitance, resistance and cyclability [24].

From the slope of the GCD profile, capacitance, C, (F) and gravimetric specific capacitance (F/g) are calculated as follows:

$$C = \frac{I\Delta t}{\Delta V} \qquad \textbf{(3.7)}$$

$$C_{sp} = \frac{4C}{S} \qquad \textbf{(3.8)}$$

where I is the applied constant current (A), Δt is the discharge time (s), V is the operating widow voltage (V), and S is the active electrode mass (g)

The cell series resistance (Ohms), power density (W/kg), energy density (Wh/kg) and maximum power (W/kg) can be calculated according to these equations:

$$\mathrm{ESR} = \frac{V_{iRdrop}}{2I} \qquad \textbf{(3.9)}$$

$$E_{sp} = \frac{C\Delta Vmax^2}{2m} \times \frac{1000}{3600} \qquad \textbf{(3.10)}$$

$$P_{sp} = \frac{Esp \times 3600}{\Delta t} \qquad \textbf{(3.11)}$$

$$P_{max} = \frac{Vmax^2 \times 1000}{4mESR} \qquad \textbf{(3.12)}$$

where Q is charge (C), V is the potential (V), V_o the is the peak voltage (V) , V_{iR} is the internal resistance voltage drop (V), Vmax is the maximal applicable (V), m is the active material mass (g), I is current (A), t is time (s), z is impedance (Ohms), f is frequency (Hz), ESR is (Ohms).

GCD was performed at current densities ranging from 0.05 to 10 A/g with electrolyte specific set potentials to profile the charge/discharge, galvanostatic cyclability and synergistic contributions of the components in the material.

3.3.4.3. Potentio Electrochemical Impedance Spectroscopy

Electrochemical Impedance Spectroscopy (EIS) is one of the most super powerful techniques used by electrochemists. This technique is classified as a stationary electrochemistry technique. It is a highly sensitive, non-destructive technique that is able to characterize the electrical properties of materials together with their interfaces. EIS tests are performed under a steady state, over a wide response time for an accurate measurement of electrochemical processes. The general principle underlying the operation of this technique is that a small electric signal with a specific frequency for excitation is imposed on the working electrode. The excitation signal can be current or voltage, meaning that either voltage or current respectively can be subsequently measured as an output signal. Commonly, potential control – referred to as Potentio EIS (PEIS) - is widely employed and was chosen for undertaking studies in this work. So, voltage is applied at specific frequencies. This voltage consists of two components: a sinusoidal periodic signal with small amplitudes; and direct current signal independent of time [27-28]. This applied voltage in a range of frequency results into a measurable current response when applied to a working electrode. On that basis, impedance is the characterization of electrochemical processes by measurement of electrical responses to an applied potential. EIS investigations in this work were conducted at 3 mV amplitude between 10 mHz and 100 kHz to

investigate the characteristic of electrode-electrolyte interface, ion mobility and adsorption/desorption to electrode surface.

3.3.5. Fabrication of Electrochemical Cells

3.3.5.1. Slurry Preparation

For the coating of the current collector to prepare electrodes for electrochemical performance testing, a slurry was prepared by mixing the active material (MX, MP-5/MX, or MP-15/MX), PVDF as a binding agent, and carbon black as a conductive agent in 80:15:5 ratio. NMP was used as a wetting agent.

3.3.5.2. Electrode Preparation

To prepare electrodes, carbon paper was cut into 12mm diameter discs and coated with the slurry using a spatula. The loading amount of the electrode material slurry was 2 mg for three electrode systems and 0.2 mg for symmetrical devices.

3.3.5.3. Electrolyte Preparation

All electrolyte was prepared in the lab using electrolyte salts and deionized water following a simple wet chemistry procedure. Figure 3.17 shows the work done at the lab bench in electrolyte preparation and testing.

1mol.l^{-1} electrolytes were prepared:

i. Acidic – H_2SO_4
ii. Neutral – Li_2SO_4
iii. Alkaline – LiOH

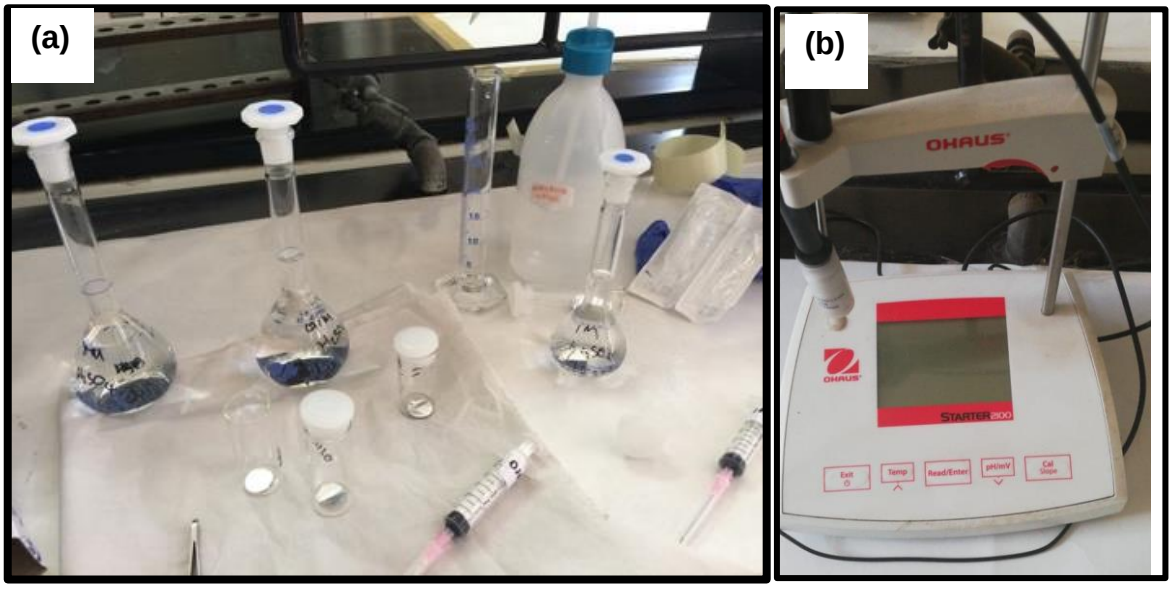

Figure 3.17: Aqueous electrolyte solutions and preparation(a) glassware and (b) pH meter used for electrolyte test – Wits School of Chemistry

3.3.5.4. Swagelok Two and Three Electrode Cell Assembly

Stainless steel split cells were used for two and three electrode electrochemical performance testing. Figure 3.18 shows the (a) schematic diagram of the two-electrode split cell [29], (b) two-electrode split cells, (c) schematic of the three-electrode split cell [30], and (d) three-electrode split cell.

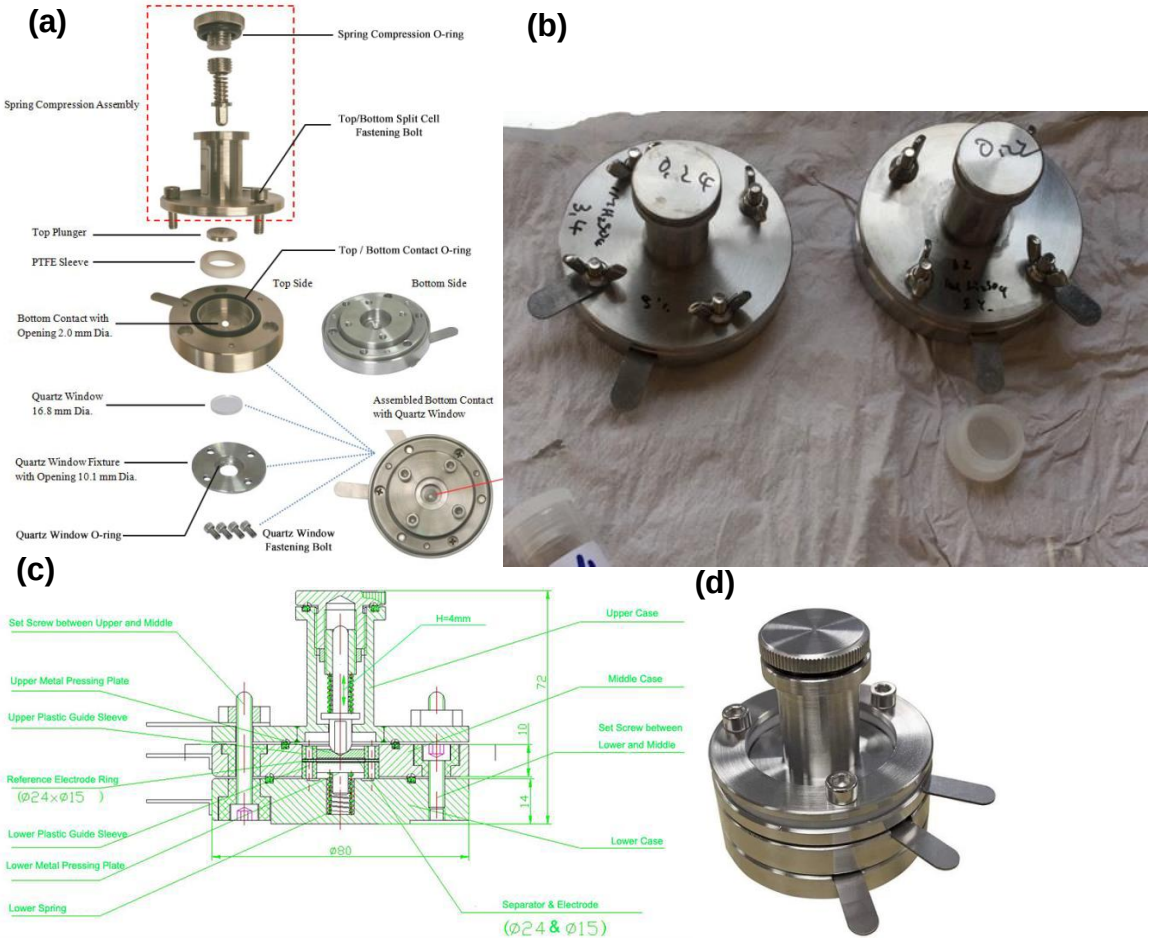

Figure 3.18: (a) schematic diagram of the two-electrode split cell [29], (b) two-electrode split cells, (c) schematic of the three-electrode split cell [30], and (d) three-electrode split cell [31]

3.4. Reference List

[1] Millipore Corporation. (2008). 'DIRECT-Q ® 3 SYSTEM DIRECT - Q3 UV SYSTEM' Rev. 3. France: Millipore Corporation. Available at: https://www.manualslib.com/manual/685315/Millipore-Direct-Q-3-System.html?page=2#manual [accessed: September 2018]

[2] Ramachandran, R. and Wang, F. (2018) 'Electrochemical Capacitor Performance: Influence of Aqueous Electrolyte', In: Supercapacitors Theoretical and Practical Solutions (Edited by L. Liudvinavičius) Intenhopen, pp. 51-68. doi: 10.5772/intechopen.69087. Available at: https://www.intechopen.com/books/supercapacitors-theoretical-and-practical-solutions [accessed 23 September 2018]

[3] Liu, F., Zhou,A., Chen, J., Zhang,H., Cao, J., Wang, L., and Hu, Q. (2016*) 'Preparation and methane adsorption of two-dimensional carbide Ti_2C'*, Adsorption. Springer US, 22(7), pp. 915–922. doi: 10.1007/s10450-016-9795-8.

[4] Ghidiu, M., Lukatskaya, M.R., Zhao, Q-M., Gogotsi, Y., and Barsoum, M.W. (2014). *'Conductive two-dimensional titanium carbide "clay" with high volumetric capacitance'*, *Nature. Nature Publishing Group*, 516(7529), pp. 78–81. doi: 10.1038/nature13970.

[5] Bunaciu, A. A., Udriştioiu, E. Gabriela and Aboul-Enein, H. Y. (2015) 'X-Ray Diffraction: Instrumentation and Applications'*, Critical Reviews in Analytical Chemistry*, 45(4), pp. 289–299. doi: 10.1080/10408347.2014.949616.

[6] Chauhan A, and Chauhan, P. (2014) 'Powder XRD Technique and its Applications in Science and Technology', *Journal of Analytical & Bioanalytical Techniques*, 5(6). doi: 10.4172/2155-9872.1000212.

[7] Mourdikoudis, S., Pallares, R. M., and Thanh, N. T. K. (2018) 'Characterization techniques for nanoparticles: Comparison and complementarity upon studying nanoparticle properties', *Nanoscale. Royal Society of Chemistry*, 10(27), pp. 12871–12934. doi: 10.1039/c8nr02278j.

[8] Griffiths, P. R. and de Haseth, J. A. (2007). Fourier Transform Infrared Spectrometry. Second Edi. Hoboken, New Jersey: John Wiley & Sons, Inc. doi: 10.1111/j.1600-0447.1967.tb10181.x.

[9] Zinn, B. (2004) *'Bruker Tensor 27 FT-IR & OPUS Data Collection Program'*, Stanley group for catalytic studies, pp. 1–47. doi: 10.1071/EA03051.

[10] Bumbrah, G. S. and Sharma, R. M. (2016) 'Raman spectroscopy – Basic principle, instrumentation and selected applications for the characterization of drugs of abuse', *Egyptian Journal of Forensic Sciences.* The International Association of Law and Forensic Sciences (IALFS), 6(3), pp. 209–215. doi: 10.1016/j.ejfs.2015.06.001.

[11 HORIBA Jobin Yvon. (2013). 'LabRAM HR Evolution User Manual', France: HORIBA Jobin Yvon SAS. Available at: https://www.horiba.com/en_en/products/detail/action/show/Product/labram-hr-evolution-1083/ [accessed: 16 October 2019]

[12] Srivastava, R. (2012) 'Synthesis and characterization techniques of nanomaterials', *International Journal of Green Nanotechnology: Biomedicine*, 4(1), pp. 17–27. doi: 10.1080/19430892.2012.654738.

[13] Chalondra, N. (2014). ‘UV-visible molecular absorption spectroscopy’, SlideServe, available at: https://www.slideserve.com/chalondra-naiser/uv-visible-molecular-absorption-spectroscopy. [accessed: 12 September 2018]

[14] Mourdikoudis, S., Pallares, R. M. and Thanh, N. T. K. (2018). ‘Characterization techniques for nanoparticles: Comparison and complementarity upon studying nanoparticle properties’, *Nanoscale. Royal Society of Chemistry*, 10(27), pp. 12871–12934. doi: 10.1039/c8nr02278j.

[15] Smith, E. (2017) ‘An introduction to X-ray photoelectron spectroscopy’, University of Nottingham, Nanoscale and Microscale Research Centre. Available at: https://www.nottingham.ac.uk/nmrc/documents/training-series/introduction-to-xps-principles.pdf [accessed: 18 October 2018]

[16] https://www.thermofisher.com/order/catalog/product/SID-10148252 [accessed: 19 August 2020]

[17] B.J. Inkson. (2016). ‘Scanning electron microscopy (SEM) and transmission electron microscopy (TEM), In: *Materials Characterization Using Nondestructive Evaluation (NDE) Methods*. (Edited by Hübschen, G., Altpeter, I., Tschuncky, R., and Herrmann, H-G.), Woodhead Publishing, Duxford, United Kingdom

[18] Nasrazadani, S., and Hassani, S., (2016). Handbook of Materials Failure Analysis with Case Studies from the Oil and Gas Industry, *Elsevier Ltd.* pp 1-430

[19] Dahmen, U. (1989) ‘Transmission electron microscopy characterization of precipitates’, *Ultramicroscopy*.1-2(30). pp 102-115. doi: 10.1016/0304-3991(89)90178-2.

[20] Günzler, H. and Williams, A. (2001) *Handbook of Analytical Techniques, Handbook of Analytical Techniques*. WILEY-VCH Verlag GmbH. doi: 10.1002/9783527618323.

[21] Zhang, S. and Pan, N. (2015) 'Supercapacitors performance evaluation', *Advanced Energy Materials*, 5(6), pp. 1–19. doi: 10.1002/aenm.201401401.

[22] Bard, A.J., and Faulkner, L.R., (2004). 'Dopamine detection using mercaptopropionic acid and cysteamine for electrodes surface modification', *'Electrochemical methods: fundamentals and applications',* Second edition. New York: John Wiley & Sons, Inc. pp. 227

[23] Khan M.S., Asif, A., Khawaldeh, S., and Tekin, A. (2018). *Journal of Electrical Bioimpedance*, 9(1), pp. 3–9. /doi.org/10.2478/joeb-2018-0002

[24] Pandolfo, T., Ruiz, V., Sivakkumar, T., and Nerkar, J., 'General Properties of Electrochemical Capacitors', In: Supercapacitors Materials, Systems, and Applications (Edited by: Lu, M., Béguin, F. and Frackowiak, E.), Wiley-VCH Verlag GmbH & Co. KGaA pp. 69-109.

[25] Liu, J., Wang, J., Xu, C., Jiang, H., Li, C., Zhang, L., Lin, J., Shen, Z.S. (2018) 'Advanced Energy Storage Devices: Basic Principles, Analytical Methods, and Rational Materials Design', *Advanced Science*, 5(1). doi: 10.1002/advs.201700322.

[26] León-Reyes, Á., Epifani, M., Chávez-Capilla, T., Palma, J., and Díaz, R. (2014) 'Analysis of the different mechanisms of electrochemical energy storage in magnetite nanoparticles', *International Journal of Electrochemical Science*, 9(7), pp. 3837–3845.

[27] Taberna, P. L., Simon, P. and Fauvarque, J. F. (2003). 'Electrochemical Characteristics and Impedance Spectroscopy Studies of Carbon-Carbon

Supercapacitors', *Journal of The Electrochemical Society*, 150(3), p. A292. doi: 10.1149/1.1543948.

[28] Yu, A., Chabot, V. and Zhang, J. (2017) *'Electrochemical supercapacitors for energy storage and delivery: Fundamentals and applications, Electrochemical Supercapacitors for Energy Storage and Delivery: Fundamentals and Applications'*. Roca Raton, Flourida: CRC Press. pp. 1-355doi: 10.1201/b14671.

[29] MTI Corporation. (2017) 'Three-electrode split cell', Available at: https://www.mtixtl.com/images/products/detail/ThreeElectrodeStructure.jpg [accessed: 29 August 2019] https://www.mtixtl.com/images/products/detail/3e.jpg

[30] MTI Corporation. (2017). 'Three-electrode split cell', Available at: https://www.mtixtl.com/images/products/detail/ThreeElectrodeStructure.jpg [accessed: 29 August 2019]

[31] MTI Corporation. (2017). 'Two-electrode split cell', Available at: https://www.mtixtl.com/images/EQ-STC-QW_assembly2.jpg [accessed: 29 August 2019]

CHAPTER 4

RESULTS & DISCUSSION

MATERIALS CHARACTERIZATION

4.1. Spectroscopic Characterization

4.1.1. Powder X-Ray Diffraction Spectroscopy

The PXRD patterns of the parent, hexagonal MAX phase Maxthal 211 (Ti_2AlC) powder; the as-synthesized pristine MXene (Ti_2CT_x); as well as the 5 and 15 wt.% NiTpyzPz incorporated Ti_2CT_x (MAX, MX, MP-5/MX, and MP-15/MX) are displayed on Figure 4.1. The obtained PXRD patterns as shown on the diffractogram confirm the crystalline nature and structural order of the materials. The as-obtained commercial parent hexagonal Ti_2AlC composition was confirmed by pronounced (002), (101), (102), (103), (106), (107), (110) characteristic diffraction peaks according to the (JCPDS PDF card no. 01-081-8106) [1]; common to the commercially obtained Ti_2AlC phase composition characterization from other studies [1, 5]. Ti_3AlC_2, which is a diatomic titanium layer, heavier expression of Ti_2AlC is present as a minor impurity as indicated according to the (JCPDS PDF card no. 01-074-8806) with (002) and (105) as characteristic peaks to indicate this impurity in the lighter Ti_2AlC.

After Al selective etching by in-situ HF (LiF-HCl) method, also known as the alkali solution etching [6-8], the successful synthesis of MXene is suggested by the weakening and significant disappearance of MAX characteristic peaks and the kept (002) peak that moved to lower two theta angle [1, 2, 7]. This (002) peak move to lower two theta angles imply increase in the interlayer spacing, indicating an

increase of the lattice parameter which characterizes the conversion of the MAX to MX nanosheets which have the =O, -OH, -Cl and -F surface termination groups which replace the Al thus showing the multilayer nature of the resulting material. The resulting nanosheet surfaces are known to be negatively charged and hydrophilic. This electronegativity and hydrophilicity make MX to be able to absorb water and polar organic solvents which is useful for further expanding the interlayer spacing that can be quantified to approximate the expansion [9, 10].

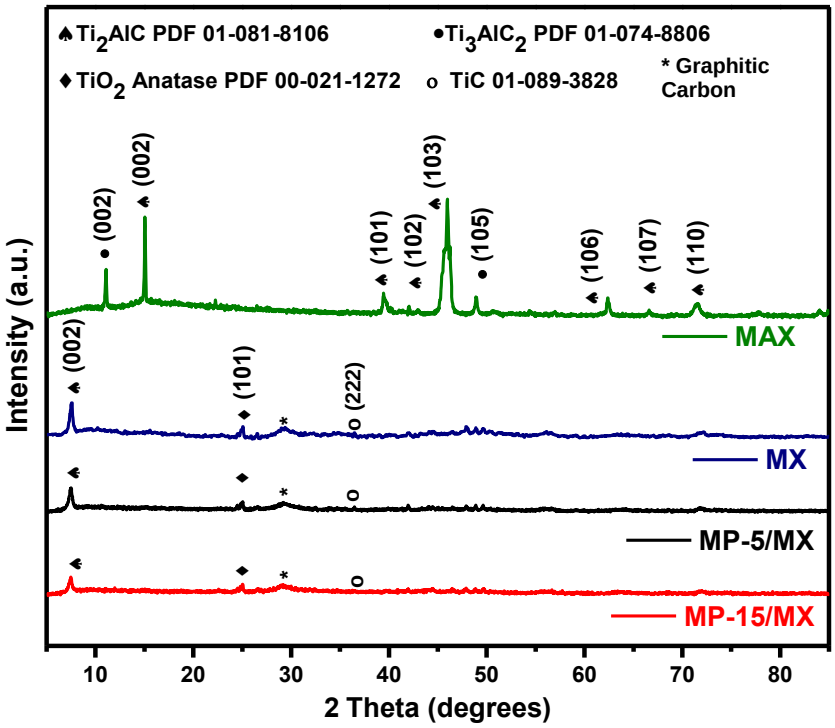

Figure 4.1: PXRD diffractogram of MAX, MX, MP-5/MX, and MP-15/MX 0 – 85 º

As shown on Figure 4.2, the MAX phase, MXene, and modified MXene (002) peaks at 15.05°, 7.60°, 7.51°, and 7.48° were identified and used to determine the interlayer spacing. Similar to the work of Rakhi. [2], the interlayer spaces were calculated to be 6.83, 13.50, 13.66, and 13.71 Å respectively using Bragg's law. Firstly, a remarkable increase of 6.65 Å is evident for the evolution of MAX to MX.

Also, there is a subsequent increase of 0.16 Å from MX to MP-5/MX, and 0.21 Å for MX to MP-15/MX. These basal plane spaces show us that as the Al is etched out and replaced with surface termination groups and that the subsequent treatment of delamination by intercalating the MP complex further widens the interlayer spacing which proves to be important in ion transport for electrochemical energy storage electrode materials because it means there are more active sites for redox reactions together with an increased surface area. The success of the typical in-situ HF in selectively etching out Al from the Ti_2AlC crystal structure is explicated. The main peaks that remain unchanged but exhibit a downshift after exfoliation indicate that the crystallinity of the material remains unchanged. The obtained diffractogram also indicates the presence of Ti_3AlC_2 MXene as a secondary phase in the precursor which is however present in minor quantities. Titanium oxide anatase peaks at approximately 25 degrees are identified. This (101) TiO_2 anatase phase formation is attributed to the local heat that is released during the exothermic reaction of MXene with in-situ HF exfoliation in aqueous media – oxygen dissolved in water acts as an oxidizing agent. The material storage in ambient conditions can also contribute to titanium oxides formation [10,11]. The broad diffraction peak at 29° on the MX, MP-5/MX and MP-15/MX spectra indicate the presence of graphitic carbon as a result of the A-group element exfoliation. The TiC (222) phase is also present and assigned at 36°. This TiC phase is common in the samples of the titanium carbide MXene. NiTpyzPz was not detected using the XRD technique.

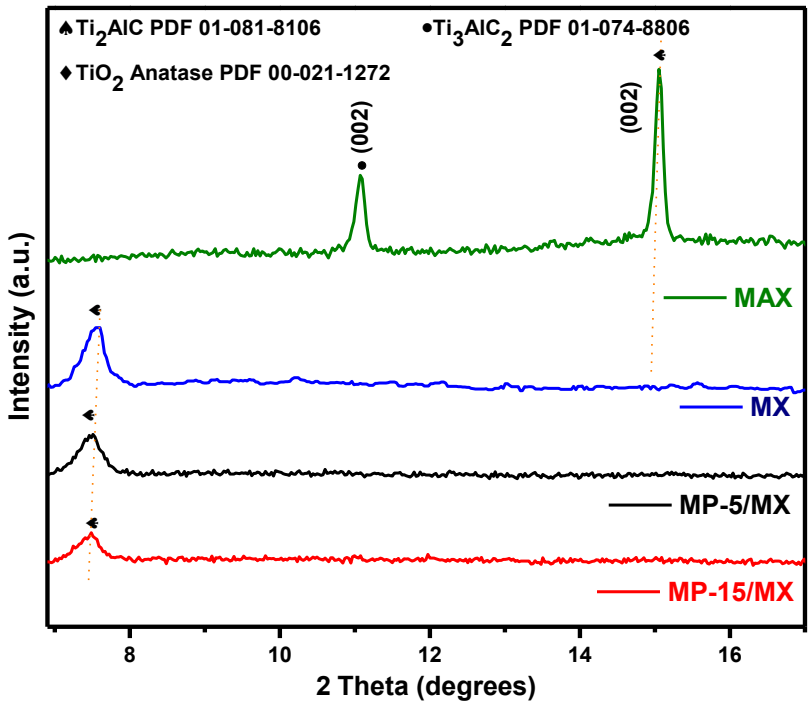

Figure 4.2: PXRD diffractogram of MAX, MX, MP-5/MX, and MP-15/MX (002) shift

4.1.2. Raman and Fourier Transform Infrared Spectroscopy

Raman spectral studies of the materials MAX, MX, MP-5/MX, MP-15/MX and MP are carried out based on the obtained spectral information as displayed on Figure 4.3. The parent MAX Raman spectra projects three peaks centred at 147, 265, and 382 cm ^{1}. These peaks, herein referred to as Raman-active modes ω1, ω2 & ω3, ω4, are consistent with literature as descriptive peaks indicating the shear (in-plane) and longitudinal (out-of-plane) vibrations of Ti and Al atoms in Ti_2AlC which the XRD spectral data indicated as present [12]. Post the selective etching of the Al from Ti_2AlC, and subsequent treatments of the resulting MXene, the observation from the obtained Raman spectra for MX, MP-5/MX, and MP-15/MX is that the ω1, ω2 & ω3, ω4 modes move to lower frequencies and become more broader indicating the preferential removal of Al, and newly formed surface

termination group vibrations while the original hexagonal structural order of MAX is maintained.

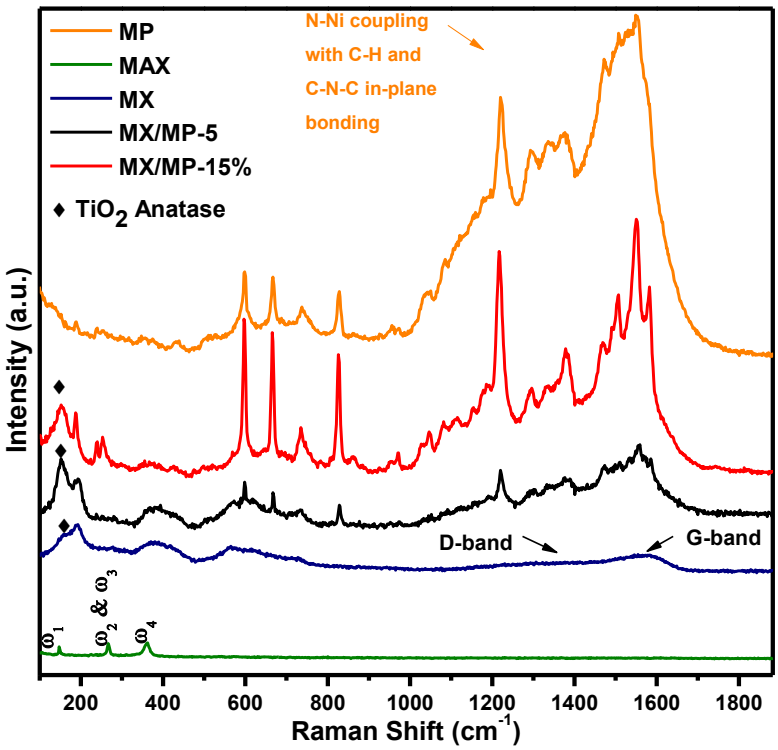

Figure 4.3: Raman spectra of MP, MAX, MX, MP-5/MX, and MP-15/MX

The further evaluation of the MX, MP-5/MX, and MP-15/MX reveals that the upshift and broadening of ω1, ω2 & ω3, ω4 at 190, 384, 584 cm^{-1} modes is accompanied with the formation a small peak at 729 cm^{-1} attributed to C-C vibrations, as well as weak peaks at 1276 and 1583 cm^{-1} which are commonly referred to as the D and G band in carbon characterization, especially in characterizing graphene. The peaks at 190, 384, and 584 are respectively attributed to Ti-C vibration, C E_g vibrations of O termination groups or A_{1g} vibration of O atoms. Regarding the two D and G weak peaks we postulate that the desired MXene similar to graphene in terms of structure has some disordered sp2 hybridized carbon to a lesser extent as peaks are relatively very weak. This disorder might be in the nonstoichiometric Ti_xC_y

or carbon that might have fragmented during the harsh exfoliation process when the M-A metallic bond was broken. Furthermore, MP-5/MX and MP-15/MX show the combination of MX and MP Raman peaks. From this observation we realize consistency of the MX pattern even after the incorporation of the MP and what we derive from this is that the MX nature is maintained as in the XRD analysis. The nickel(II) tetrapyrazinoporphyrazine Raman spectra exhibits several multiple sharp peaks which are evident in the MP-5/MX and increasingly in the MP-15/MX material. According to Lekitima [13] for similarly metalated tetrapyrazinoporphyrazine organic compounds such as CoNiTpyzPz , the strong peak at approximately 1532 cm^{-1} can be related to the C-N-C stretch and C-N bond coupling, while the peak at 1383 cm^{-1} is mainly due to the involvement of the stretching of pyrroles and N-Ni bonds with C-H and C-N-C bonds in-plane bonding. The four noticeable peaks in the 560 to 890 cm^{-1} regions can be attributed to the expanding of the pyrrole rings and stretching N-Ni.

The FTIR spectra shown on Figure 4.4 was recorded to supplement Raman spectral data and confirm functionalities of the materials. As it is with the Raman spectra in terms of MP peaks showing on MP-5/MX, and MP-15/MX at varying intensities, a similar trend is observed. The probed functionalities are indicated at respective wavenumbers (cm^{-1}) with their functional groups accordingly indexed: 755 aromatic C-H, 822 1.2 disubstituted aryl, 858 1.3 disubstituted aryl, 1040-1055 aliphatic fluoro stretch, 1086 amine stretch, 1100 secondary alcohol, 1208 primary amine C-N stretch, 1256 aromatic primary amine stretch, 1286 aromatic secondary amine, 1367 aromatic tertiary amine,1450 methylene C-H bend, 1545 aromatic nitro group, 1640 C=N amine bend , 1650 N-H bend amine. As

expected these peaks at respective bands provide insight into how MP retained its functionality as we incorporated it into the host MXenes at different proportions. It is worth noting that the peaks that the multiple bands presented at 1200-1600 cm^{-1} with their respective indexes can be attributed to the rotational and stretching vibrations of the amine and amide groups in the pyrazino and pyrrolic heterocyclic groups of the nickel(II) tetrapyrazinoporphyrazine. MAX and MX FTIR spectra are considerably featureless.

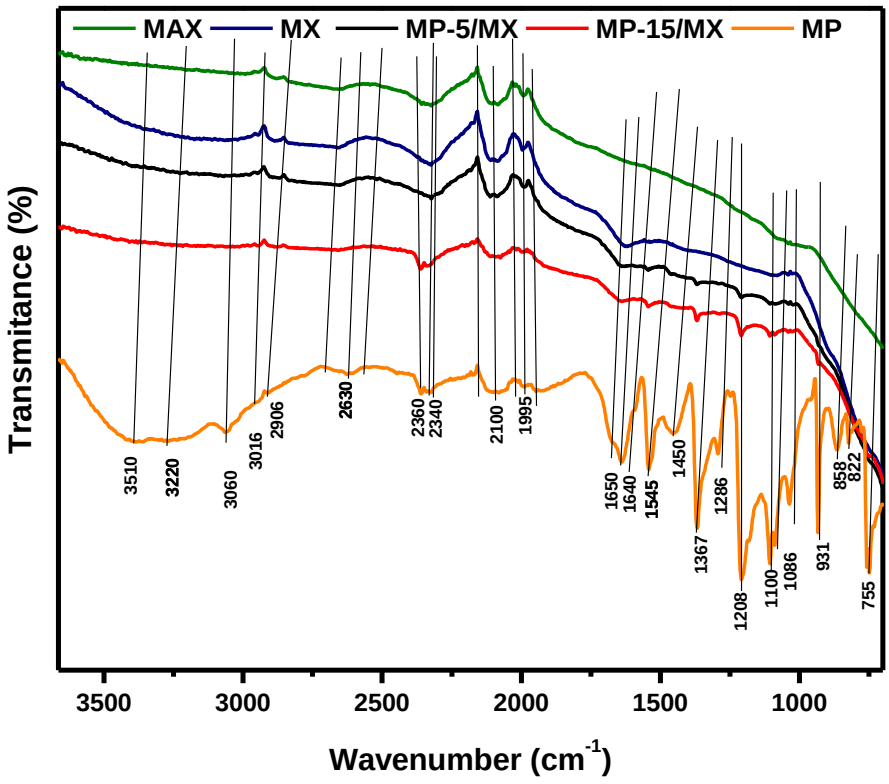

Figure 4.4: FTIR spectra of MP, MAX, MX, MP-5/MX, and MP-15/MX

4.1.3. Ultraviolet-Visible Spectroscopy

The UV-Vis spectra shown on Figure 4.5 was used to evaluate the electronic transition properties of MP and MXene based samples including the parent MAX. The electronic transition activity of MP upon UV-Vis excitation is characteristic of molecules in a class of transition metal macrocyclic complexes with MN-4 moieties such as metalloporphyrins and metallophtalocyanines which exhibit two set of bands: the B bands (also known as Soret bands) in the blue wavelength region and Q bands in the visible region of the spectrum. The absorbance band shown between 623 and 659 nm is the characteristic absorption split Q band peak which is attributed to the aggregation. In addition to the pronounced Q bands, B band at 310 nm is observed and is indicative of the coupling of electrons of nitrogen atoms to the π system. These electronic absorption peaks are more visible on MP-15/MX than on MP-5/MX as is FTIR and Raman spectroscopy peaks. The MP/MX interaction is made possible by the π-stacking between the electron rich aromatic rings in porphyrazine ligand and the hybrid electronic surface termination functionalities on the MX sheets.

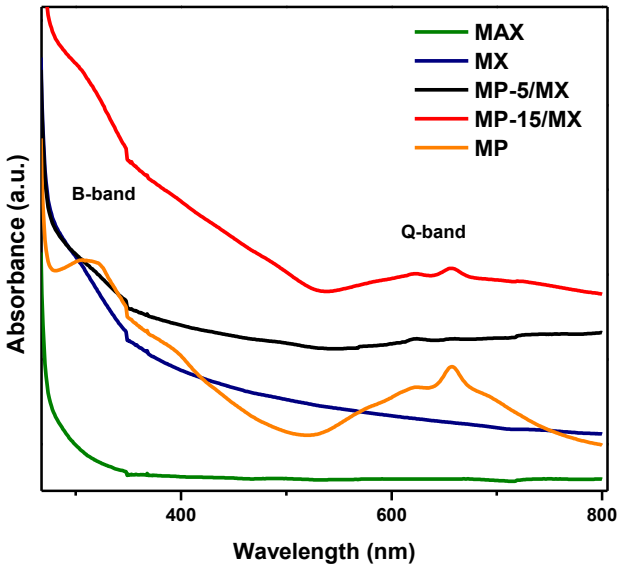

Figure 4.5: UV/Vis spectra of MP, MAX, MX, MP-5/MX, and MP-15/MX

4.1.4. X-Ray Photoelectron Spectroscopy

X-ray photoelectron spectroscopy (XPS) was the spectroscopic technique used at the very last stage of this research after all electrochemical performance evaluation characterizations were completed because of the scarcity of this technique and required costs for its access. Initially, it was employed to probe the surface chemical composition and valence states for MP, MX, MP-5/MX and MP-15/MX samples, respectively.

4.1.4.1. MP - XPS Characterization

MP Survey

The survey scan spectra of MP shown in Figure 4.6 indicates the presence of Ni 2p1/2, Ni 2p1/2, Ni 2p3, Ba 3d5/2, Fe 2p3/2, Mn 2p3/2, O 1s, N 1s, C 1s and Ni 3p in the surface bonding of the MP material.

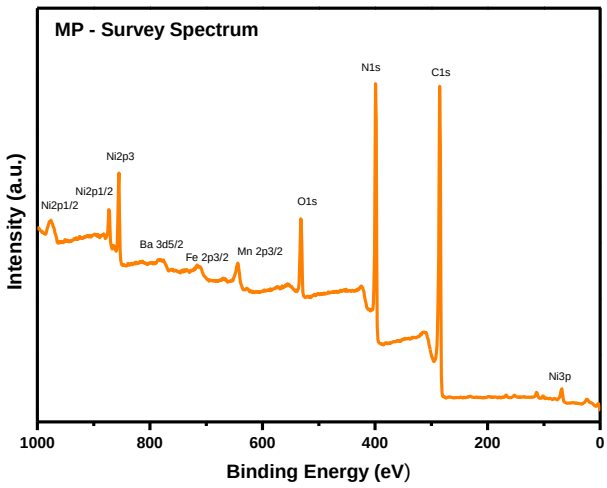

Figure 4.6: XPS survey spectra of MP

Table 4.1 shows the surface elemental identification of MP with C, N, O, and Ni as the constituent elements of focus in this study as identified on the scan survey spectra, Figure 4.6. The binding energies of C, N, O, and Ni are 285.0, 398.9, 531.5 and 855.2 eV respectively. According to the components peak fit, C 1s has an atomic percentage of 63 followed by N 1s, O 1s and Ni 2p3 having photoelectron emission percentages of 28.5, 6.8 and 1.5 respectively. These atomic values correspond well, as a composition estimation, with the elemental ratio of the MP as calculated according to the elemental ratio of $C_{24}N_{16}H_8Ni$, C:N:H = 4:2:1. The presence of O1s is expected and can have its origins from the MP synthesis reactions. The precursor chemicals nickel dichloride hexahydrate and ethylene glycol, as well as the methanol involved in washing processes have oxygen functionalities.

Table 4.1: Surface elemental identification and quantification of MP

Name	**Peak BE (eV)**	**Atomic %**
C 1s	285.0	63.2
N 1s	398.9	28.5
O 1s	531.5	6.8
Ni 2p3	855.2	1.5

The high-resolution fitted spectra of C 1s, N 1s, O 1s and Ni 2p is shown in Figures 4.7a-d. The fitted spectra components are displayed on table 4.2 with their respective binding energies. The chemical nature of the macrocycle complex is explicated according to the high-resolution spectra of components as plotted and

gaussian fitted on Figure 4.7a-d. The summary of the high-resolution spectral data showing the peak position binding energies and atomic percentage is also provide on table 4.2.

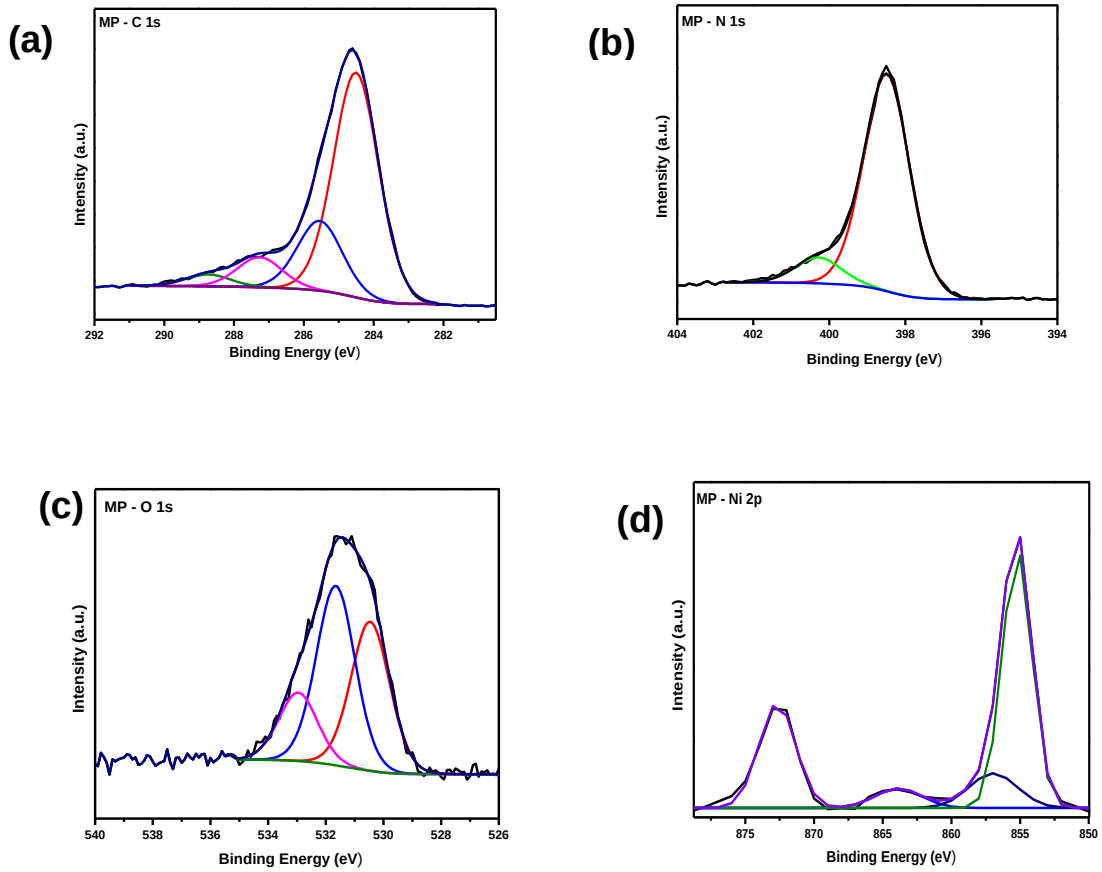

Figure 4.7: XPS high resolution spectra of MP (a) C 1s, (b) N 1s, (c) O 1s, and (d) Ni 2p

Table 4.2: Peak identification and quantification of MP

Name	Peak BE (eV)	FWHM (eV)	Atomic %
C1s (C-C)	284.5	1.5	41.6
C1s (C-O)	285.5	1.5	12.9
C1s (C=O)	287.3	1.5	5.6
C1s (O-C=O)	288.7	1.5	2.2
N1s (Organic N)	398.5	1.4	26.1
N1s (Organometallic N)	400.3	1.4	3.1
O1s (Metal Oxide)	530.5	1.6	2.6
O1s (Metal Oxide; Organic C-O)	531.7	1.6	3.1
O1s (Organic C=O)	533.0	1.6	1.2
$Ni2p_{3/2}$ (Organic Ni)	855.0	1.4	1.6
$Ni2p_{3/2}$ satellite	863.0	-	-
$Ni2p_{1/2}$ satellite	874.1	-	-

MP - C 1s region

The chemical nature of MP regarding C is revealed by the main peak at 285.0 eV as fitted on Figure 4.7a. According to the high-resolution C 1s fit, there are four peaks at 284.5, 285.5, 287.3, and 288.7 eV. These carbon peaks may be related alpha and beta carbon atom bonds [14] with imide groups ideally and carbonyl groups as a result of oxidation contamination in the synthesis process.

MP - N 1s region

Figure 4.7b shows the high-resolution spectra of N 1s with a gaussian fit of the main peak at 398.9 eV which is characteristic of the N of the tetrapyrrolic macrocycle of porphyrin and porphyrin derivative macrocyclic molecules [15]. The gaussian fit of this peak deconvolutes two peaks at 398.5 eV pyridinic, and 400.5 eV pyrrolic that are characteristic of the pyridinic and pyrrolic nitrogen of MP respectively [14-19]. Furthermore, there is a peak fit at 400.3 eV that can be associated with the valence excitations pi to pi* as a result of pyrrolic nitrogen core ionization as it interacts with the metal [15]. The fitting of the N 1s is well matched with a symmetric gaussian peak shape with respective binding energy that are well associated with the diamagnetic nature of the quadridentate nickel-tetrapyrrolic macrocyclic bond [14-15].

MP - O 1s region

A closer look at the survey spectra of MP on Figure 4.6 shows an O 1s main peak at 531.5 eV as tabulated on table 4.1. A closer look of this peak, as shown on the high-resolution spectra of this O 1s peak, Figure 4.7c reveals peak 530.5, 531.7 and 533.0 eV as deconvoluted. These three peaks indicate the presence of O and its bonding states that are primarily from the contamination in the MP synthesis procedure.

MP - Ni 2p3 region

The Ni 2p spectrum of MP on Figure 4.7d shows three core levels of Ni: Ni $2p_{3/2,}$ Ni $2p_{3/2}$ satellite, and Ni $2p_{1/2}$ satellite at 855.0, 863.0 and 874.1 eV, respectively.

These three core level energies are consistent with literature of Ni(II) macrocyclic complexes and are indicative of the spin -orbit doublet [15].

The XPS analysis of the MP complex confirms the successful synthesis of MP as the main peaks are the same as those obtained in the literature of the MP closest analogue with the 0.1 eV shift in the Ni $2p_{3/2}$ binding energy which may be indicative of a stronger sigma metal to nitrogen bond as a result of the metal protonation by four pyrrolic rings bonded to each other by imide groups [15, 18].

4.1.4.2. MX - XPS Characterization

MX Survey

Figure 4.8 is the survey spectrum of the pristine MX. In this spectrum, the presence of C 1s, O 1s, Ti 2p, F 1s and Al 2p core levels is displayed and detailed on table 4.3 to show peak binding energies and the atomic percentage of specific elements.

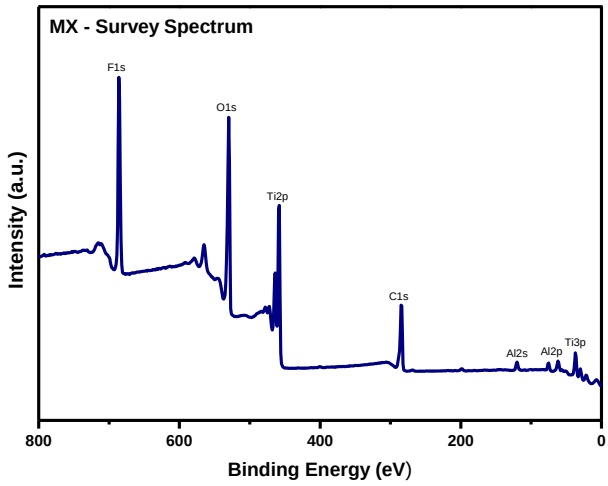

Figure 4.8: XPS survey spectra of MX

Table 4.3: Surface elemental identification and quantification of MX

Name	**Peak BE (eV)**	**Atomic %**
O 1s	530.1	30.8
C 1s	284.5	28.3
F 1s	685.7	24.5
Ti 2p	458.3	12.2
Al 2p	75.2	4.1

Figure 4.9a-e plots show the high-resolution spectra of Al, C, Ti, and O respectively and their respective component peak-fitting indicative of valence state and moiety of each element detected on the surface of the as-synthesized material. The elemental identification and quantification details of these deconvoluted plots are shown on table 4.3 providing the atomic percentage of O 1s as the highest at 30.8% followed by 28.3% for C 1s, 24.5% for F 1s, 12.2% for Ti 2p, and 4.3% for Al 2p. The high presence of oxygen is assumably indicative of the high oxygen terminated functionalities on the MX surface as well as the inevitable oxidation of MX when stored in ambient storage environment. Carbon is in the structure of MX, in binary titanium carbide structure, as well as graphitic carbon from the aggressive etching treatment that the MAX undergoes as described in the synthesis protocol as Al is etched out of selectively. F comes from the in-situ HF (LiF-HCl) etching solution. Although undesired, the F termination of MX surfaces amongst other termination groups (O, and Cl) is well documented in literature [20-25].

Figure 4.9a-e plots are high-resolution spectra of Al 2p, C 1s, Ti 2p, O 1s, and F 1s photoemission regions with table 4.4 providing the corresponding peak identification as deconvoluted for elaborate peak quantification and assumed bond assignments.

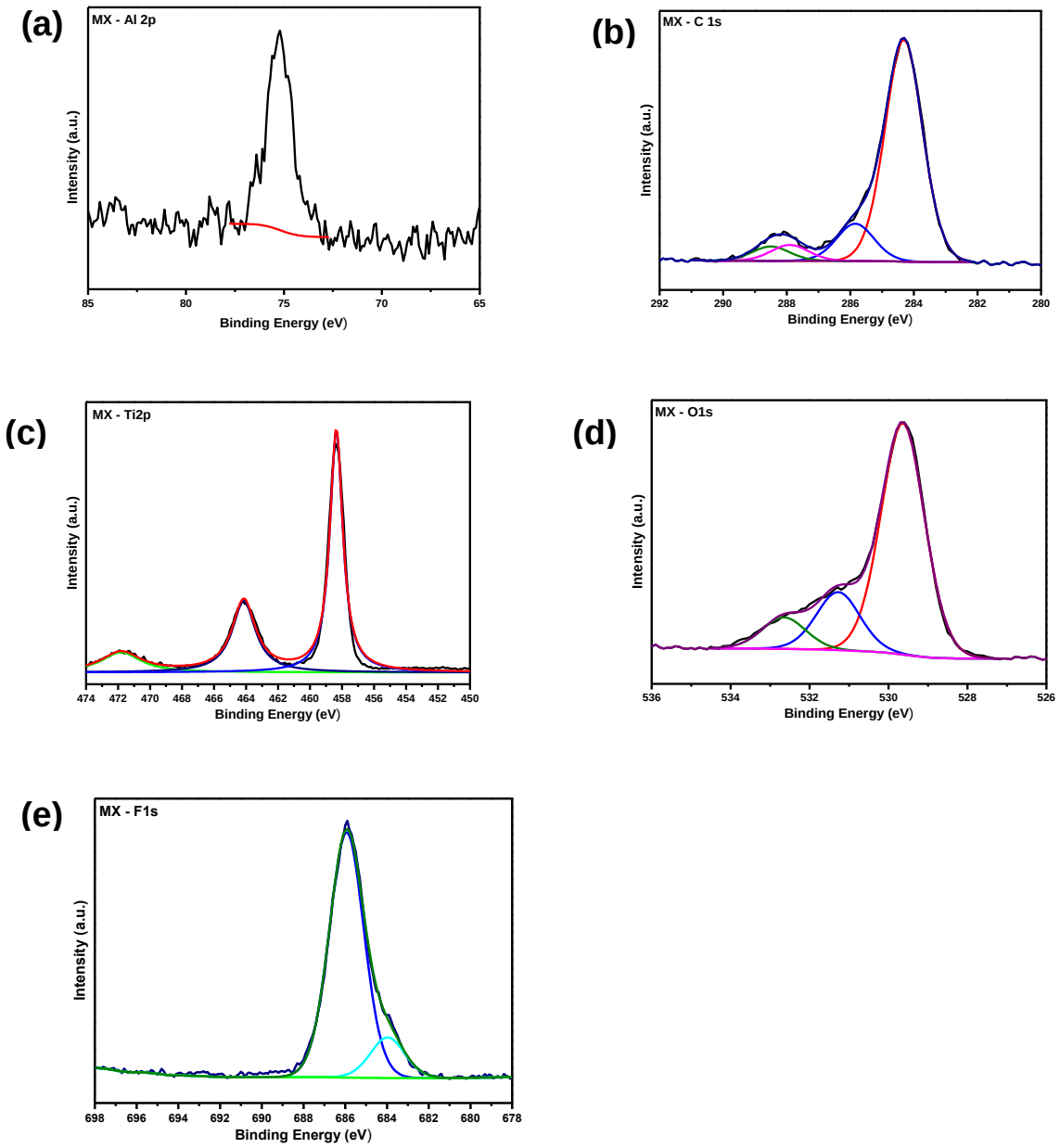

Figure 4.9: XPS high resolution spectra of MX (a) Al 2p, (b) C 1s, (c) Ti 2p, (d) O 1s, (e) F 1s

Table 4.4: Peak identification and quantification of MX

Name	Peak BE (eV)	FWHM (eV)	Atomic %
Al2p (Organic Al; AlF3)	75.2	1.4	4.6
C1s (C-C)	284.3	1.4	23.0
C1s (C-O)	285.8	1.4	3.9
C1s (C=O)	287.9	1.4	1.7
C1s (O-C=O)	288.5	1.4	1.5
Ti2p3 (TiO2)	458.3	1.1	11.9
O1s (Metal Oxides)	529.6	1.3	21.4
O1s (Metal Oxides; Organic C-O)	531.3	1.3	5.4
O1s (Organic C=O)	532.6	1.3	2.9
F1s (Fluoride)	684.0	1.9	3.4
F1s (Fluoride)	685.9	1.9	20.4

MX - Al 2p region

Figure 4.9a presents the high-resolution spectrum of the Al 2p region. The moiety of Al_2O_3 can be assigned to the Al peak energy of 75.2 eV. Although present with the lowest atomic percentage, the presence of this aluminium oxide is indicative of the in homogenic nature of MX as Al formations from the synthesis process are still present post Al etching [22].

MX - C 1s region

The C 1s region photoemission peaks, and peak fittings are shown on Figure 4.9b. Table 4.6 indicates the peak binding energies for this high-resolution spectra of C 1s at 284.3 eV for the C-C bond, 285.8 eV for the C-O bond, 287.9 eV for the C=O, and 288.5 eV for the O-C=O [21-23]. The C-C bond is assumably from the graphitic carbon present from the selective etching process when Al is exfoliated from the parent MAX phase. The carbon-oxygen bonds are expected as oxygen terminated titanium carbide is expected in the MX materials from the DMF solvent used in delamination.

MX - Ti 2p region

The high-resolution spectra of Ti 2p for the MX material is displayed on Figure 4.9c showing the prominent TiO_2 peak at 458.3 eV [22]. This reveals that at the time that XPS analysis was performed, the oxidation process due to the ambient storage conditions had advanced on the material. Proving the proneness of the Ti_2CT_x to oxidise faster than the heavier Ti-based MXene counterparts. Two more peaks above 460.0 eV are identified at 464.1 eV and 471.8. The peak at 464.1 eV can be assigned to the Ti 2p1/2, and the peak at 471.8 can be assigned as the Ti 2p satellite shake-up peak.

MX - O 1s region

The peak fits for the O 1s emission on Figure 4.9d at 529.6 eV, 531.3 eV and 532.6 eV indicate the presence of TiO_2 [22], C-Ti-Ox and C-Ti-OH [21-23] moieties. This provides a positive indication that MXene nanostructure are present in the MX material even as oxidation due to ambient conditions advanced.

MX - F 1s region

Figure 4.9e shows an intense peak at 684.0 eV which is indicative of the inorganic interaction (C-Ti-F_x) of fluorine atoms with titanium and a minor one at 685.9 eV emerging from the Al-F_x moiety. This Al-F bond reveals the formation of metal inorganic fluorides from the in-situ HF wet chemical exfoliation process [21, 25].

4.1.4.3. MP-5/MX - XPS Characterization

MP-5/MX Survey

Figure 4.10 is the survey spectra of MP-5/MX. On this spectrum the presence of C 1s, O 1s, F 1s, Ti 2p, Al 2p, and are N 1s identified on binding energies 75.1, 284.8, 530.3, 685.6, 485.2, 399.0 eV respectively.

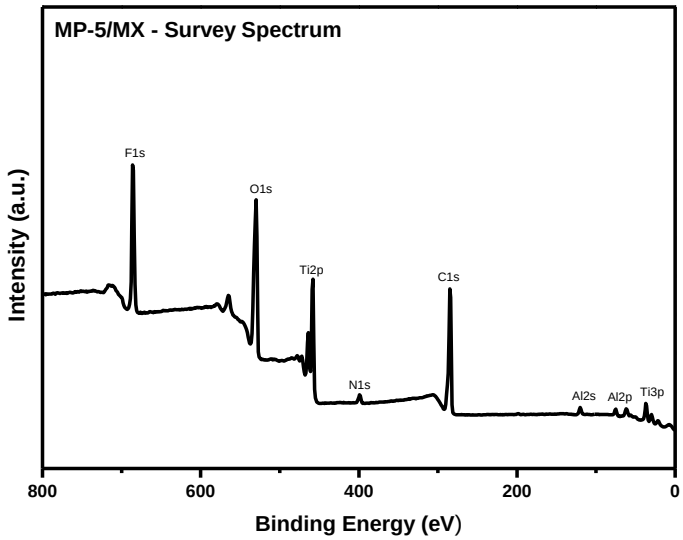

Figure 4.10: XPS survey spectra of MP-5/MX

As shown on table 4.5, carbon makes up 45.2%, the greatest constituency, of the MP-5/MX material. The oxygen atomic percentage follows at 26.2% and then fluorine, titanium, aluminium and nitrogen making up 15.8, 7.8, 3.0 and 2.0 %.

Table 4.5: Surface elemental identification and quantification MP-5/MX

Name	**Peak BE (eV)**	**Atomic %**
C1s	284.8	45.2
O1s	530.3	26.2
F1s	685.6	15.8
Ti2p	458.2	7.8
Al2p	75.1	3.0
N1s	399.0	2.0

MP-5/MX - Al 2p region

The Al 2p high resolution spectra shown on Figure 4.11a shows the main peak at 75.2 eV. According to the survey spectra, Al accounts for 3.0% of the sample. This indicates the high success of the milder in-situ HF etching method and its capability as a safer yet strong Al etchant synthesis protocol.

MP-5/MX - C 1s region

Figure 4.11b shows the high-resolution spectra of C 1s. In this spectrum, the main peaks are deconvoluted to characterize C 1s moieties present in the MP-5/MX material. As presented on table 4.6, there are four binding energies showing different C 1s chemical bonds. At 284.8, 285.8, 287.9, and 288.5 eV the detected

moieties are C-C, C-O, C=O, and O-C=O just as in the MX material. However, in MP-5/MX there is higher carbon content because of the presence of MP.

MP-5/MX - Ti 2p3 region

The main Ti 2p peak at 458.2 eV is observed in the high-resolution spectra of Ti 2p for the MP-5/MX material as presented on Figure 4.11d. For the MX material, Ti 2p accounts for 11.9% of the sample atomic composition, whereas for the MP-5/MX material there is a decrease in the Ti 2p element because of the sample composite that is 95% MX and 5% MP. We also note that the addition of MP in the MX material effects no observable changes on the Ti 2p binding energy. Two more peaks above 460.0 eV are identified at 463.9 eV and 471.7. The peak at 463.9 eV can be assigned to the Ti 2p1/2, and the peak at 471.7 can be assigned as the Ti 2p satellite shake-up peak.

MP-5/MX - O 1s region

The O 1s region high resolution spectra shown on Figure 4.11e has 3 peaks as fitted. At 529.5 eV, a pronounced peak attributed to TiO_2 suggests that even in the presence of MP, the oxidation of Ti_2CT_x by ambient storage conditions is still possible. The intrinsic MX chemical bonding is retained even as MP is introduced to this host material. This is observed from the C-Ti-Ox and C-Ti-OH peak fittings at 531.3 eV and 528.8 eV.

MP-5/MX - F 1s region

Figure 4.11f is the high-resolution spectrum of F 1s for the MP-5/MX material. The presence of F comes from the wet chemical etching synthesis of MX and it is

interesting to note that the C-Ti-Fx and AlFx chemical bonding as identified and quantified at 683.8 and 685.6 eV peaks is still present even after the intercalation of MX with MP.

MP-5/MX – N 1s region

Figure 4.11c shows the high resolution spectra of the N 1s surface chemical state of the MP-5/MX material. According to the MP-5/MX survey spectra at 399.0 eV, N 1s accounts for the atomic % of 2.0. The deconvoluted peaks can associated with the pyridinic nitrogen at 398.4 eV and pyrrolic nitrogen-metallic bonding at 400.6 eV.

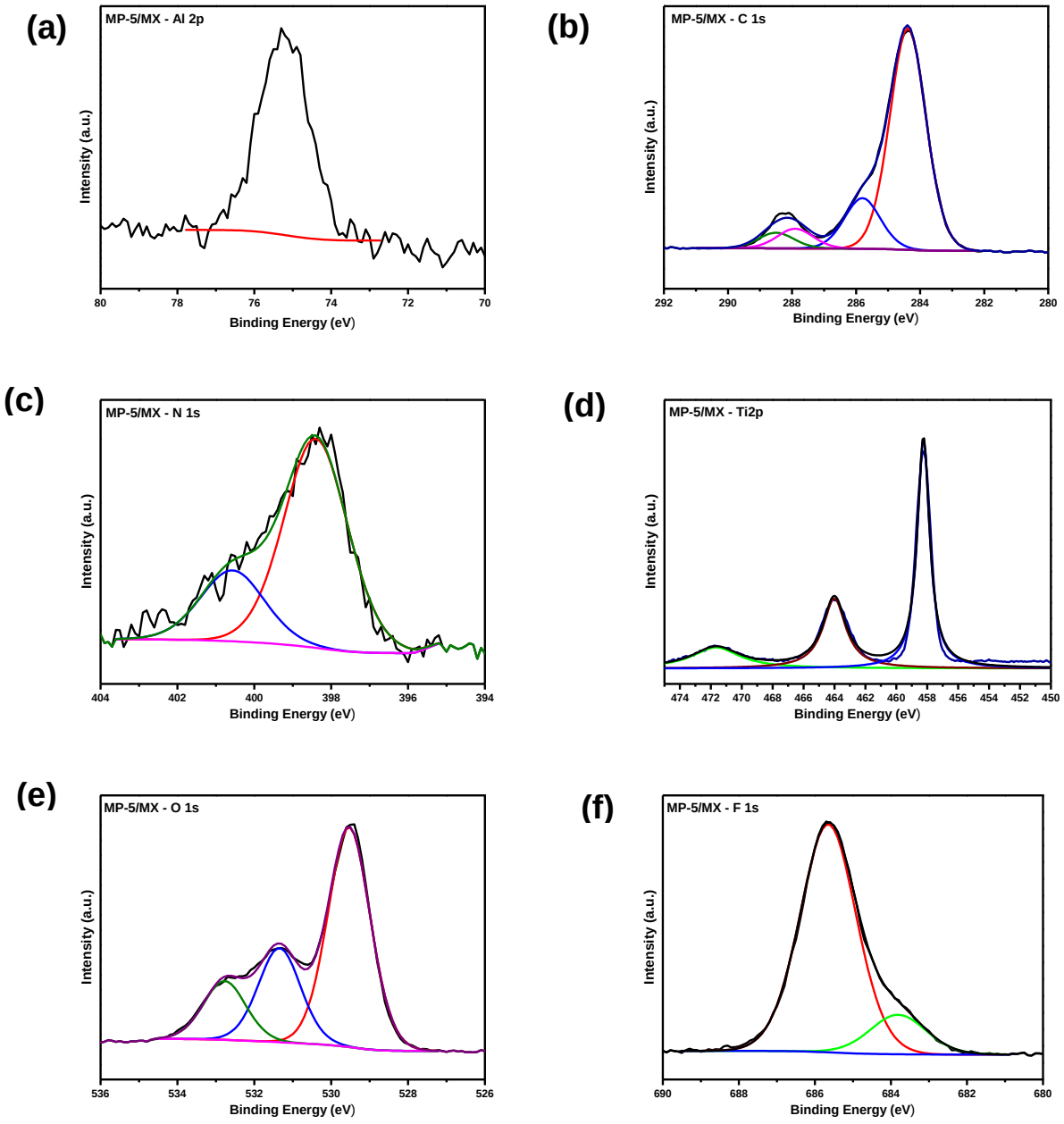

Figure 4.11: XPS high resolution spectra of MP-5/MX (a) Al 2p, (b) C 1s, (c) N 1s, (d) Ti 2p, (e) O 1s, and (f) F 1s

Table 4.6: Peak identification and quantification of MP-5/MX

Name	Peak BE (eV)	FWHM (eV)	Atomic %
Al2p (Organic Al; AlF3)	75.2	1.5	3.0
C1s (C-C)	284.4	1.3	31.6
C1s (C-O)	285.8	1.3	7.2
C1s (C=O)	287.9	1.3	2.8
C1s (O-C=O)	288.5	1.3	2.2
N1s (Organic N)	398.4	2.0	1.7
N1s (Organometallic N)	400.6	2.0	0.6
Ti2p3 (TiO2)	458.2	1.1	8.1
O1s (Metal Oxides)	529.5	1.3	15.4
O1s (Metal Oxides; Organic C-O)	531.3	1.3	6.6
O1s (Organic C=O)	532.8	1.3	4.1
F1s (Fluoride)	683.8	1.7	2.5
F1s (Fluoride)	685.6	1.7	14.2

4.1.4.4. MX/MP-15 XPS Characterization

MP-15/MX Survey

Figure 4.12 shows the survey spectrum of MP-15/MX. This spectrum is like that of MP-5/MX, except that there is higher nitrogen intensity from the tetrapyrrolic, pyrazino and imide bridges indicating the higher presence of MP. The addition of MP also results in lower MX in sample matrix compared to the MP-5/MX sample. As a result, the Ti intensity is lower compared to the Ti in MP-5/MX because of different sample compositions. Table 4.7 provides a summary of atomic percentages of the C, O, F, Ti, N and Al element present in the MP-15/MX.

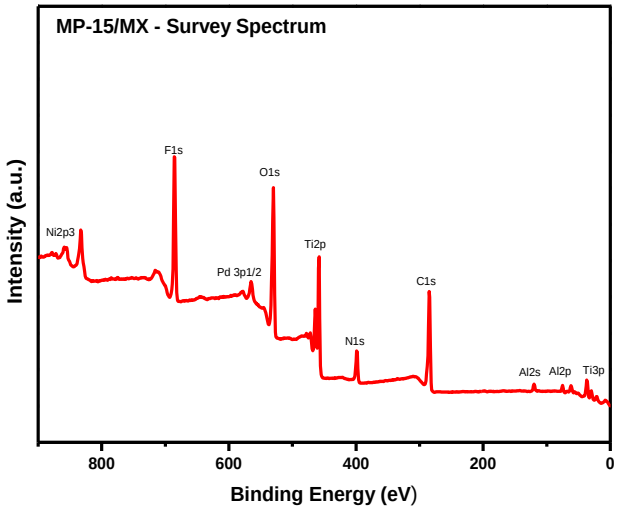

Figure 4.12: XPS survey spectra of MP-15/MX

Table 4.7: Surface elemental identification and quantification of MP-15/MX

Name	**Peak BE (eV)**	**Atomic %**
C1s	284.8	39.7
O1s	530.1	23.9
F1s	685.4	17.7
Ti2p	458.2	8.3
N1s	398.8	7.6
Al2p	75.1	2.9

MP-15/MX - Al 2p region

The high-resolution Al spectrum shown on Figure 4.13a is the photoemission region fit for Al 2p at 75.3 eV assignable to AlFx. This is the lowest atomic percentage of the elements present in the material as an impurity from the Al that was not completely etched from the etching step of the synthesis.

MP-15/MX - C 1s region

The C 1s region, Figure 4.13b, comprises of four carbon moieties attributed to C-C, C-O, C=O, and O-C=O at 284.4, 285.8, 287.9, and 288.5, respectively. They are the same as the moieties for MP-5/MX.

MP-15/MX - N 1s region

The N 1s region of MP-15/MX, presented on Figure 4.13c, shows pronounced peaks at 398.4 and 400.6 eV. These two are assignable to the pyridinic nitrogen bond (398.4 eV) and the quadridentate nickel-tetrapyrrolic macrocyclic bond (400.6 eV). An observation on the atomic % of N 1s for the MP-5/MX and MP-15/MX materials is that based on tables 4.5 and 4.7, there is an increase in the atomic % from 2.0 (MP-5/MX) to 7.6% (MP-15/MX). This is significant of the MP presence in the MX material surfaces. Although nickel is not identified on the MP-5/MX and MP-15/MX XPS spectra, increased atomic % of MP indicates an anticipated change as the nitrogen bonds are constituent to the Ni metal macrocyclic ligand.

MP-15/MX - Ti 2p3 region

The Ti in MP-15/MX, as expected, is lower than in MP-5/MX because for MP-15/MX there is 85% MX and 15% MP. So, MP-15/MX has the lowest MX compared to both pristine, and MP-5/MX. The chemical bonding observed from the high resolution of the Ti 2p3 photoemission region resembles the one for MX, and MP-15/MX, suggesting that the addition of MP effects no chemical bonding change on the titanium moieties. Figure 4.13e shows the high resolution spectra for Ti 2p. Two more peaks above 460.0 eV are identified at 464.1 eV and 471.7. The peak at 464.1 eV can be assigned to the Ti 2p1/2, and the peak at 471.7 can be assigned as the Ti 2p satellite shake-up peak.

MP-15/MX - O 1s region

Figure 4.13e is the high-resolution spectra of the MP-15/MX O 1s photoemission region. On it three fitted peaks can be observed. These peaks at 529.6, 531.3, and 532.7 eV are assignable to TiO2, C-Ti-Ox, and C-Ti-OH. Titanium oxide emerges is formed during the highly exothermic etching process of the MAX precursor as well as from the oxidation of Ti_2CT_x in ambient conditions. The C-Ti-Ox and C-Ti-OH moieties are the chemical bonds that prove the presence of MXene nanostructures.

MP-15/MX - F 1s region

Because MX was synthesized by selective etching of Al from the MAX precursor with in-situ HF, the surface termination groups of MX have the F functionalities. An interesting observation, as shown on Figure 4.13f, is that the F 1s photoemission region of MP-15/MX has two well fitted peaks at binding energies 683.9 and 685.7

eV. These two peaks at respective binding energies indicate the C-Ti-F and AlFx bonds. C-Ti-F is of the MX sheet terminated with F, while the AlFx is the impurity from the etched Al material bound to F from the etching solution.

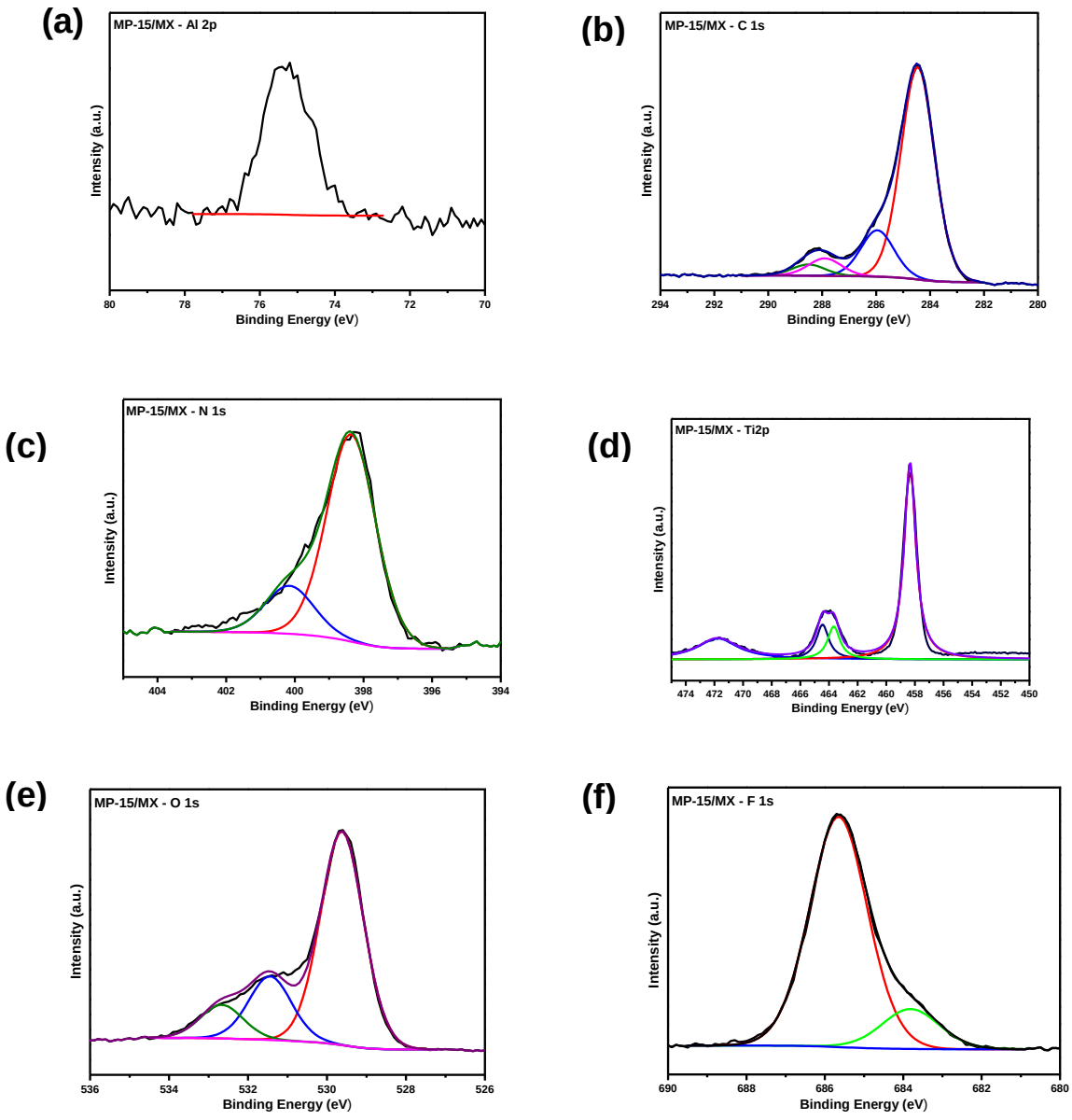

Figure 4.13: XPS high resolution spectra of MP-15/MX (a) Al 2p, (b) C 1s, (c) N 1s, (d) Ti 2p, (e) O 1s, and (f) F 1s

Table 4.8: Peak identification and quantification of MP-15/MX

Name	Peak BE (eV)	FWHM (eV)	Atomic %
Al2p (Organic Al; AlF3)	75.3	1.5	3.3
C1s (C-C)	284.5	1.5	28.5
C1s (C-O)	286.0	1.5	6.2
C1s (C=O)	287.9	1.5	2.3
C1s (O-C=O)	288.5	1.5	1.5
N1s (Organic N)	398.4	1.7	6.2
N1s (Organometallic N)	400.2	1.7	1.4
Ti2p3 (TiO2)	458.3	1.1	8.5
O1s (Metal Oxides)	529.6	1.3	16.1
O1s (Metal Oxides; Organic C-O)	531.3	1.3	4.9
O1s (Organic C=O)	532.7	1.3	2.5
F1s (Fluoride)	683.9	1.8	2.7
F1s (Fluoride)	685.7	1.8	15.6

4.1.5. Microstructural and Morphological Properties

SEM and (HR)TEM were used to, at a micrometre and nanometre level, capture and reveal the morphological and microstructural transformations of the materials as shown in Figures 4.14-17. Complemented with elemental mapping picked up with EDS spectra taken with SEM showing the elemental material evolution corresponding to synthesis steps was observed.

First, the transformation of the parent 3D MAX powders to 2D MXene is explicitly pointed out. The comparison of Figures 4.14 and 4.15 present to us the differences between the as obtained commercial MAX and in-situ HF wet-chemical exfoliated MAX (MXene). Figure 4.14a evidences the characteristic close-packing of Al atoms layered within the bulky MAX which is not transparent under the electron beam as opposed to the as-etched MXene in Figure 4.15a-c. Other differences that standout are the thick multilayers of the MAX as shown in Figure 4.14b relative to the resulting lamellar multi-layered MXene with some narrow slits between the parallel sheets of which some are fragmented around the stacks. This platelet morphology gives us insight of the sheet network on a micrometre level. These observations are consistent with the elemental presence as detected by EDS. The MAX EDS spectra show the presence of Ti, Al, and C, whereas the EDS spectra of MX displays Ti, C, Cl, F, O and a very sharp decrease of Al peak determined to be 4% from the XPS data. The elemental presence of Cl, F, and O reflects the wet-chemical LiF-HCl method that was used to break the inherently strong M-A metallic bond during the etching process, leaving O, Cl, and F as MX surface termination

groups, thus effecting the separation of sheets and partly impeding interplanar forces.

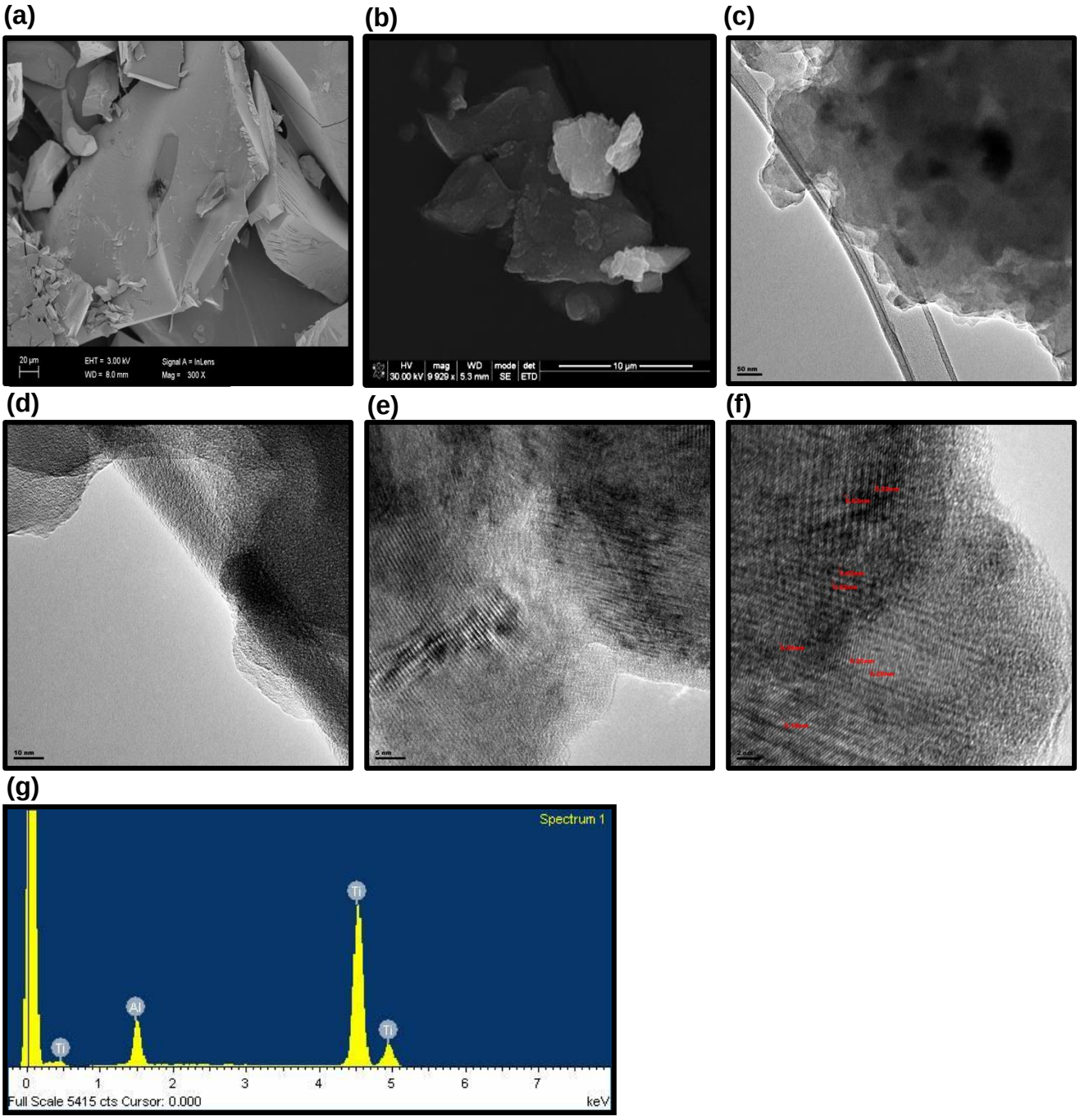

Figure 4.14: SEM (a) 20 µm, (b) 10 µm; TEM & HRTEM (c) 50 nm, (d) 10 nm, (e) 5 nm, (f) 2 nm micrographs, and (g) EDS Spectra of MAX

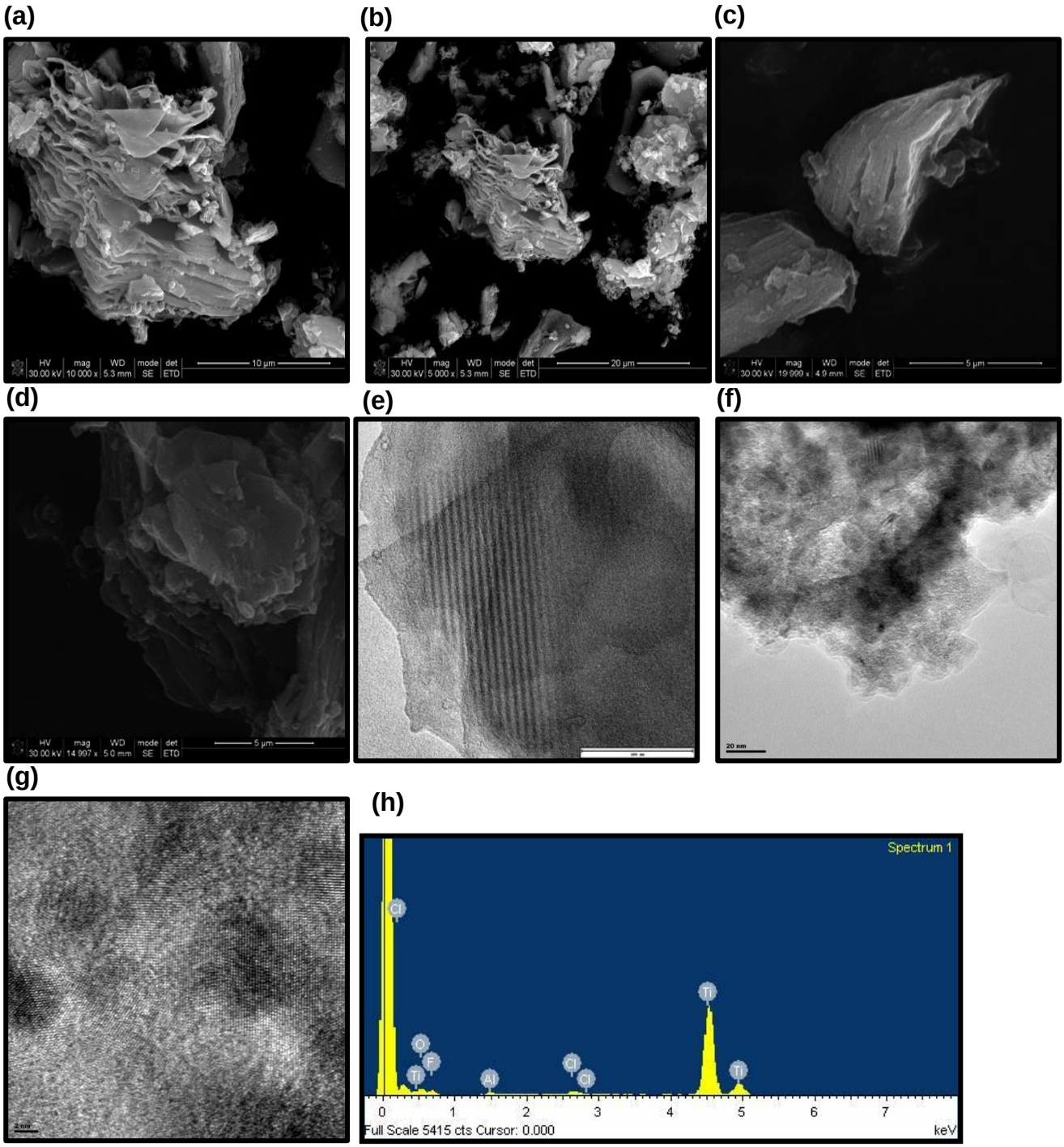

Figure 4.15: SEM (a) 20 µm, (b) 10 µm; (c) 50 nm, (d) 10 nm, TEM & HRTEM (e) 100 nm, (f) 20 nm, (g) 2 nm micrographs, and (h) EDS Spectra of MX

Secondly, the microstructural and morphological effects of the incorporation of nickel(II) tetrapyrazinoporphyrazine into the MX multi-layered, narrow slit network is monitored. Upon a close look into the SEM micrographs of MP-5/MX and MP-15/MX, an introduction of some grains on the MX smooth basal planes, around sheet edges, and their fall off fragments is observed. The introduction of MP between the MX sheets is desirable to increase the interplanar spacing - exposing more surface area or accessible sites on the nanosheet surface - and prevent the nanosheet inclination to restack. These grains seem to be more on the MP-15/MX than on the MP-5/MX. EDS still shows the Ti, C, O and Cl elements with Ni detected the MP-15/MX.

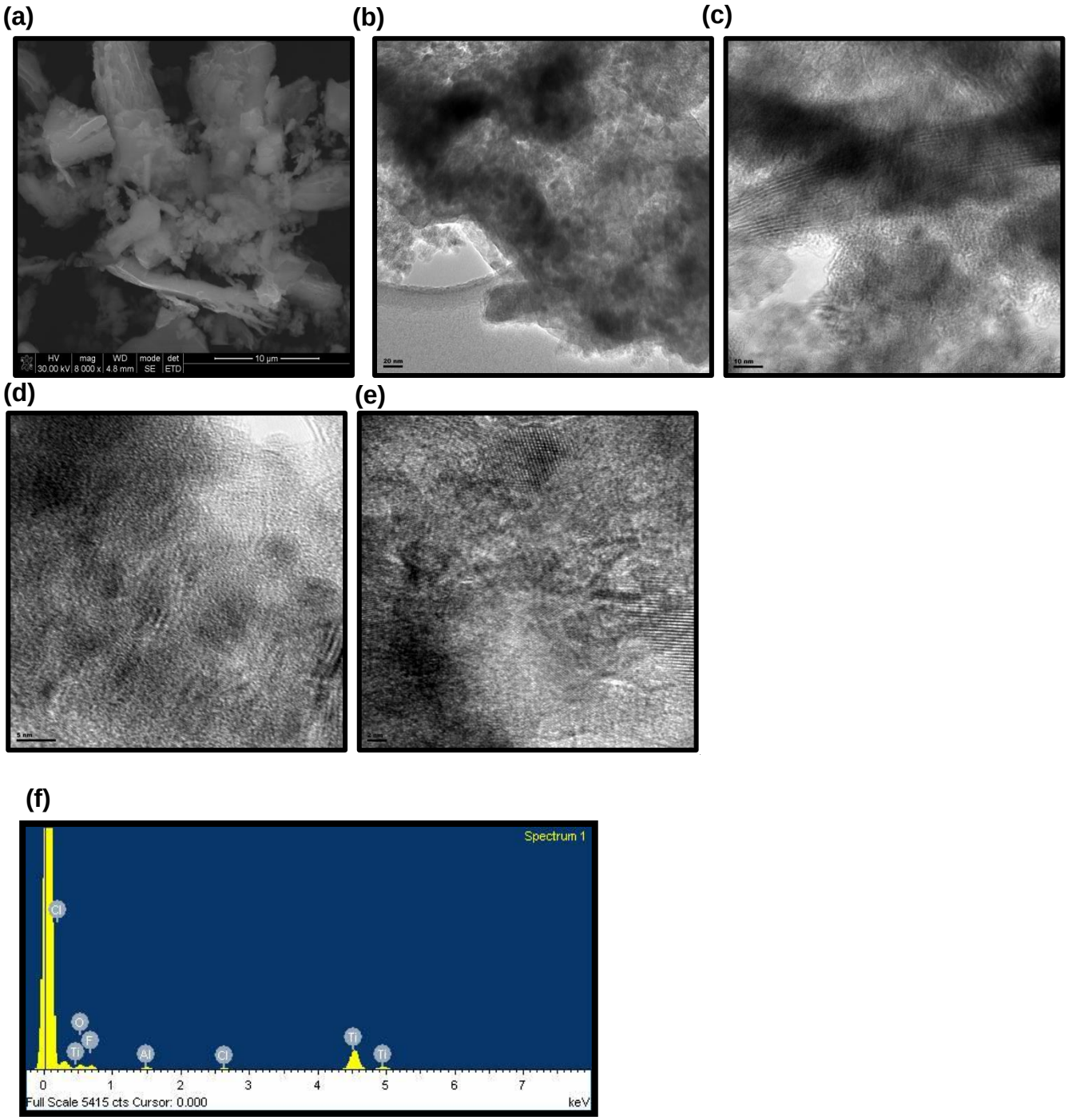

Figure 4.16: SEM (a) 10 µm; TEM & HRTEM (b) 20 nm, (c) 10 nm, (d) 5 nm (e) 2 nm, and (f) EDS Spectra of MP-5/MX

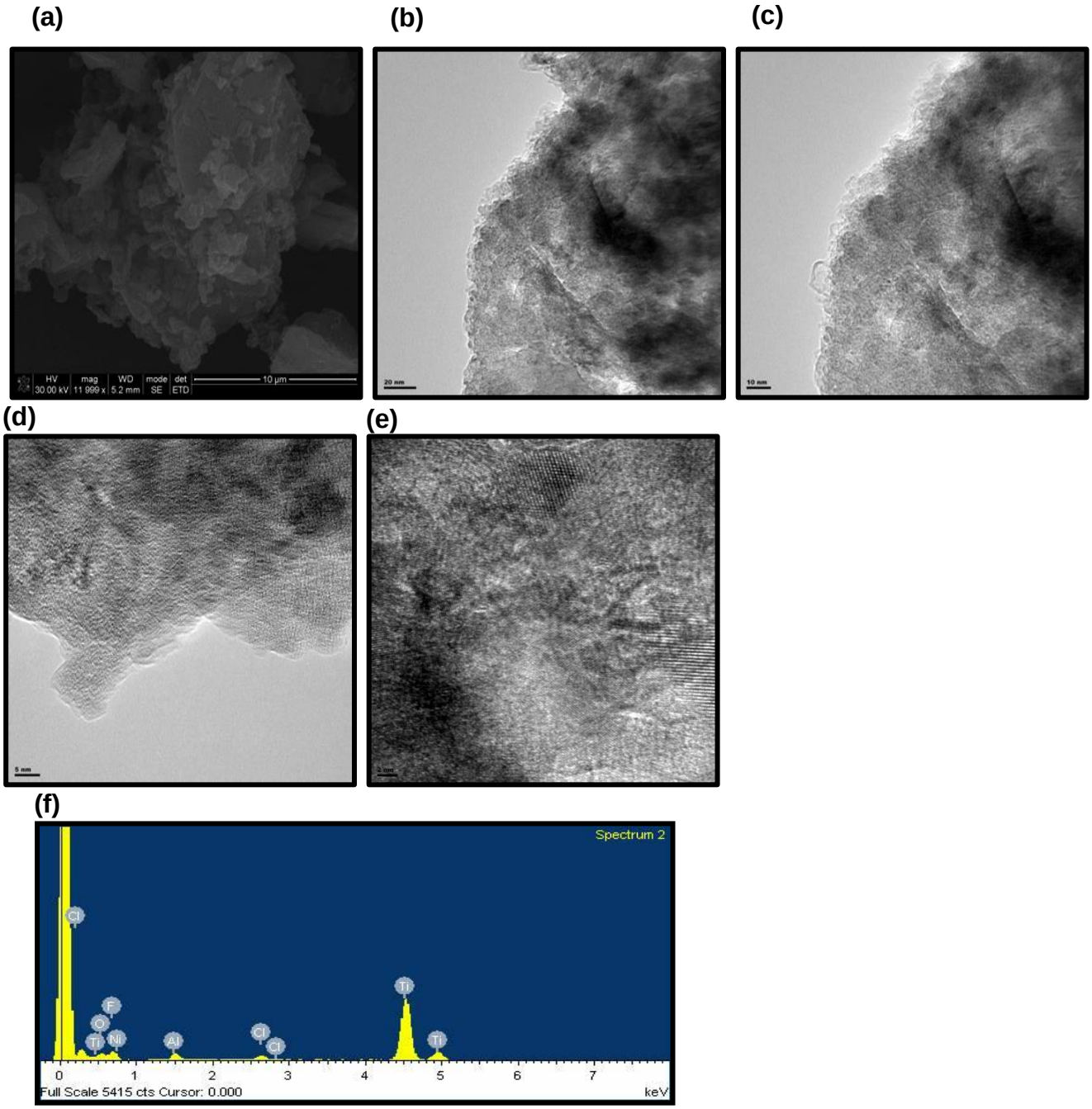

Figure 4.17: SEM (a) 10 µm, TEM & HRTEM (b) 20 nm, (c) 10 nm, (d) 5 nm, (e) 2 nm micrographs and (f) EDS Spectra of MP-15/MX

Table 4.9 provides a qualitative glimpse of the material composition and insights to the present elements in the as-synthesized material. The atomic weight % of carbon was not approximated as carbon tape was used as a substrate for the EDS/SEM analysis.

Table 4.9: Energy dispersive X-ray spectroscopy analysis of MAX, MX, MP-5/MX, and MP-15/MX

Material	**Atomic %**					
	Ti	**O**	**F**	**Cl**	**Ni**	**Al**
MAX	65.6	-	-		-	34.4
MX	18.3	47.8	32.6	0.5	-	0.8
MP-5/MX	19.0	39.8	39.0	1.2		1.0
MP-15/MX	12.1	30.4	54.1	0.8	0.15	2.5

4.2. Physical Properties of Materials

4.2.1. Brunauer-Emmett Teller Surface Area and Porosity Analysis

All BET analyses of materials were undertaken with a single point method. As a result, pore width results are an average of the total pores and the pore volume results are the approximation of the total pores at maximum relative pressure. The primary findings that standout for this physical analysis of the material based on the nitrogen physisorption is the BET surface areas as tabulated on table 4.10. The extraction of Al from Ti_2AlC by selective etching for the generation MX is confirmed by the low surface area value of 11.37 before etching expanding to 44.12 m^2/g after the etching treatment. In addition to that, relative to MX, MP-5/MX and MP-15/MX, there is an inverse relationship between the amount of MP incorporated into the MX microstructure and surface area. Possibly this emanates from the MP complex inhibiting the material pores and agglomerating on the platelet thus clogging the absorptive surface of the MX nanosheets. As tabulated on table 4.10, the absorption average pore with is in

the nanometric scale and well within the 2-50 nm dimensions (2-50 nm being the mesoporous classification of pores according to the International Union of Pure and Applied Chemistry.

Table 4.10: Brunauer-Emmett Teller BET Surface Area, Average Pore Volume, Average Pore Width

Sample	**BET Surface Area (m^2/g)**	**Adsorption Total Pore Volume at max. P/Po (cm^3)**	**Adsorption Average Pore Width (nm)**
MAX	11.37	0.0193	6.791
MX	44.12	0.0578	5.236
MP-5/MX	29.81	0.0510	8.343
MP-15/MX	22.17	0.0463	6.840

4.2.2. Thermogravimetric Analysis

Thermogravimetric analysis was employed to profile the gravimetrical differences by thermally decomposing the synthesized MX, MP-5/MX and MP-15/MX. The obtained curves shown in Figures 4.18 and 4.19 indicate that MX had more residue after 50 to 900°C heating of the material followed by MP-5/MX with 83.57% and MP-15/MX with 74.77% residue. In terms of metallic presence, MX has highest metallic content, followed by MP-5/MX and then MP-15/MX. This trend indicates that as MP is introduced to MX, there is lesser titanium and more organic content form the metallotetrapyrazinoporphyrazine complex. This trend is consistent with BET surface area, spectroscopic, and microscopic results in

indication apparent differences due to the incorporation of the MP complex into the MX multilayers in different amounts.

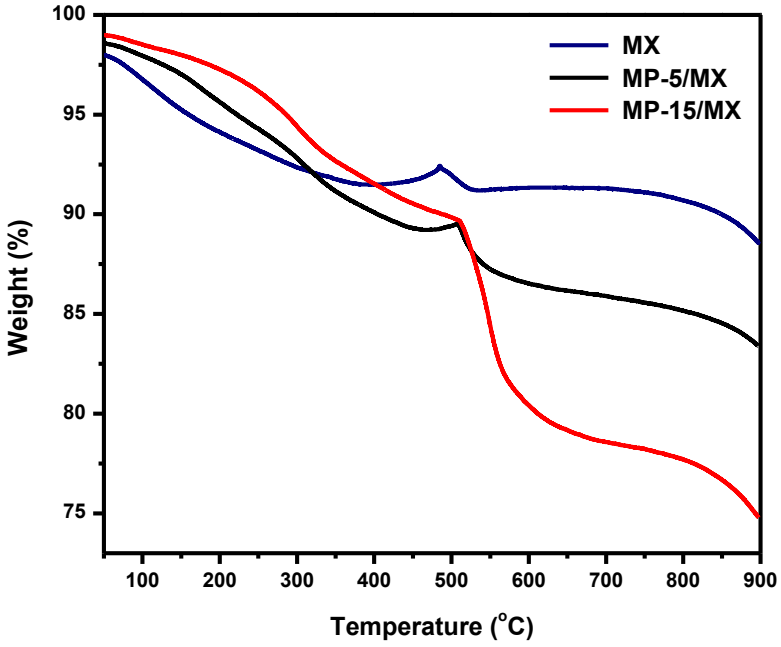

Figure 4.18: Thermogravimetric curves (normalized weight versus temperature) of MX, MP-5/MX, and MP-15/MX

The derivative thermogravimetry Figure 4.19 below shows the major peaks for the MX, MP-5/MX, and MP-15/MX materials. All materials possess two DTG major peaks. The first MX decomposition peak between 90 to 200 ^{o}C is gentle and broad. This peak emanates from the evaporation of water possibly trapped in the MX material from the aqueous synthesis of the material, and the elimination of organic solvents used in the washing and delamination process. The second peak at 500.8 ^{o}C shows can be attributed to the degradation of the MX surface termination groups.

The peaks between 251 and 400 ^{o}C can be attributed to the degradation of amine groups in the tetrapyrazinoporphyrazine structure. The second sharp peaks between

500 to 600 ^{o}C can be associated with the metallo-carbon bond degradation as well as all the charring of the materials as it is sharpest for the MP-15/MX material.

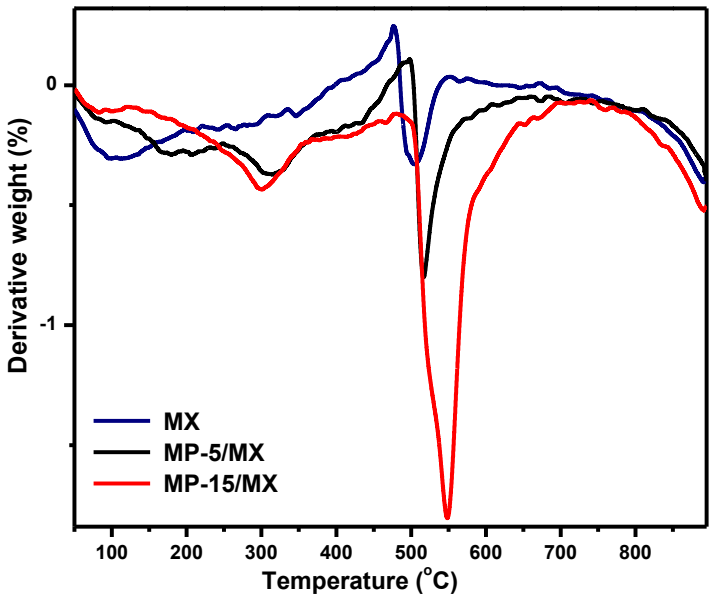

Figure 4.19: Thermogravimetric curves (derivative weight versus temperature) of MX, MP-5/MX, and MP-15/MX

4.3. Reference List

[1] Melchior S.A., Raju, K., Ike, I.S., Erasmus R.M., Kabongo, G., Sigalas, I., Iyuke, S.E., and Ozoemena, K.I. (2018) 'High-Voltage Symmetric Supercapacitor Based on 2D Titanium Carbide (MXene, Ti_2CT_x)/Carbon Nanosphere Composites in a Neutral Aqueous Electrolyte', *Journal of The Electrochemical Society,* 165(3), pp. A501–A511. doi: 10.1149/2.0401803jes.

[2] Rakhi, R. B., Ahmed, B., Hedhili, M. N., Anjum, D.H., and. Alshareef, H. N. (2015). 'Effect of Postetch Annealing Gas Composition on the Structural and Electrochemical Properties of Ti_2CT_x MXene Electrodes for Supercapacitor Applications', *Chemistry of Materials*, 27(15), pp. 5314–5323. doi: 10.1021/acs.chemmater.5b01623.

[3] Wang, P., Mei, B., Hong, X., and Zhou, W. (2007). 'Synthesis of Ti_2AlC by hot pressing and its mechanical and electrical properties', *Transactions of Nonferrous Metals Society of China (English Editio*n), 17(5), pp. 1001–1004. doi: 10.1016/S1003-6326(07)60215-5.

[4] Zhu, K., Jin, Y., Dub, F., Gao, S., Gao, Z., Meng, X. Chen, G., Wei, Y., and Gao, Y. (2019). 'Synthesis of Ti_2CT_x MXene as electrode materials for symmetric supercapacitor with capable volumetric capacitance', *Journal of Energy Chemistry*, 11(2019), pp. 11–18. doi: 10.1016/j.jechem.2018.03.010.

[5] Frodelius, J., Sonestedt, M., Björklund, S., Palmquist, J-P., Stiller, K., Högberg, H., and Hultman, L. (2008). 'Ti_2AlC coatings deposited by High Velocity Oxy-Fuel spraying', *Surface and Coatings Technology*, 202(24), pp. 5976–5981. doi: 10.1016/j.surfcoat.2008.06.184.

[6] Ghidiu, M., Lukatskaya, M.R., Zhao, Q-M., Gogotsi, Y., and Barsoum, M.W. (2014). *'Conductive two-dimensional titanium carbide "clay" with high volumetric capacitance'*, *Nature. Nature Publishing Group*, 516(7529), pp. 78–81. doi: 10.1038/nature13970.

[7] Liu, F., Zhou, A., Chen, J., Jia, J., Zhou, W., Wang, L., and Hua, Q. (2017). 'Preparation of Ti_3C_2 and Ti_2C MXenes by fluoride salts etching and methane adsorptive properties', *Applied Surface Science. Elsevier B.V.*, 416, pp. 781–789. doi: 10.1016/j.apsusc.2017.04.239.

[8] Alhabeb, M., Maleski,K., Anasori, B., Lelyukh, P., Clark, L., Sin, S., and Gogotsi, T. (2017). 'Guidelines for Synthesis and Processing of Two-Dimensional Titanium Carbide ($Ti_3C_2T_x$ MXene)', *Chemistry of Materials*, 29(18), pp. 7633–7644. doi: 10.1021/acs.chemmater.7b02847.

[9] Liu, G., Shen, J., Ji, Y., Liu, Q., Liu, G., Yang, J., and Jin, W. (2019). 'Two-dimensional Ti_2CT_x: MXene membranes with integrated and ordered nanochannels for efficient solvent dehydration', *Journal of Materials Chemistry A*, 7(19), pp. 12095–12104. doi: 10.1039/c9ta01507h.

[10] Anasori, B., Lukatskaya, M. R. and Gogotsi, Y. (2017). '2D metal carbides and nitrides (MXenes) for energy storage'. *Nature Review Materials,* 2 doi: 10.1038/natrevmats.2016.98.

[11] Habib, I., Ferrer, P., Ray, S.C., and Ozoemena, K.I. (2019). 'Interrogating the impact of onion-like carbons on the supercapacitive properties of MXene (Ti_2CT_X)', *Journal of Applied Physics,* 126(13). doi: 10.1063/1.5112107.

[12] Urbankowski, P., Anasori, B., Makaryan, T., Er, D., Kota, S., Walsh, P.L., Zhao, M. Shenoy, V.B, Barsoum, M.W. and Gogotsi, Y. (2016). 'Synthesis of two-

dimensional titanium nitride Ti_4N_3 (MXene)', *Nanoscale. Royal Society of Chemistry*, 8(22), pp. 11385–11391. doi: 10.1039/C6NR02253G.

[13] Lekitima, J.N., Ozoemena, K.I., Jafta, C.J., Kobayashi, K., Song, Y., Tong, D., Chen, S., and Oyama, M. (2013). 'High-performance aqueous asymmetric electrochemical capacitors based on graphene oxide/cobalt(ii)-tetrapyrazinoporphyrazine hybrids', *Journal of Materials Chemistry A*, 1(8), pp. 2821–2826. doi: 10.1039/c2ta01325h

[14] Karweik, D. H. and Winograd, N. (1976). 'Nitrogen Charge Distributions in Free-Base Porphyrins, Metalloporphyrins, and Their Reduced Analogs Observed by X-ray Photoelectron Spectroscopy', *Inorganic Chemistry*, 15(10), pp. 2336–2342. doi: 10.1021/ic50164a003

[15] Guascito, M. R., Ricciardi, G. and Rosa, A. (2017). 'Nickel-macrocycle interaction in nickel(II) porphyrins and porphyrazines bearing alkylthio β-substituents: A combined DFT and XPS study', *Journal of Porphyrins and Phthalocyanines*, 21(4–6), pp. 371–380. doi: 10.1142/S1088424617500328.

[16] Berríos, C., Cárdenas-Jirón, G.I., Marco, J.F., Gutiérrez, C and Ureta-Zañartu, M.S. (2007). 'Theoretical and spectroscopic study of nickel(II) porphyrin derivatives', *Journal of Physical Chemistry A*, 111(14), pp. 2706–2714. doi: 10.1021/jp0653961

[17] Pop, D., Winter, B., Freyer, W., Hertel, I.V., and Widdra, W. (2003). 'Electronic structure of metal-free porphyrazines in thin films', *Journal of Physical Chemistry B*, 107(42), pp. 11643–11647. doi: 10.1021/jp030647g

[18] Svirskiy, G.I., Sergeeva, N. N., Krasnikov, S. A., Vinogradov, N. A., Sergeeva, Y. N., Cafolla, A. A., Preobrajenski, A. B. and Vinogradov, A. S. (2017). 'Electronic structure of nickel porphyrin NiP: Study by X-ray photoelectron and

absorption spectroscopy', *Physics of the Solid State*, 59(2), pp. 368–377. doi: 10.1134/S1063783417020299.

[19] Krasnikov, S.A., Sergeeva, N.N., Brzhezinskaya, M.M., Preobrajenski, A.B., Sergeeva, Y.N., Vinogradov, N.A., Cafolla, A.A., Senge, M.O., and Vinogradov, A.S. (2008) 'An x-ray absorption and photoemission study of the electronic structure of Ni porphyrins and Ni N-confused porphyrin', *Journal of Physics Condensed Matter*, 20(23). doi: 10.1088/0953-8984/20/23/235207

[20] Fang, Y., Yang, X., Chen, T., Xu, G., Liu, M., Liu, J., Xu, and Y. (2018). Two-dimensional titanium carbide (MXene)-based solid-state electrochemiluminescent sensor for label-free single-nucleotide mismatch discrimination in human urine', *Sensors and Actuators, B: Chemical*. Elsevier B.V., 263, pp. 400–407. doi: 10.1016/j.snb.2018.02.102.

[21] Halim, J. Cook, K.M., Naguib, M., Eklund, P., Gogotsi, Y., Rosen, J., and Barsoum, M.W. (2016). 'X-ray photoelectron spectroscopy of select multi-layered transition metal carbides (MXenes)', *Applied Surface Science*, 362, pp. 406–417. doi: 10.1016/j.apsusc.2015.11.089.

[22] Zhang, Z., Lim, S.H., Lai, D.M.Y., Tan, S.Y., Koh, X.Q., Chai, J., and Wang, S. J., Jin, H., and Pan, J.S. (2017). 'Probing the oxidation behavior of Ti_2AlC MAX phase powders between 200 and 1000 °C', Journal of the European Ceramic Society. Elsevier Ltd, 37(1), pp. 43–51. doi: 10.1016/j.jeurceramsoc.2016.08.004.

[23] Halim, J., Persson, I., Moon, E.J., Kühne, P., Darakchieva, V., Persson, P.O.Å., Eklund, P., Rosen, J., and Barsoum, M.W. (2019). 'Electronic and optical characterization of 2D Ti_2C and Nb_2C (MXene) thin films', *Journal of Physics Condensed Matter*, 31(16). doi: 10.1088/1361-648X/ab00a2.

[24] Yamamoto, S., Bluhm, H., Andersson, K., Ketteler, G., Ogasawara, H., Salmeron, M., and Nilsson, A. (2008). 'In situ x-ray photoelectron spectroscopy studies of water on metals and oxides at ambient conditions', *Journal of Physics Condensed Matter*, 20(18). doi: 10.1088/0953-8984/20/18/184025.

[25] Mousty-desbuquoit, C., Riga, J., and Verbist, J. J. (1987). 'Electronic Structure of Titanium(III) and Titanium(IV) Halides Studied by Solid-Phase X-ray Photoelectron Spectroscopy', *Inorganic Chemistry*, 26(8), pp. 1212–1217. doi: 10.1021/ic00255a008.

CHAPTER 5

ELECTROCHEMICAL PERFORMANCE EVALUATION

ACIDIC ELECTROLYTE

The electrochemical charge storage mechanisms of the MX, MP-5/MX, and MP-15/MX were assessed in three, and two electrode configuration systems in acidic electrolyte. This part of study presents the electrochemical evaluation of our materials in 1 M H_2SO_4 based cells. According to the work done on aqueous class of electrolyte for MXene as active electrode materials, sulphuric acid has emerged as the best in terms of highest specific capacitance and redox activity [1].29 This chapter is divided into two sections. Section 5.1 is focused on three electrode cells. Section 5.2 is focused on symmetrical cells where the CV, GCD, and PEIS results are presented and compared.

The pH of the 1 M H_2SO_4 electrolyte was: 0.55.

5.1. Half-Cell Cyclic Voltammetry Studies – Acidic Electrolyte

In 5.1.1. the general three electrode CV analysis will be discussed. In 5.1.2., according to the current (I) and scan rate (v) relationship, the charge storage mechanism kinetics will be studied. In 5.1.3. capacitive contributions will be quantified using total current (I) as a function of potential (V) related to the scan rate dependencies.

5.1.1 General Evaluation – Acidic Electrolyte

Figure 5.1a-c shows the obtained cyclic voltammograms of the three materials: MX, MP-5/MX, and MP-15/MX. These materials in their respective systems were swept at the scan rate range 5 to 200 mV/s at a 0.6 V potential window ranging from – 0.5 to 0.1 V. This voltage window is mostly on the negative potentials because of the MX stability in the negative operating potential range.

Shown in Figure 5.1a is the three-electrode cyclic voltammogram of Ti_2CT_x, herein referred to as MX. This Figure shows the known oxidation behaviour of Ti-O termination groups of the Ti_2CT_x in H_2SO_4 for electrochemical capacitor applications. Many studies focused on $Ti_3C_2T_x$ - which is a first MXene to be synthesized and is a layer heavier than the Ti_2CT_x used in this work - have presented CV curves like the one we present for our pristine Ti_2CT_x. This is not a surprise because both these materials have identical surface functionalities and therefore similar surface redox reactions electrochemistry [2, 3].

The shape of the CV curve for MX in H_2SO_4 is near-rectangular and is typical of the MX redox activity in H_2SO_4. This near-rectangular shaped CV loop qualitatively suggests the pseudocapacitive nature of the pristine material in low pH electrolyte. A more reliable quantitative method for classifying the extent of active charge storage mechanisms will be used to interpret the CV obtained data in sections 5.1.2 and 5.1.3. Also, it is known according to published literature that electrochemical capacitor systems whose components are comprised of sulphuric

acid electrolyte and titanium oxide based or surfaced electrode materials have relatively higher pseudocapacitance than in neutral or basic aqueous media [1-4]. The reason for this highly appreciated pseudocapacitance stems from the faradaic charge transfer process which is attributed to the hydronium ions from the electrolyte accumulating on the material surface Ti-O oxygen termination groups upon charging (reduction to lower oxidation states) and the subsequent reversal (oxidation to higher oxidation states) upon discharge. This redox activity happens as a function of potential change that transitions the oxidation state of Ti upon charge and discharge by de/intercalation or desorption/adsorption of cations at or near the electrode surface [5]. Therefore, gentle broad redox couples on Figure 5a indicate the reversible change of Ti – oxidation states between +3 and +4. Equation 5.1 is a commonly assumed equation to express the involved reaction corresponding to Figure 5a as they are labelled on the Figure [2]. The minor cathodic peak visible between cathodic peak 1 and two from scan rates 75 to 200 mV/s can be related to irreversible parasitic reaction evolving the material to TiO_2.

$$Ti_2CO_x(OH)_yF_{x-y} + \delta\bar{e} + \delta H^+ \rightleftharpoons Ti_2CO_{x-\delta}(OH)_{y+\delta}F_{x-y} \qquad (5.1)$$

The charge storage mechanism enhancement as a result of nickel(II) tetrapyrazinoporphyrazine incorporation with the layered material network of MX were subsequently examined under the CV parameters as the MX CV testing.

On Figures 5.1b and 5.1c, their cyclic voltammograms show pronounced reduction peaks between potential – 0.38 V and - 0.25 V. These pronounced redox peaks in MP/MX active materials are attributed to faster, and high energy protonation and deprotonation. Hypothetically, these empirical observations may be due to the

electrocatalysis role of the π-rich bonds of the macrocyclic compound. A second postulation is: as hydronium species are aggregated on the pi-conjugated nucleophilic MP dopant and the linear change electrical potential is applied between the working and reference electrode, the kinetics are enhanced to improve the charge storage properties of the system. As potential is applied, the MP species intensify the rapidity of cation mobility through the pathways because of its role as an interplanar spacer, and thus allowing more cation diffusion and pseudocapacitive intercalation on the oxygenated titanium surface functionalities. These processes are quantitatively corroborated by the peak data extracted from the respective CV curves to tabulate the power law dependence graphs as well as in capacitive studies.

Also, important to note, Figure 5b shows this pronounced peak at ≈ - 0.38 V at the minimum scan rate, this oxidation peak has a right-ward shift as the scan rate is increased. This shift can be indicative of the non-reversibility this reaction might have [6] which is not desired. Moreover, pronounced peaks are more intense for MP-15/MX than they are for MP-5/MX. However, the more intense the current response as a result of increased MP content in MX the smaller the integration area towards the positive voltage end. The implication is that there is a lower open circuit potential volume as MP is increased. The MP/MX active material may be more suited for asymmetrical pseudocapacitors as good negative electrode materials. Figure 5.1d gives an indication of the specific gravimetric capacitance performance of all three materials at specific scan rates. The supercapacitive performance of MP-15/MX is the highest at lowest scan rate, followed by MP-5/MX performance and the pristine MX. The specific gravimetric capacitance values at

the lowest scan rate, 5 mV/s are 89.2, 59.7, and 54.5 F/g for MX, MP-5/MX and MP-15/MX respectively. However, at the highest scan rate of 200 mV/s MX exhibits the highest capacitance of 31.8 F/g while MP-5/MX and MP-15/MX have relatively lower capacitances, 16.9 and 26.9 F/g respectively. This is indicative of the possible MP inhibited protonic transport paths within the interlamellar network such that the pristine material is more active at high scan rates to store and release charge.

The observation is MP influences the capacitance of the material, but the half-cell tests were primarily used to gain insight on the material behaviour and electrochemistry kinetics than energy performance. The symmetrical cell results will be focussed on the device energy performance.

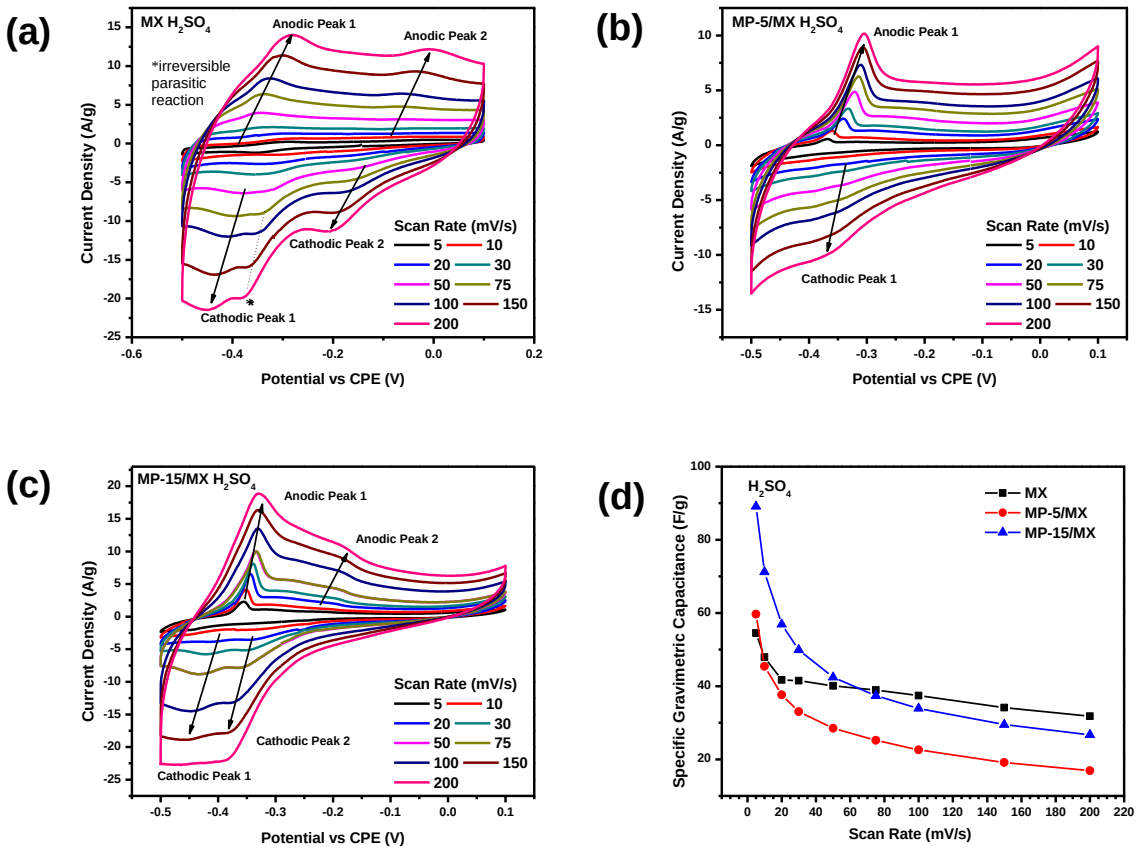

Figure 5.1: Cyclic voltammograms of (a) MX, (b) MP-5/MX, and (c) MP-15/MX in 1 M H_2SO_4 electrolyte, and (d) the specific gravimetric capacitance comparison calculated from CV at different scan rates

5.1.2. Mechanism Studies: Charge Storage Kinetics – Acidic Electrolyte

According to the power law relationship between the current response and sweep rate at fixed potentials as mentioned on chapter 3, the kinetics of electrochemical reactions can be calculated from CV curves of the materials. Current responses of peaks at specific voltages and scan rates were recorded and linearly fitted as presented on Figures 5.2a,c,e to evaluate the linear dependence and then the corresponding logarithmic translation of the plots was established as showed on Figures 5.2b,d,f to solve b. The b-value is indicative

of the charge storage mechanism exhibited by materials in acidic electrolyte in this instance. MX showed interesting results as 4 distinct peaks are observable on Figure 5.1a. The b-values, although they all vary, the first step is relatively close to 1 than all the others. However, all b-values are in the transitional range (between 0.5 and 1). This suggests a capacitive mechanism in place for the pristine material which makes this a complex reaction to decode without in-situ spectroscopic techniques to monitor the lattice parameters and oxidation states as reactions take place. However, from published work, it has been observed that the carbide nanosheets can be from the -OH terminated surfaces [6]. Hydroxyl surface terminations induce capacitive energy storage in titanium carbide MXenes. So, the conclusion that can be drawn from this is that the MX in this work has a higher distribution of -OH terminated surface chemistry. Figures 5d, and 5f show the decrease towards 0.5 b-value. This decrease represents the changes induced by the MP intercalant. It is quite clear that the mechanism in MP-5/MX as presented on Figure 5d is simpler than the complexity observed in Figure 5f. b-values decreasing as a result of the introduction of MP to MX, specifically for MP-5/MX, prove that the presence of MP has a redox effect on the charge storage mechanism of MX. The multiplicity makes it difficult to understand the electrochemistry as some peaks might be overshadowed by prominent ones. However, the shift of onset peak potentials is indicative of an electrochemical irreversibility of MP-15/MX material which might negatively affect the overall cell performance.

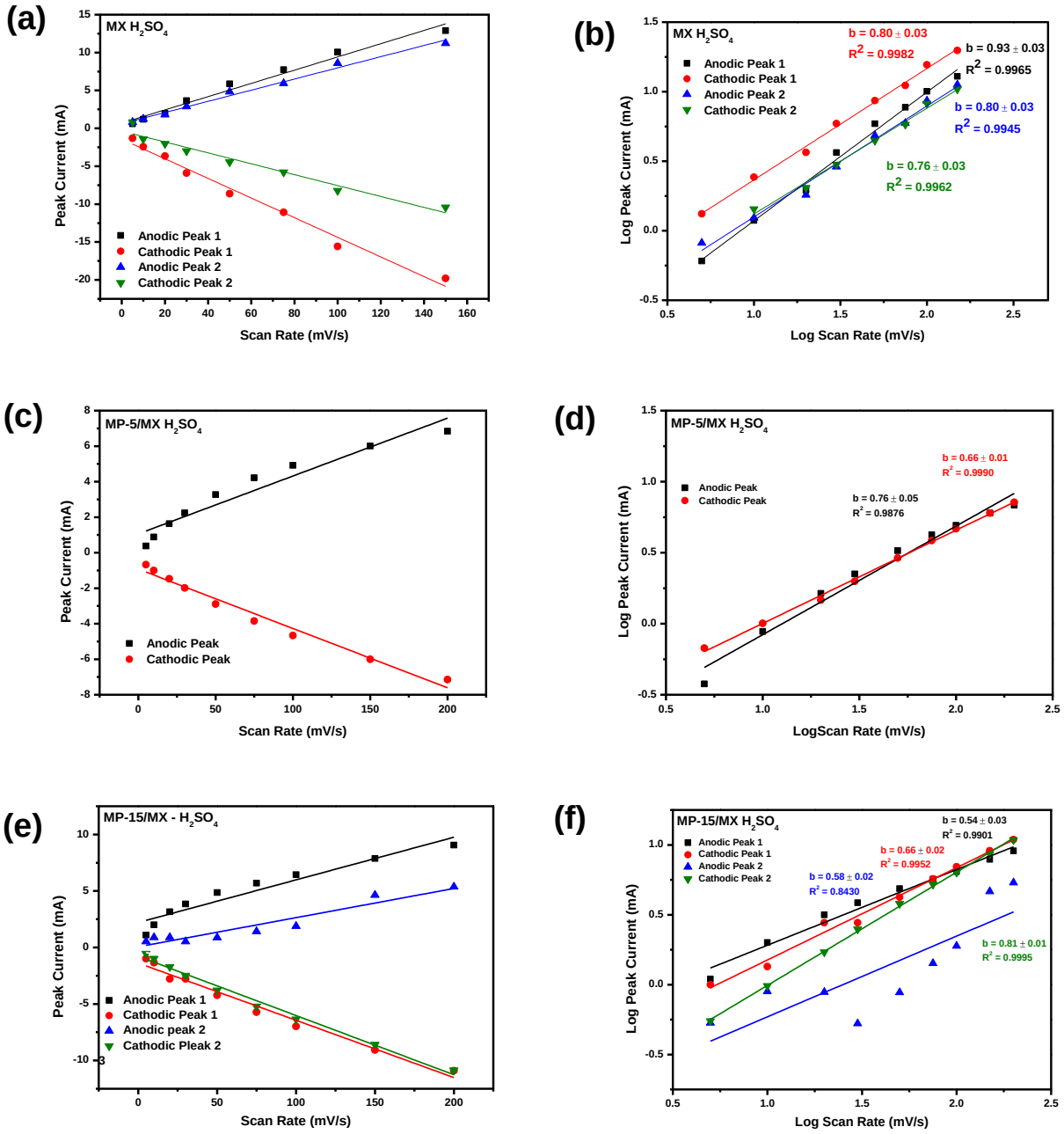

Figure 5.2: Linear power dependence plots, current (i) vs scan rate (v); log current (i) vs log scan rate (v) of: (a;b) MX, (c;d) MP-5/MX, and (e;f) MP-15/MX in 1 M H_2SO_4 electrolyte

5.1.3. Mechanism Studies: Capacitive Contributions – Acidic Electrolyte

As mentioned earlier, the capacitance of MX nanosheets is higher in sulphuric acid. Given the relatively lower specific surface area of the materials compared to high surface area carbon materials, if the EDLC was the only mechanism at play, the capacitance of MX would be extremely lower than that of carbon-based systems but that is not the case. This means pseudocapacitive charge storage mechanisms are also present. Tests to approximate the capacitive contribution of EDL and PC were undertaken in three electrode cells with a CPE quasi-reference electrode. The resulting CV evolutions are presented on Figure 5.1 (a – c). Figure 5.3a,c,e presents the calculated contributions at 20 mV/s for all the materials. Figure 5.3b,d,f depict the contributions in percentages. MX has 71% capacitive contribution and 29% diffusion-controlled contribution. The diffusion-controlled contribution increased from 29% for MX to 50.2% on Figure 5.3d as a result of MP. This increase can be attributed to two pseudocapacitive mechanisms: (i) redox pseudocapacitance and (ii) intercalation pseudocapacitance. Redox activity is improved because of the participation of MP in the redox activity. Intercalation pseudocapacitance is improved because of the presence of MP as an interplanar spacer allowing for more protic adsorption on/near the surface of MX. Figure 5.3f shows an increase in capacitive contribution as MP is further increased and a decrease in diffusion-controlled contribution of 24% for MP-15/MX material. This can be a result of the MP species clogging the MX surfaces thus making it difficult for hydronium ions to have a free path and interact with the active sites of the host MX.

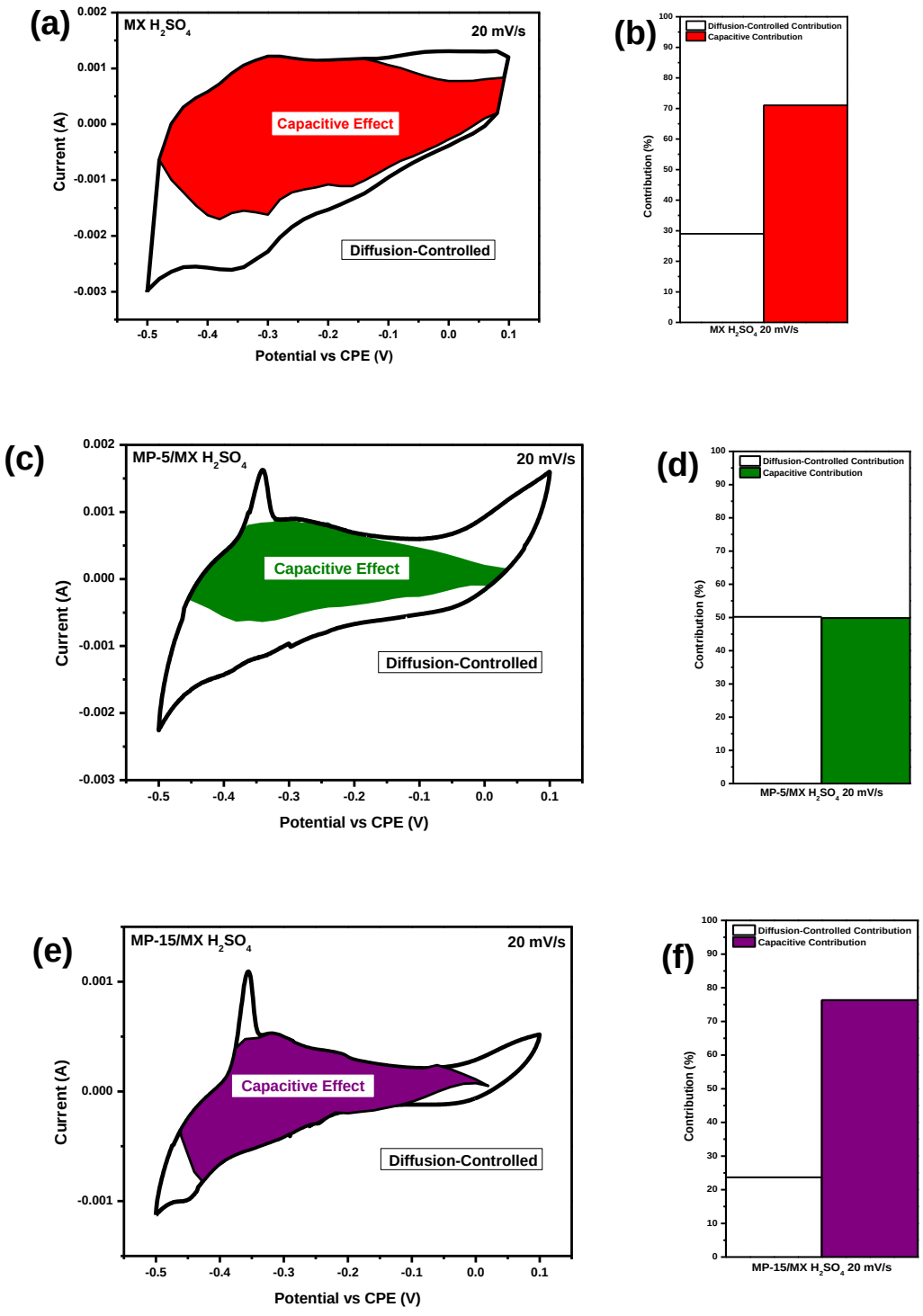

Figure 5.3: Diffusion-controlled and capacitive contribution determination cyclic voltammogram at 20 mV/s of (a) MX, (c) MP-5/MX, and (e) MP-15/MX at 20 mV/s for contribution studies; and corresponding bar graphs showing the contribution of different processes at 20 mV/s scan rate for (b) MX, (d) MP-5/MX, and (f) MP-15/MX in 1 M H_2SO_4 electrolyte

5.2. Symmetrical Cells – Acidic Electrolyte

All the full cell electrochemical performance evaluation tests were performed under common parameters with Swagelok two electrode split cell housing the symmetrical electrodes seperated by a glass fiber separator soaked in 1 M H_2SO_4 electrolyte as described in the methodolgy section with MX, MP-5/MX and MP-15/MX as active electrode materials. Testing parameters for CV evolutions presented on Figure 5.4a,c,e were 3, 5, 10, 20, 30, 50, 75 and 100 mVs^{-1} scan rates providing the following gravimetric specific capacitances: (MX) 33.9, 25.6, 18.5, 12.3, 11.1, 9.0, 7.7, and 7.0 F/g; (MP-5/MX) 51.4, 39.9, 31.2, 25.6, 23.2, 20.7, 19.0, and 18.0 F/g, (MP-15/MX) 109.5, 77.4, 53.7, 40..4, 36.6, 31.9, 29.2, and 27.1 F/g. On the other hand, there were minor variations on the GCD parameters because of respective cell performance difference. The pristine material-based cell could charge at low current density of 0.10 A/g, while the modified material required moderately higher current densitites, 0.15 A/g for MP-5/MX and 0.25 A/g for MP-15/MX. Based on Figures 5.4b,d,f the best coloumbic efficiency is 96.5% at 1 A/g current density for MX, the worst is for MP-15/MX which is 60.1% at 0.25 A/g. These differences in response confirm the resistitivity MP induces at high dosages to the supercapacitive performance of MX and the desired performance enhancement MP provides in lower quantities as the MP-5/MX coulumbic efficiency is better compared to MP-15/MX.

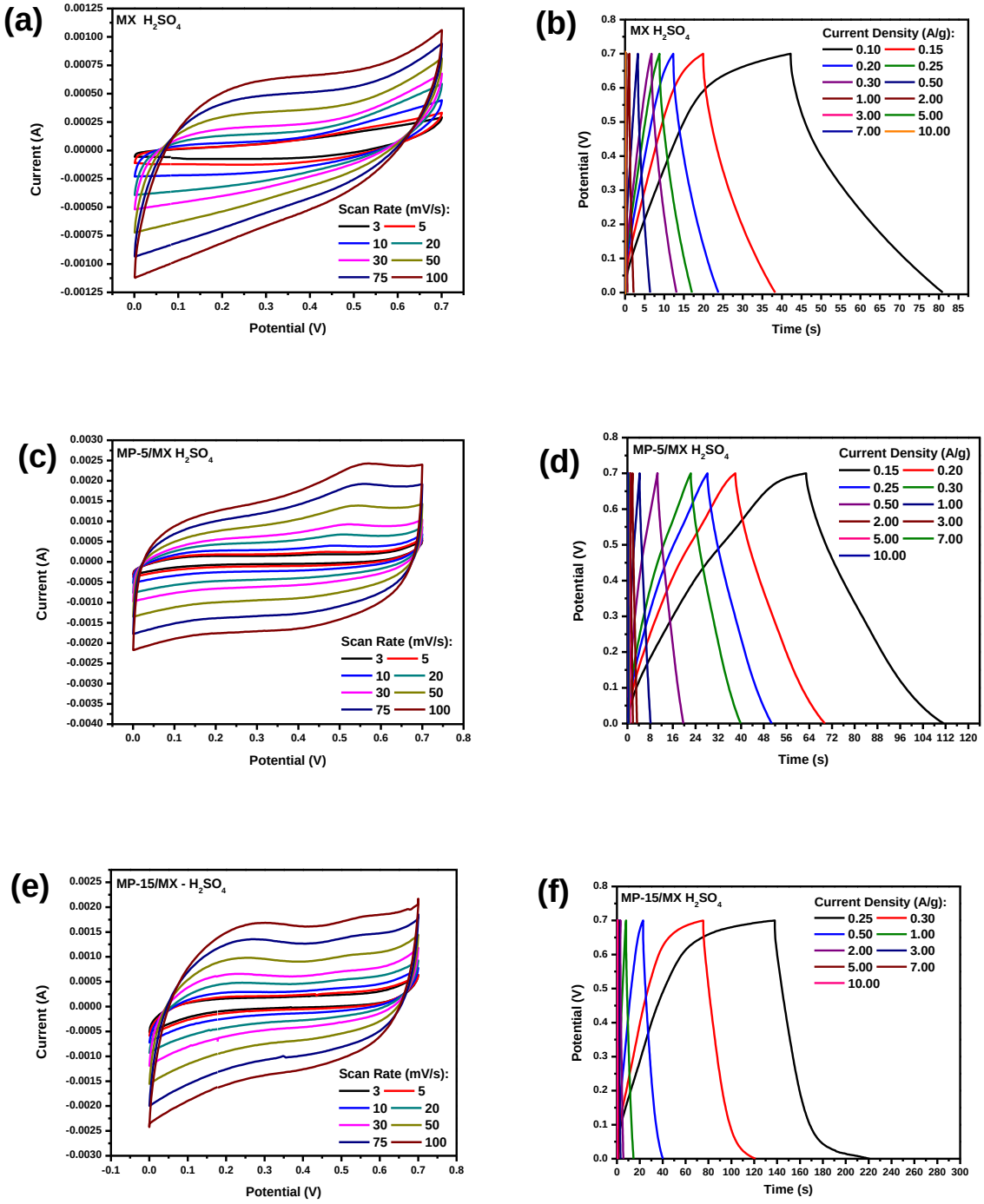

Figure 5.4: Two-electrode cyclic voltammograms of (a) MX, (c) MP-5/MX, and (e) MP-15/MX; and galvanostatic charge discharge profiles of (b) MX, (d) MP-5/MX, and (f) MP-15/MX in 1 M H_2SO_4 electrolyte

MP-5/MX is better in shape possibly because of the extra reaction in H_2SO_4 such as hydrogen evolution reaction but in symmetric cell, hydrogen evolution reaction is prevented and the full cell performance in terms of energy density, power density and long term cycling stability is observed.

On Figure 5.5a-d it is evident that MP-15/MX shows the highest capacitance. Second to that is MP-5/MX material and lastly, the prisitine MX is the worst performing in terms of capacitance. So the addition of MP to MX improves the energy density. However, although this is an improvement, the Ragone plot on Figure 5.5e reveals that the addition of MP improves the capacitance and energy density but limits the power of cell performance. An insight for this limitation is elucidated from two perspectives. Firstly, from the physical characterization perspective, the surface area of the layered material decreases as the modifying material is introduced to the host material. Based on the CV loops and GCD curves on Figures 5.4a-f, MX show internal cell resistance at 0.6 V, MP-5/MX has a gentle redox peak at 0.58 V that effectively fades out the resitence and MP-15/MX shows the most resistence yet highest capacitance. So, deducing from the apparent trend for symmetrical cells, the presence of MP in relatively low quantities effects redox activity and enables optimal ion transport paths such that resistence is low. As the MP is increased, theres more resistence but the energy density improves as well.

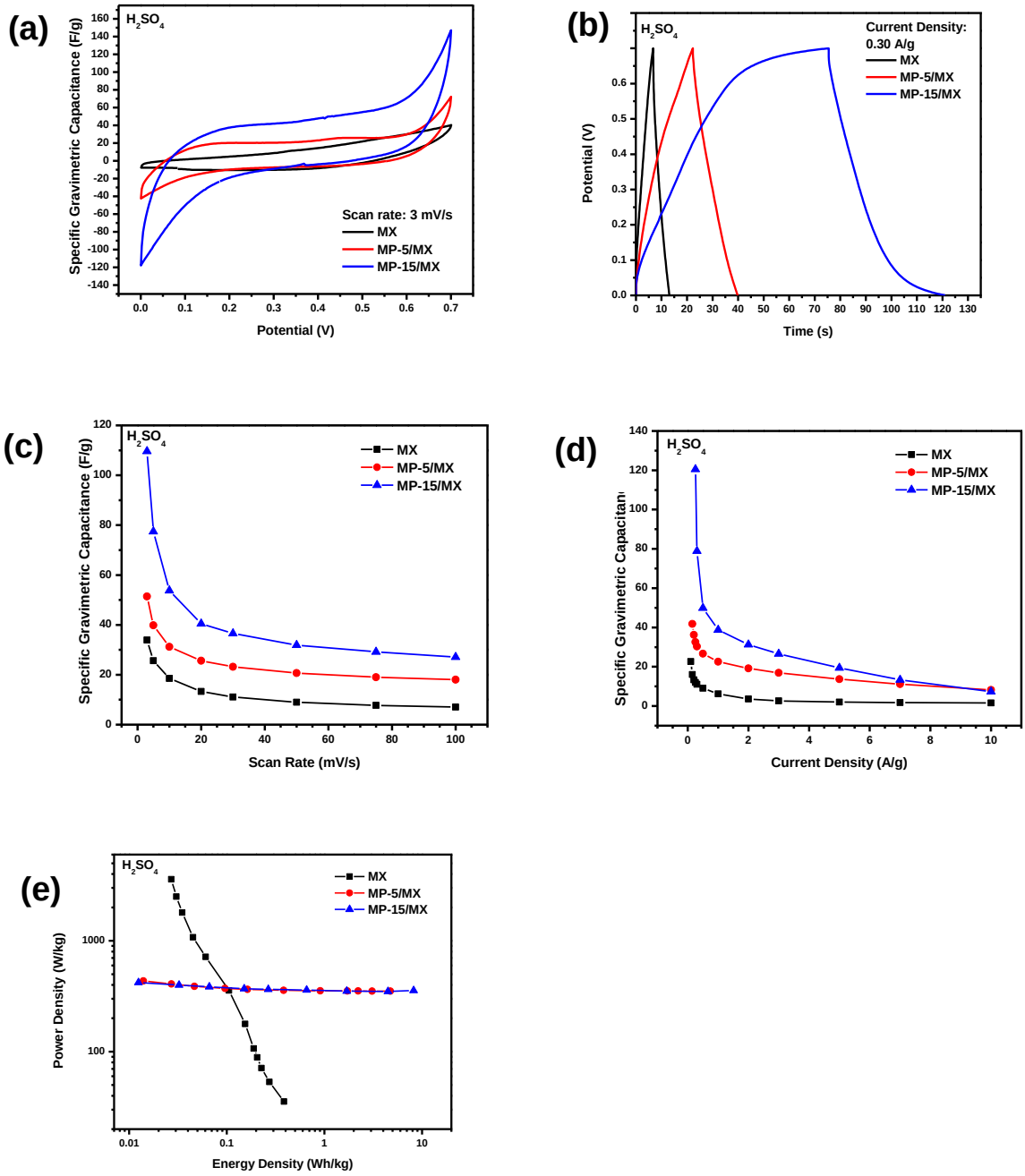

Figure 5.5: (a) Cyclic voltammogram specific gravimetric capacitance comparison of MX, MP-5/MX, and MP-15/MX at 3 mV/s; (b) Constant current charge/discharge profile comparison of MX, MP-5/MX, and MP-15/MX at 0.30 A/g; (c) Specific gravimetric capacitance comparison of MX, MP-5/MX, and MP-15/MX calculated from cyclic voltammogram areas at sweep rate range 3 to 100 mV/s; (d) Specific gravimetric capacitance comparison of MX, MP-5/MX, and MP-15/MX calculated from discharge time at constant current range 0.30 to 10.00 A/g; and (e) the Ragone plot of MX, MP-5/MX, and MP-15/MX in H_2SO_4 system

The lifetime stability of these novel materials was studied via constant current charge/discharge long term cycling for a minimum of 5000 cycles at a 1.0 A/g current density. MX reached 5000 cycles with a decrease in columbic efficiency to 91.7% and a capacitance retention drop to 98.6% at the 4755th cycle as presented on Figure 5.6a. So, MX has impressive electrochemical stability. MP-5/MX on Figure 5.6b is not as stable as MX but it is more stable than MP-15/MX. The initial capacitance retention for MP-5/MX is 100% and runs out to 80.5% after 4000 cycles with the columbic efficiency 96.0% while MP-15/MX has an initial capacitance retention 100 that drops to 44.9% at the 5000th cycle and shows a relatively low columbic efficiency retention that starts at 96.3% at the first cycle to 82.5% on the 5000th cycle.

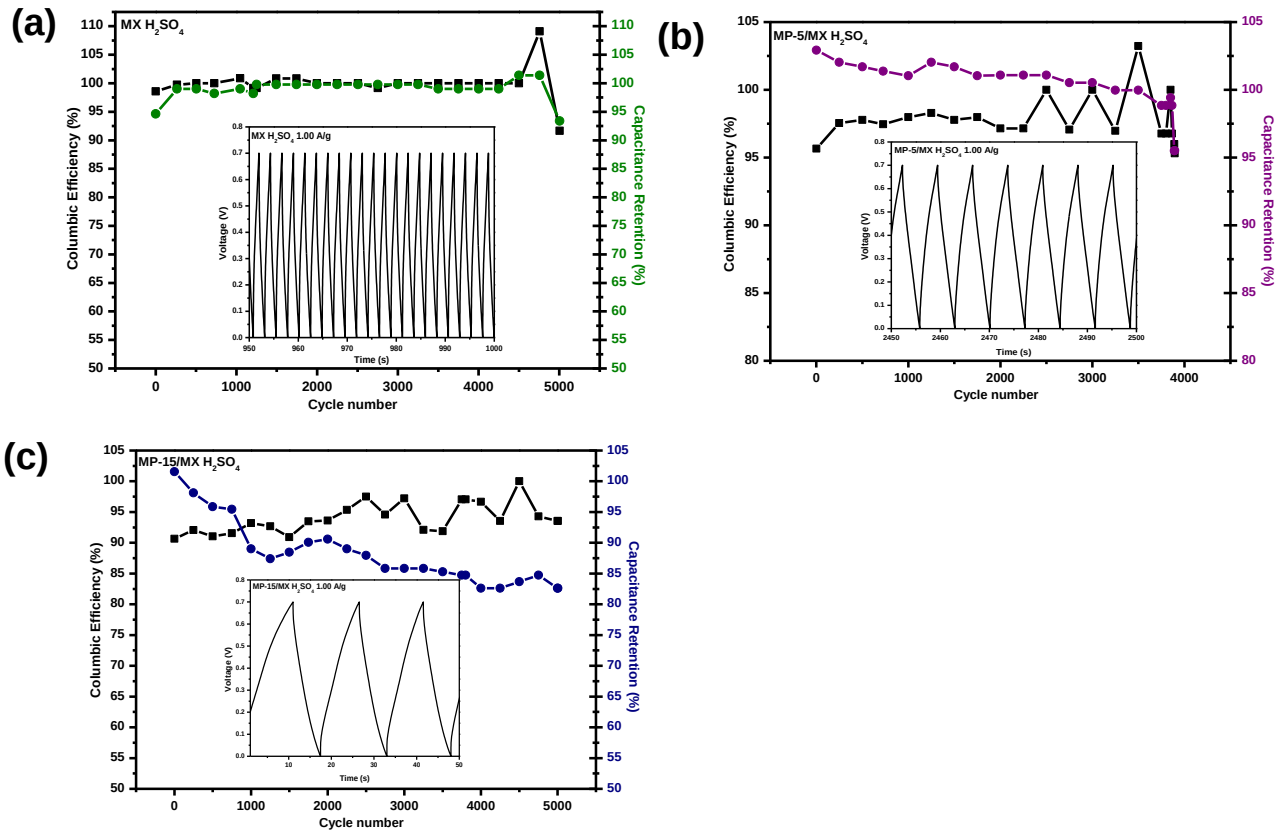

Figure 5.6: Long term cycling tests of(a) MX, (b) MP-5/MX, and (c) MP-15/MX

EIS was used to investigate the full cell impedance properties after an approximately 4 hours equilibration time prior to any cyclic voltammetry and charge/discharge characterization tests. After the initial EIS investigation, CV tests to establish an optimal operating voltage window were swept at a 20 mVs-1 rate - this step also served as a cell activation step. These voltage window studies were performed with caution starting from 0.1 V to 0.7 V which was found to be the widest potential range of the system without inducing any electrolyte degradation. The potentio-electrochemical impedance spectroscopy testing parameters were set to 3 mV to open circuit potential in the frequency range of 200 kHz to 10 mHz at room temperature.

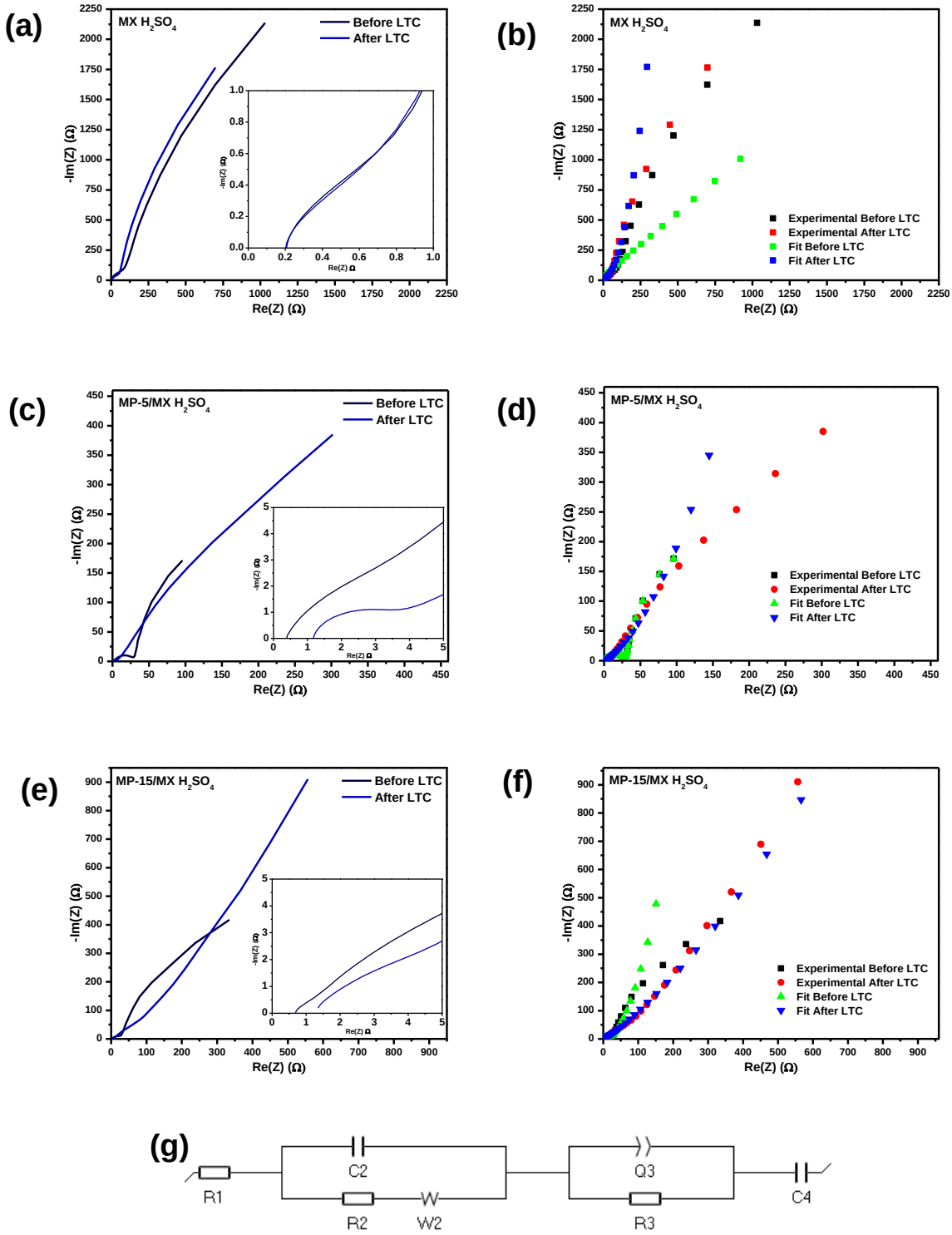

Figure 5.7: The Nyquist spectra of (a) MX, (b) MX fit, (c) MP-5/MX, (d) MP-5/MX fit, (e) MP-15/MX, (f) MP-15/MX fit, and (g) the equivalent electric circuit used for the fitting of the 1 M H_2SO_4 electrolyte based symmetrical devices EIS data for before and after the stability tests to observe the changes in material impedence characteristics

In Figure 5.7a, a Nyquist spectra representation of pristine MX based electrode in H_2SO_4 electrolyte tested in a symmetrical electrode configuration is presented. The two curves shown on this plot are for before and after long term cycling to monitor the transformations in the impedance characteristics. On this Figure, the real impedance axis (x-axis) of the plot is intercepted by the MX curves at 0.2076 Ω and 0.2019 Ω for pre and post long-term cycling test, respectively. The low ohmic resistances of both tests are indicative of good electrolyte-electrode material resistance as well as good electrode material-current collector contact resistance. The minor change in resistance and overall curves validates the long-term cycling finding regarding MX as having an impressive electrochemical stability in 1 M H_2SO_4 electrolyte notwithstanding the possibility of diminishing electrical conductivity of MX material and electrolyte degradation over prolonged cycling. Furthermore, a magnified assessment of the MX high frequency region of the impedance response as shown on Figure 5.7a inset, distinctively shows the absence of a semi-circle. This absence of the semi-circle in pristine MX is indicative of low faradaic electrolyte-electrolyte resistance in MX surfaces as well as the low contact resistance between the electrode material and the substrate. So, the absence of the semi-circle implies good conductivity. After cycling, the Nyquist spectra minor alteration suggests of the possibility of a broad semi-circle formation should the cycles be extended. This formation of a semi-circle is followed by a slope on the transitional region reflecting the diffusion of charged ion in the electrode materials as well as capacitance properties.

In the low frequency region, the comparison of EIS response of MX before and after stability tests shows that after cycling, the capacitive behaviour of MX is lesser than before cycling as the spike becomes more parallel to the imaginary axis (y-axis). To

quantitatively interpret the EIS plots, an equivalent circuit was constructed for the computation of charge storage elements and their respective physical meaning. The elements of the equivalent electric circuit selected for modelling the experimental data are R1+C2/(R2+W2)+Q3/R3+C4 where: R1 is the ESR, C2(R2+W3) involves the contact resistance as well as the Warburg diffusion impedance, pseudocapacitive properties and unaccounted possible parasitic or degradation resistance; element; Q3/R3 , constant phase element parallel to R3; as well as C4 representing intercalation capacitance. Figure 5.7g is the circuit representation of the used fit. Table 5.1 presents of EIS fitting data for MX, MP-5/MX, and MP-15/MX in H_2SO_4 electrolyte - symmetrical cell electrochemical performance (amplitude 3 mV, frequency) – before and after long term cycling as extraopolated from Nyquist plots.

Table 5.1: EIS fitting data for MX, MP-5/MX, and MP-15/MX in H_2SO_4 electrolyte - symmetrical cell electrochemical performance (amplitude 3 mV, frequency) – before and after long term cycling as extraopolated from Nyquist plots.

	MX		**MP-5/MX**		**MP-15/MX**	
Parameters	**Before Cycling**	**After Cycling**	**Before Cycling**	**After Cycling**	**Before Cycling**	**After Cycling**
R1 (Ohm)	0.1941 ± 0.4328	0.1979 ± 0.4467	0.3718 ± 0.4317	1.199 ± 0.2314	0.6309 ± 0.6502	1.388 ± 0.451
C2 (F)	0.4352e-3 ± 0.01224	0.8053e-3 ± 0.173e-3	0.6585 e-3 ± 0.4546 e-3	11.05 e-6 ± 0.1332e-3	0.6204 e-3 ± 0.4151 e-3	6.124 e-6 ± 6.911 e-6
R2 (Ohm)	0.2072 ± 1442	24.7 ± 0.9109	18.78 ± 6.796	1.032 ± 38.8	8.729 ± 12.66	1.806 ± 2.996
s2 (Ohm.s $^{-1/2}$)	242.9 ± 1.338	69.25 ± 1.134	9.326 ± 0.7097	43.12 ± 0.2279	33.16 ± 1.2	138.8 ± 1.425
Q3 (F.s $^{a-1}$)	0.3595e-3 ± 0.0171	1.271 e-3 ± 0.02706	0.5914 e-3 ± 0.9877	92.32 e-6 ± 2.25 e-3	2.843 e-3 ± 0.01256	8.569 e-3 ± 9.927 e-3
**C3 (F)*	0.1481e-3	1.168	0.1107 e-3	56 e-6	0.1548 e-3	1.023 e-3
n3	0.904 ± 1	0.7814 ± 1	0.7752 ± 0.9877	0.9481 ± 1	0.5547 ± 0.8829	0.5455 ± 0.8304
R3 (Ohm)	0.6557 ± 3.673	1.168 ± 2.676	5.228 ± 7.794	1.171 ± 38.89	9.369 ± 14.6	9.103 ± 4.868
C4 (F)	0.3898 ± 0.049843	0.01065 ± 34.34 e-6	0.105 ± 2.805 e-3	0.05294 ± 0.5168 e-3	0.04581 ± 0.6902 e-3	0.05433 ± 1.055 e-3
Chi ^{2}	0.7581	0.8822	0.308	0.3852	0.4271	0.08247

The phase angle Bode representation of the impedance analysis presented on Figure 5.8 are useful for the evaluation of capacitance and pseudocapacitance. An interesting feature observable on the four respective bode spectra Figure 5.8a-c showing the performance of respective materials before and after long term cycling tests and Figure 5.8d showing the comparison of all materials before cycling. These plots provide a qualitative analysis in terms of the electrochemical mechanisms involved in the energy storage processes and can be related to the diffusion-controlled and capacitive contribution in the three-electrode section regarding the capacitive and pseudocapacitive nature of the MX, MP-5/MX, and MP-15/MX in H_2SO_4 electrolyte. Observing the bode plot Figure 5.8a, the MX spectra for both before and after long term cycling shows the preservation of the phase angle-frequency signature. This repeatable spectra after long term cycling indicates the good stability of the MX electrodes in 1 M H_2SO_4 media after 5000 cycles. Figure 5.8b has one broad peak indicative of relatively low redox activity. However, the overlay of this spectra before and after cycling shows some differences at low log frequencies implying a change that can be attributed to irreversible redox processes over long cycling. Figure 5.8c has the most activity in terms of peak variations. This implies that MP-15/MX is highly pseudocapacitive but relatively electrochemically unstable compared to its MX, and MP-15 counterparts. A comparative look at the three materials is presented on Figure 5.8d shows the differences in faradaic activity in the systems. The bode spectral evolution of MP-15/MX suggests that this material is the most redox active.

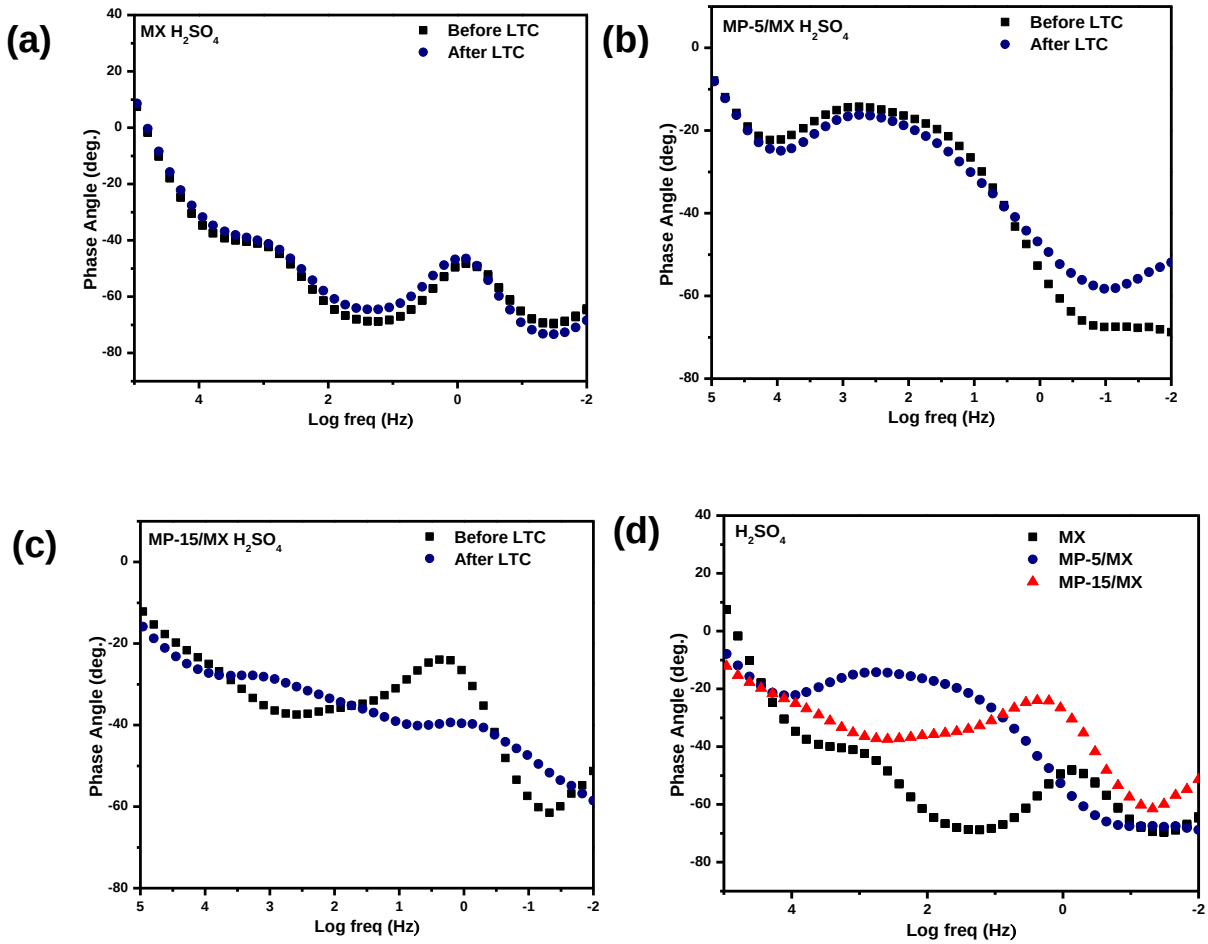

Figure 5.8: Phase angle Bode plot of (a) MX, (b) MP-5/MX, (c) MP-15/MX, and (d) an overlay of respective materials in 1 M H_2SO_4 systems

5.3 Reference List

[1] Shan, Q., Mu, X., Alhabeb, M., Shuck, C.E., Pang, D., Zhao, X., Chu, X-F., Weia, Y., Du, F., Chen, G., Gogotsi, Y., Gao, Y., and Dall'Agnese, Y. (2018). 'Two-dimensional vanadium carbide (V_2C) MXene as electrode for supercapacitors with aqueous electrolytes', *Electrochemistry Communications. Elsevier*, 96(September), pp. 103–107. doi: 10.1016/j.elecom.2018.10.012.

[2] Dall'Agnese, Y., Lukatskaya, M.R., Cook, K.M., Taberna, P-L., Gogotsi, Y., and Simon, P. (2014) 'High capacitance of surface-modified 2D titanium carbide in acidic electrolyte', *Electrochemistry Communications*, 48, pp. 118–122. doi: 10.1016/j.elecom.2014.09.002.

[3] Ghidiu, M., Lukatskaya, M.R., Zhao, Q-M., Gogotsi, Y., and Barsoum, M.W. (2014). 'Conductive two-dimensional titanium carbide "clay" with high volumetric capacitance', *Nature. Nature Publishing Group*, 516(7529), pp. 78–81. doi: 10.1038/nature13970.

[4] Hu, M., Li, Z., Hu, T., Zhu, S., Zhang, C., and Wang, X. (2016). 'High-Capacitance Mechanism for $Ti_3C_2T_x$ MXene by in Situ Electrochemical Raman Spectroscopy Investigation', *ACS Nano*, 10(12), pp. 11344–11350. doi: 10.1021/acsnano.6b06597.

[5] Lukatskaya, M.R., Kota, S., Lin, Z., Zhao, M-Q., Shpigel, N., Levi, M.D., Halim, J., Taberna, P-L., Barsoum, M.W., Simon, P., and Gogotsi, Y. (2017). 'Ultra-high-rate pseudocapacitive energy storage in two-dimensional transition metal carbides', *Nature Energy*, 6. doi: 10.1038/nenergy.2017.105

[6] Okubo, M., Sugahara, A., Kajiyama, S., and Yamada, A. (2018). 'MXene as a Charge Storage Host', *Accounts of Chemical Research*, 51(3), pp. 591–599. doi: 10.1021/acs.accounts.7b00481.

[7] Liu, J., Wang, J., Xu, C., Jiang, H., Chunzhong L., Zhang, L., Lin, J., and Shen, Z.X. (2018). 'Advanced Energy Storage Devices: Basic Principles, Analytical Methods, and Rational Materials Design', *Advanced Science*, 5(1). doi: 10.1002/advs.201700322.

[8] Wang, Y., Song, Y. and Xia, Y. (2016). 'Electrochemical capacitors: Mechanism, materials, systems, characterization and applications', *Chemical Society Reviews. Royal Society of Chemistry*, 45(21), pp. 5925–5950. doi: 10.1039/c5cs00580a.

CHAPTER 6

ELECTROCHEMICAL PERFORMANCE EVALUATION

NEAR-NEUTRAL ELECTROLYTE

The electrochemical charge storage mechanisms of the MX, MP-5/MX, and MP-15/MX were assessed in three-electrode configuration systems in near-neutral electrolyte. This part of our study presents the electrochemical evaluation of our materials in 1 M Li_2SO_4 based cells. This chapter is divided into two sections. Section 6.1 is focused on three electrode cells. Section 6.2 is focused on symmetrical cells where the CV, GCD, and PEIS results are presented and compared.

The pH of the 1 M Li_2SO_4 electrolyte was: 6.07.

6.1. Half-Cell Cyclic Voltammetry Studies – Lithium Sulphate Electrolyte

In 6.1.1. the general three electrode CV analysis will be discussed. In 6.1.2., according to the current (I) and scan rate (v) relationship, the charge storage mechanism kinetics will be studied. In 6.1.3. capacitive contributions will be quantified using total current (I) as a function of potential (V) related to the scan rate dependencies.

6.1.1 General Evaluation – Near-Neutral Electrolyte

The electrochemical behaviour of MX, MP-5/MX, and MP-15/MX in 1 M lithium sulphate electrolyte was probed with three-electrode CV testing performed at – 0.8 V to 0.8 V potential window at 5 to 100 mV/s sweep rate as depicted on Figure 6.1. The first thing that stands out with this half-cell lithium sulphate system is the widest potential window of 1.6 V achieved in this neutral media. This wide potential window outstands the known 1.23 V thermodynamic decomposition potential window of water which thus limits the aqueous based electrolyte systems to 1.0 V to prevent electrolyte decomposition [1]. This wide potential is known to be enabled by the highly solvated lithium cations [2].

A noticeable feature from the CV plots presented on Figure 6.1a-c is the signature curves characteristic of intercalation and deintercalation within layered electrode material [3]. This process is known as the lithiation and delithiation of the Li^+ ion between the MX layers and is commonly described as expressed on equation 6.1

$$Ti_2CO_x + yLi^+ + ye^- \rightleftharpoons Li_yTi_2CO_x \quad (\mathbf{6.1})$$

The most apparent difference between the three materials is the presence of redox peaks effected by the presence of MP. An assessment of the MP-5/MX and MP-15/MX CV evolutions as presented on Figures 6.1b and c respectively, shows more pronounced anodic peaks around -0.4 to -0.7 V voltages than in MP-15/MX than in miMP-5/MX. This shows that the presence of MP enhances the electrochemistry of the material in neutral electrolyte as well. Presumably, the presence of MP in

the MX in an inorganic salt based aqueous electrolyte is electrocatalytic for oxygen evolution reaction and oxygen reduction reactions at a 1.6 V operational window. Based on Figure 5.1d, according to the CV evolutions at various scan rates, the capacitance general trend in this system follows this order: MP-15/MX > MP-5/MX > MX.

The steady state for lithium sulphate-based cells were reached after a relatively long time. The longer time taken for the steady state to be reached shows that relative to acidic and alkaline electrolyte, lithium sulphate has sluggish or limited interaction with the electrode material.

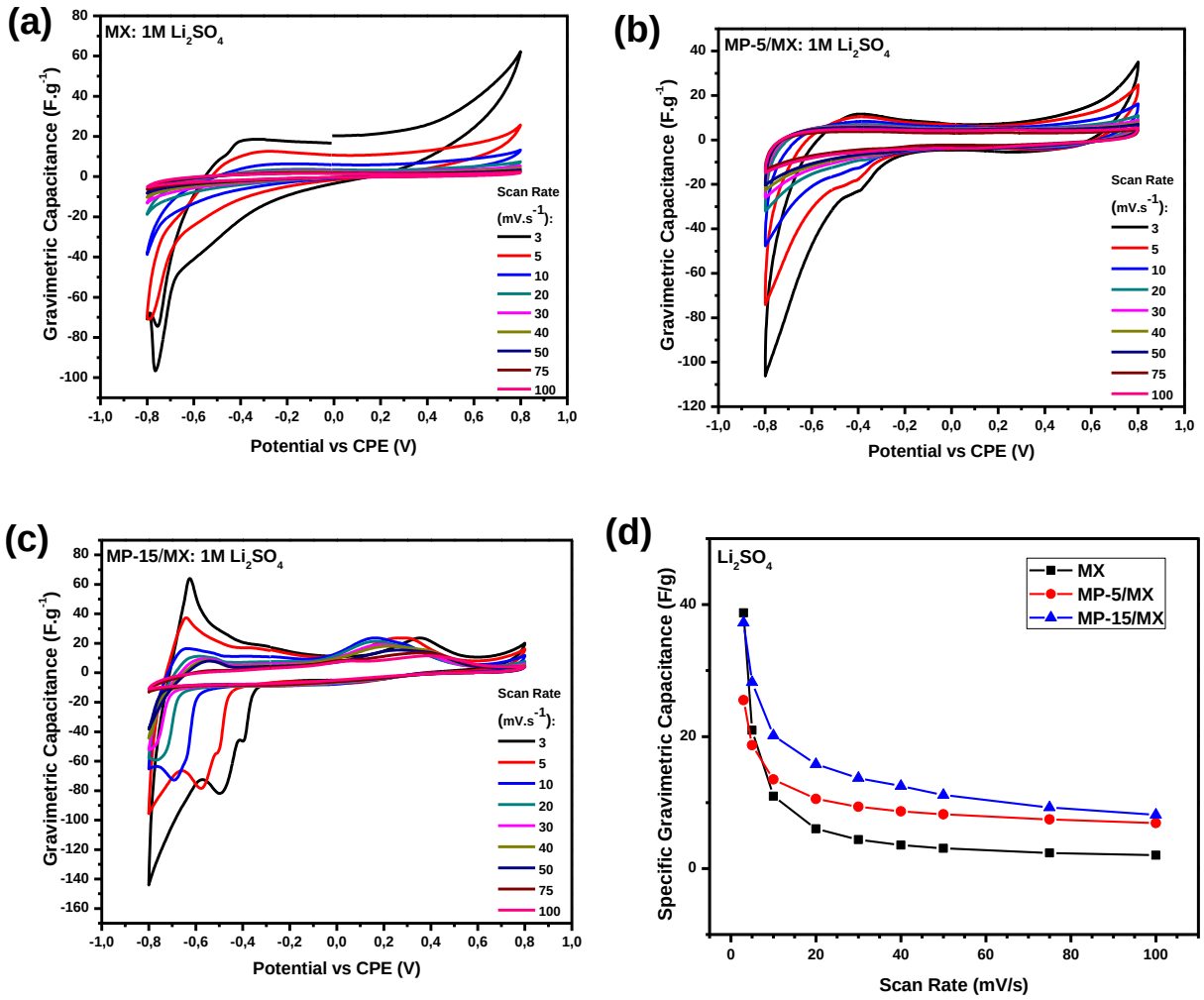

Figure 6.1: Cyclic voltammograms of (a) MX, (b) MP-5/MX, and (c) MP-15/MX in 1 M Li_2SO_4 electrolyte, and (d) the specific gravimetric capacitance comparison calculated from CV at different scan rates

6.1.2. Mechanism Studies: Charge Storage Kinetics – Near-Neutral Electrolyte

The assessment of the power law relationship between the current and scan rate at as a function of potential, like chapter 5 and 7, was used to determine the b-values of the half-cell systems from their CV loops as an indication of the electrochemistry reaction processes and kinetics involved in the performance of the MX, MP-5/MX, and MP-15/MX active materials. Observed in Figure 6.2b,d,f - the log scan rate vs log current linear fit, derived from the corresponding plots – Figure 6.21,c,e, the b-value similarities are similar for cathodic peaks. Cathodic peaks show low b-values ranging from 0.31 for MX to 0.43 for MP-15/MX to 0.47 for MP-5/MX. However, differences are significant for anodic peaks. Pristine MX has a 0.44 b-value while MP-5/MX and MP-15/MX show 0.80 and 0.84 b-values, respectively. The electrokinetic information that we can draw from these b-values is that the MX based cell is highly diffusion-controlled. Presumably, ions adsorb to deep trap sites of the active material thus exhibiting effecting an extremely intercalation redox activity. On the other hand, the similar b values obtained for MP incorporated MX shows the overall capacitance obtained from these materials is rather a combination of a diffusion-controlled behaviour and a capacitive behaviour. The anodic b-values at 0.8 are regarded as a transitional area meaning the pseudocapacitive charge storage mechanism is a combination of redox and intercalation pseudocapacitance, while the 0.4 cathodic b-value indicate battery-like processes.

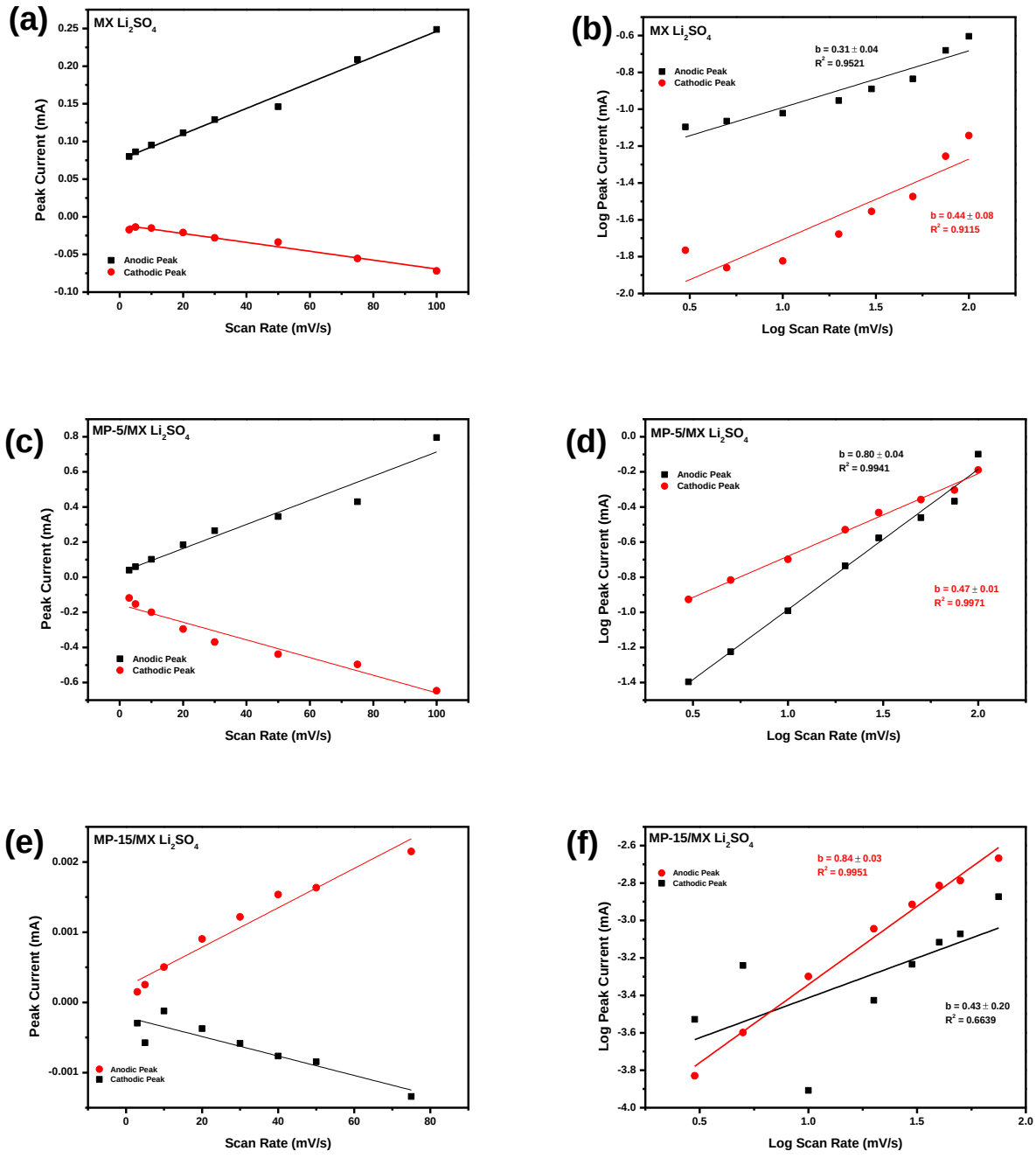

Figure 6.2: Linear power dependence plots, current (i) vs scan rate (v); log current (i) vs log scan rate (v) of: (a;b) MX, (c;d) MP-5/MX, and (e;f) MP-15/MX in 1 M Li_2SO_4 electrolyte

6.1.3. Mechanism Studies: Capacitive Contributions – Lithium Sulphate Electrolyte

Contribution studies were undertaken at 20 mV/s to quantify supercapacitive contributions as capacitive and/or diffusion controlled according to the current responses at specific potentials and its relationship to the sweep rates. Although MX is the most capacitive, the overall capacitance contribution for the three cells is relatively balanced in terms of diffusion and capacitance-controlled charge mechanisms. This can mean that 20 mV/s is an optimal scan rate for an almost balanced supercapacitive contribution as we theoretically, and empirically established in the preceding subsection that at low scan rates, there is more cation diffusion within the crystal lattice of the material thus resulting to higher pseudocapacitance.

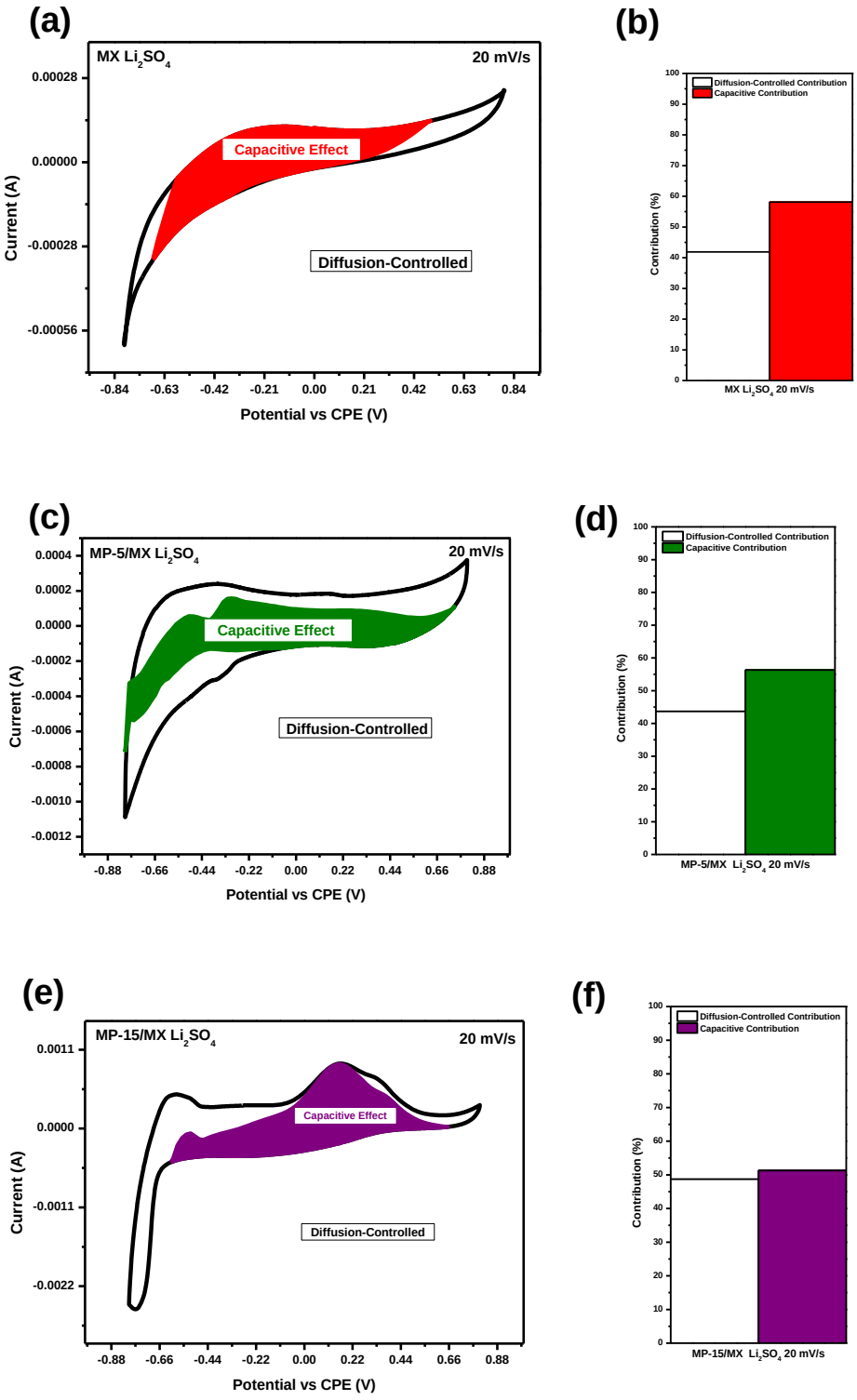

Figure 6.3: Diffusion-controlled and capacitive contribution determination cyclic voltammogram at 20 mV/s of (a) MX, (c) MP-5/MX, and (e) MP-15/MX at 20 mV/s for contribution studies; and corresponding bar graphs showing the contribution of different processes at 20 mV/s scan rate of (b) MX, (d) MP-5/MX, and (f) MP-15/MX in 1 M Li_2SO_4 electrolyte

6.2. Full Cells – Neutral Electrolyte

The CV curve of MP-15/MX on Figure 6.4e is characteristic of a resistive system compared to that of MX and MP-5/MX Figure 6.4a, c. This could be sterical hindrance due to the presence of the bulky MP between the MX layer impeding the fast charge transfer processes and mobility of the electrolyte ions. For MP-15/MX, if the mesopores are inhibited, ion mobility is limited as Li is larger than H in H_2SO_4. Another factor is the possible clogging of MX micropores which will account for less charge storage as deep trap sides are not participating in charge adsorption mechanism. As a result, in terms of the full cell performance, lowest power and lowest energy is observed. This electrochemical poor performance can be sustantiated by the physiochemical results obtained from surface area analysis in that MP-15/MX has lowest total pore volume and BET surface area results post MX synthesis relative to MX and MP-5/MX as a result of MP intercalation as showed on the BET surface area results. MP-5/MX proves to be the ideal material suggesting that the electrode material and electrolyte are well matched for an optimal electrolyte/electrode interface interaction. The CV profile of MP-5/MX shows a very gentle redox peak pair that is not apparent for MX and MP-15/MX CV curves. This could be indicative of pseudocapacitive mechanism at play when the lithiation and delithiation occurs without MP hinderences. It could even happen that MP is playing a synergistic role in facilitating charge and discharge processes.

MP-5/MX is the best performing material than MX, and MP-15/MX electrode materials. This might be because, MP at an optimal dosage, widens the interlayer spacing of MX allowing Li ions to move freely while MP plays an electrocatalytic

role in lithiation and delithiation of ions within the more exposed adsorption sites of the host MX network thus equating to less resistance and more pseudocapacity.

Worthy of being noted is that, as known in literature, the oxidation of the prisitine MX takes place at 0.6 V as shown on MX CV curve Figures 6.4a and MX GCD profile Figure 6b respectively. However, on MP-5/MX CV and GCD plots (Figures 6.4c,d) the gentle redox peak seems to play a protective role against material oxidation thus giving rise to higher capacitance and less resistance.

The charge/discharge profiles of these systems reveal interesting performance characteristics. In terms of columbic efficiency, MX Figure 6.4b exhibits the efficiency of 97.8% at 0.1 A/g but higher than 100% on current densities: 0.05, 0.15, 0.20, 0.25, and 0.30 A/g. MP-5/MX Figure 6.4d, shows an increasing columbic efficieny from 75.6% at 0.05 A/g to 95.5% at 10 A/g. MP-15/MX has an undesirable significantly high columbic efficiency of 190.34% at 0.10 A/g. This high columbic efficiency is over 100% at current densities 0.05 to 0.25 A/g.

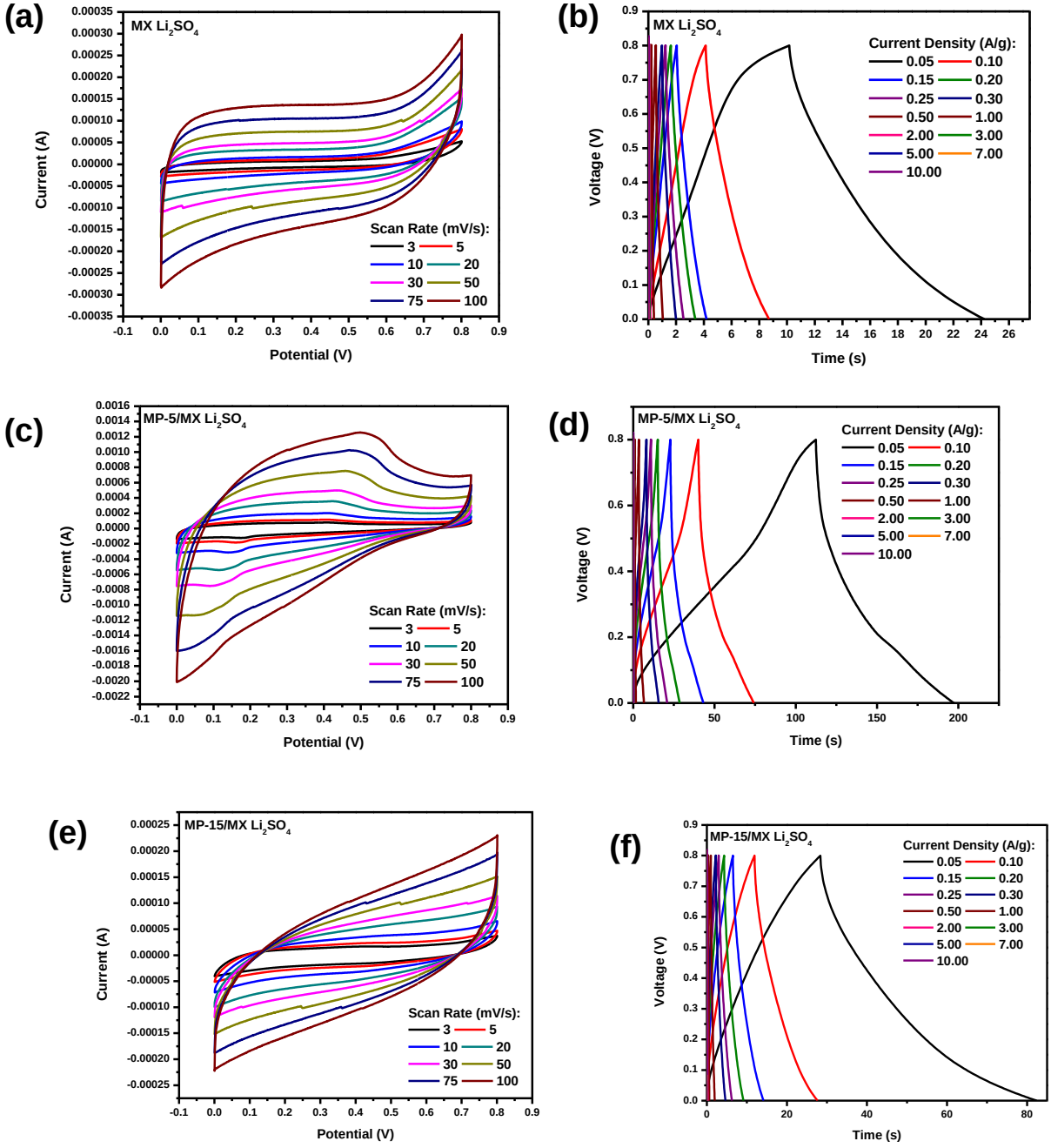

Figure 6.4: Two-electrode cyclic voltammograms of (a) MX, (c) MP-5/MX, and (e) MP-15/MX; and galvanostatic charge discharge profiles of (b) MX, (d) MP-5/MX, and (f) MP-15/MX in 1 M Li_2SO_4 electrolyte

The CV, GCD and Ragone comparison plots shown on Figure 6.5 show the higher gravimetric specific capacitance from CV curves on Figure 6.5a and GCD profiles on Figure 6.5b where MP-5/MX stands out as the highest performing device as shown on the corresponding Figure 6.5d and 6.5e representing the respective capacitances at respective scan rates and current densities. Figure 6.5e is a Ragone plot profiling the electrochemical performance of MX, MP-5/MX, as well as MP-15.MX in near-neutral lithium sulphate electrolyte. According to this representation, MP-5/MX has higher power density and a small change in terms of energy density compared to MX and MP-15/MX.

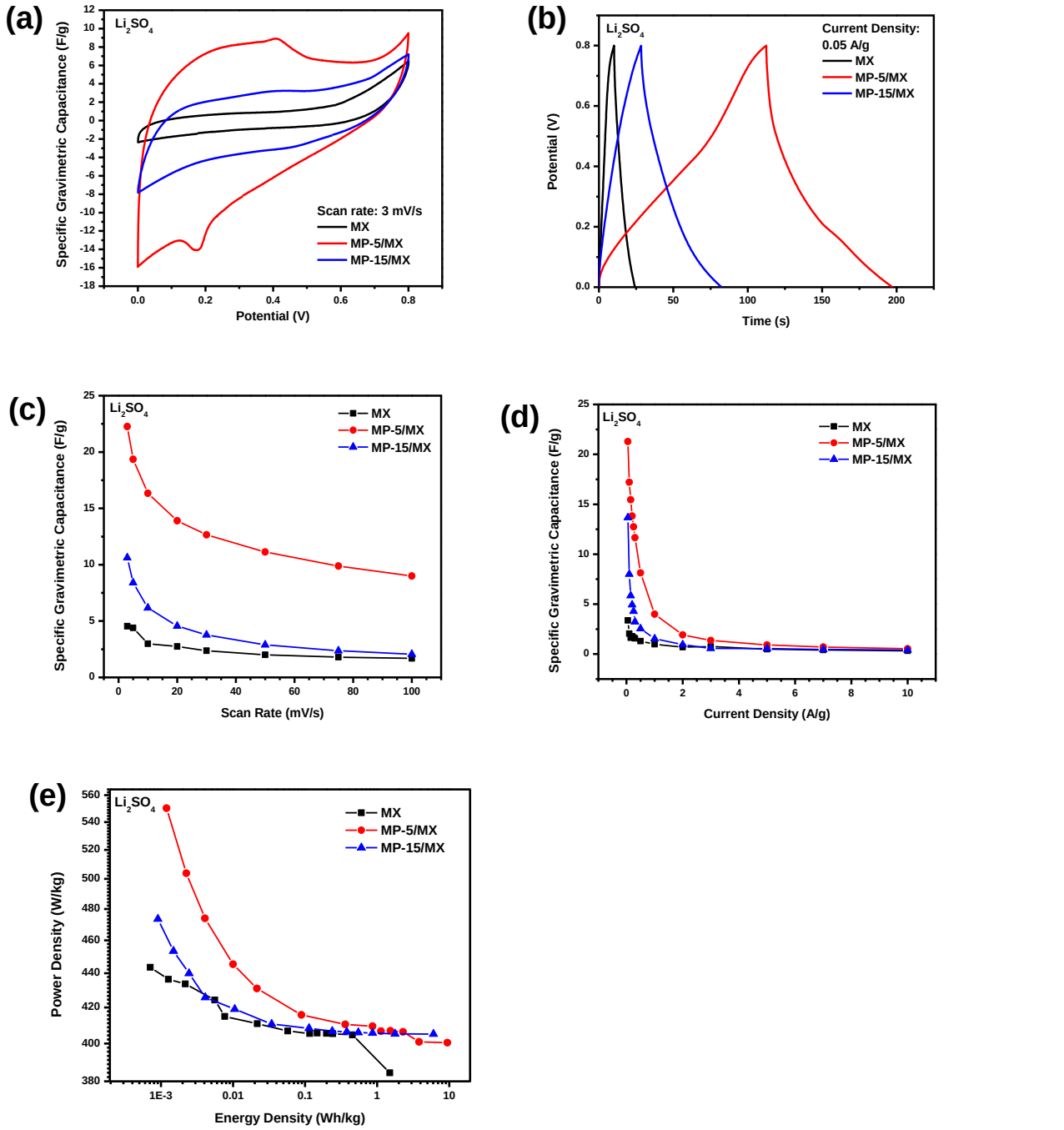

Figure 6.5: (a) Cyclic voltammogram specific gravimetric capacitance comparison of MX, MP-5/MX, and MP-15/MX at 3 mV/s; (b) Constant current charge/discharge profile comparison of MX, MP-5/MX, and MP-15/MX at 0.30 A/g; (c) Specific gravimetric capacitance comparison of MX, MP-5/MX, and MP-15/MX calculated from cyclic voltammogram areas at sweep rate range 3 to 100 mV/s; (d) Specific gravimetric capacitance comparison of MX, MP-5/MX, and MP-15/MX calculated from discharge time at constant current range 0.30 to 10.00 A/g; and (e) the Ragone plot of MX, MP-5/MX, and MP-15/MX in Li_2SO_4 system

Figure 6.6 depicts the cycling stability of MX, MP-5/MX, and MP-15/MX. After 8250 cycles, MX has retained a coulombic efficiency of 100% and 95.8 capacitance retention whereas MP-5/MX and MP-15/MX show a 98.4% and 100% coulombic efficiency at 5000 cycles with 100% capacitance retention, respectively. From these results, we can ascertain that neutral aqueous electrolyte provides good stability for MXene supercapacitor applications.

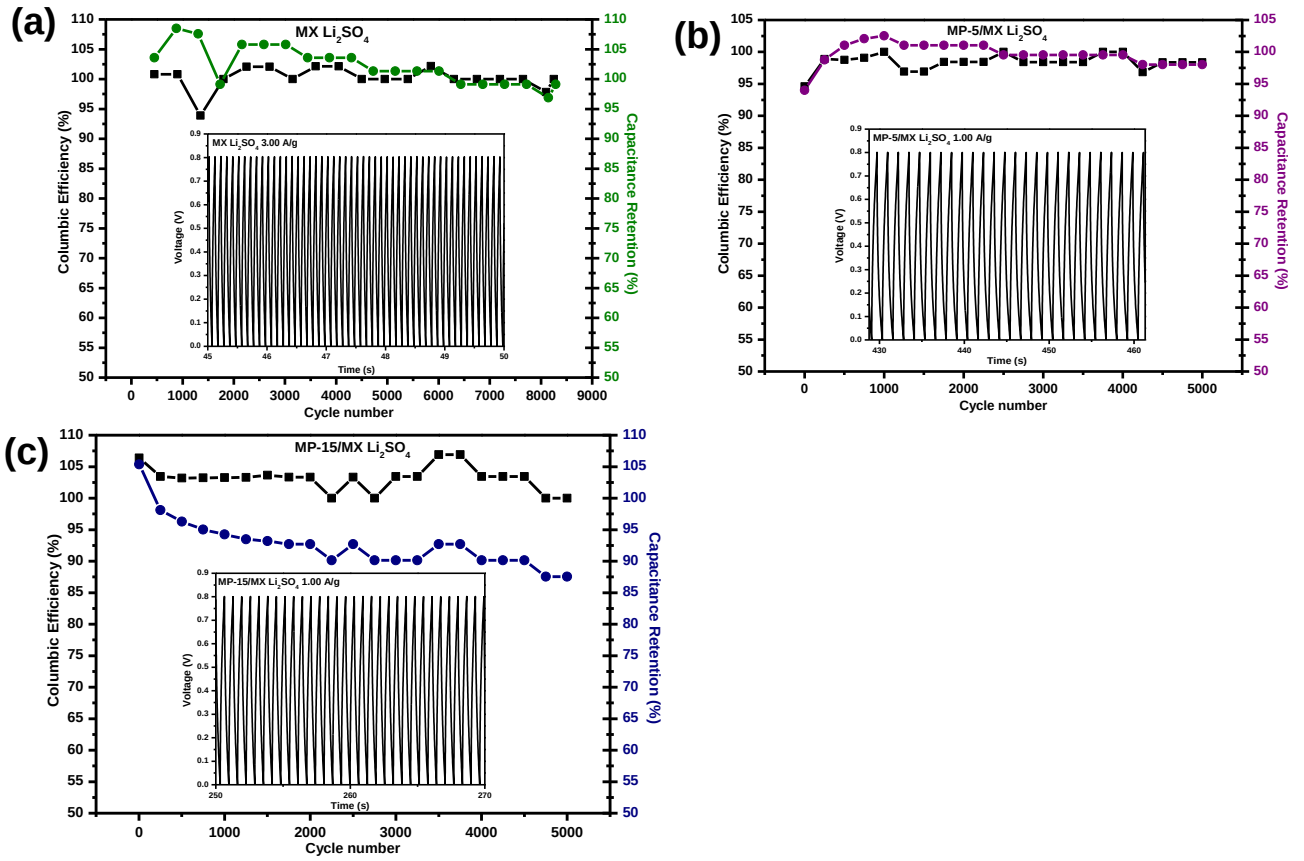

Figure 6.6: Long term cycling tests of (a) MX, (b) MP-5/MX, and (c) MP-15/MX of Li_2SO_4 devices

The symmetrical electrochemical performance was further assessed with EIS. The impedance response of the MX based symmetrical electrochemical system in Li_2SO_4 electrolyte media is represented in Nyquist and Bode plot formats on Figures 6.7 and 6.8 respectively. MX, MP-5/MX and MP-15/MX. These were obtained prior and post long term cycling of symmetrical cells to analyse the behavior of the materials before and after cycling. The shapes of the Nyquist plots and ESR values obtained from the x-axis interception of the respective plots before and after long term cycling tests exhibit significant changes in the overall cell resistance and ion kinetics. The ESR values are as follows: 1.587 Ω and 0.3973 Ω for MX Figure 6.7a, 1.3101 Ω and 0.8109 Ω for MP-5/MX; 0.8975 Ω and 0.6956 Ω for MP-15/MX. A comparison of the ESR trend prior to long term cycling tests suggest that ESR decreases as MP content is

increased. Secondly, the lithiation and delithiation processes of charge storage processes significantly modify the electrochemical performance of these materials in Li_2SO_4 electrolyte. The differences between the Nyquist plots –before LTC - of MX (Figure 6.7a), MP-5/MX (Figure 6.7c), and MP-15/MX (Figure 6.7e) is the evolution of the semi-circle in the high to intermediate frequency range and the diagonal line at low frequency range. These two features are representative of electrical conductivity and the diffusion processes of the electrolyte species in the electrode materials. Qualitatively, an observation is without MP within the MX nanosheets, the charge transfer resistance is the highest and decreases as MP in intercalated. This means the stacked MX layers retard the mobility of ions in the device if no intercalant is present to open up the slits for faster redox reactions. This phenomenon is supported by the longer diagonal line observed as the semi-circle diminishes with increased MP. Interestingly to note, the diagonal line becomes steeper after LTC. This inclination towards the imaginary impedance axis suggests the loss of pseudocapacitive properties as the materials are cycled.

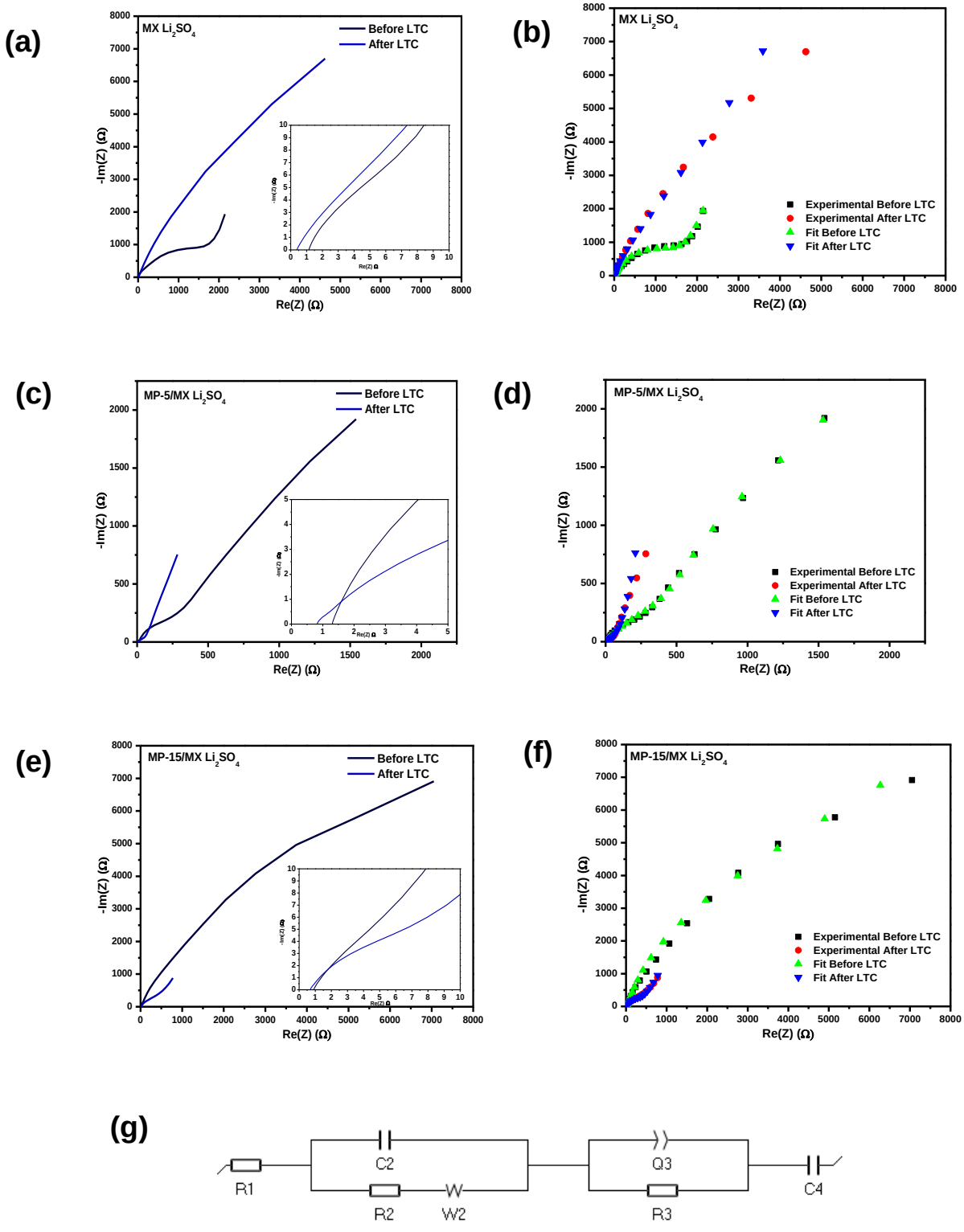

Figure 6.7: The Nyquist spectra of (a) MX, (b) MX fit, (c) MP-5/MX, (d) MP-5/MX fit, (e) MP-15/MX, (f) MP-15/MX fit, and (g) equivalent electric circuit used for the fitting of the 1 M Li_2SO_4 electrolyte based symmetrical devices before and after the stability tests to observe the changes in material impedence characteristics

Figures 6.7b, d, and e are the fitted plots for the purpose of modelling the impedance behaviour and derivation of quantitative estimations for a deeper interpretation according to the electric circuit shown on Figure 6.7g. The elements of the equivalent electric circuit selected for modelling the experimental data are R1+C2/(R2+W2)+Q3/R3+C4 where: R1 is the ESR, C2(R2+W3) involves the contact resistance as well as the Warburg diffusion impedance, pseudocapacitive properties and unaccounted possible parasitic or degradation resistance; element; Q3/R3 , constant phase element parallel to R3; as well as C4 representing intercalation capacitance. Table 6.1 provides the obtain values for each impedance tests and corresponding value for respective parameters.

Table 6.1: EIS fitting data for MX, MP-5/MX, and MP-15/MX in Li_2SO_4 electrolyte - symmetrical cell electrochemical performance (amplitude 3 mV, frequency) – before and after long term cycling as extraopolated from Nyquist plots.

	MX		**MP-5/MX**		**MP-15/MX**	
Parameters	**Before Cycling**	**After Cycling**	**Before Cycling**	**After Cycling**	**Before Cycling**	**After Cycling**
R1 (Ohm)	1.128 ± 0.4953	0.3702 ± 0.3562	1.129 ± 0.2725	0.7198 ± 0.6744	0.803 ± 0.2865	0.7544 ± 0.3498
C2 (F)	0.0122 e-3 ± 3.697 e-3	0.4924 ± 3.805 e-3	7.231 e-3 ± 0.3167 e-3	0.08412 e-3 ± 0.0867 e-3	0.8684 e-3 ± 0.05778 e-3	0.0204 e-3 ± 0.014.82 e-3
R2 (Ohm)	5.988 e-3 ± 313.8	1.107 ± 10904	1535 ± 163.6	0.9851 ± 3.802	2940 ± 92.53	2.309 ± 1.088
s2 (Ohm.s $^{-1/2}$)	206 ± 1.385	1199 ± 0.7065	63.3 ± 70.07	38.8 ± 9.54	1189 ± 136.4	146.3 ± 1.359
Q3 (F.s $^{a-1}$)	0.5832 e-3 ± 4.597 e-6	0.862 e-3 ± 0.9371 e-3	1.218 e-3 ± 26.83 e-6	0.02283 ± 2.099 e-3	1.676 e-3 ± 42.59 e-6	3.409 e-3 ± 0.1448 e-3
**C3 (F)*	0.5627 e-3	0.1852 e-3	1.055 e-3	8.16 e-3	7.699 e-3	3.409 e-3
n3	0.8705 ± 0.5048	0.7266 ± 0.7065	0.6287 ± 0.5078	0.4402 ± 0.6378	0.6101 ± 0.5116	0.9998 ± 1
R3 (Ohm)	1348 ± 16.01	19.48 ± 7.719	644 ± 42.75	63.12 ± 44.35	6484 ± 5559	198.4 ± 11.33
C4 (F)	0.01541 ± 0.2589 e-3	0.007604 ± 0.03953	0.01714 ± 5.771 e-3	0.02646 ± 0.6167 e-3	0.2004 ± 1.111	0.04473 ± 1.85 e-3
Chi ^{2}	0.2653	0.4575	0.473	0.1105	0.2985	0.2362

The asssesment of phase angle Bode represenations on Figure 6.8 (a) MX, (b) MP-5/MX, (c) MP-15 and (d) comparitive overlayof impedance results qualify the capacitance trend observed for the respective materials. As calculated from CV and GCD tests, MP-5/MX stands out from both MX and MP-15/MX. Because Bode plots are more sensitive to capacitance than Nyquist plots, an observable feature from these plots is MP-5/MX has the broadest and peculiar phase angle peaks.

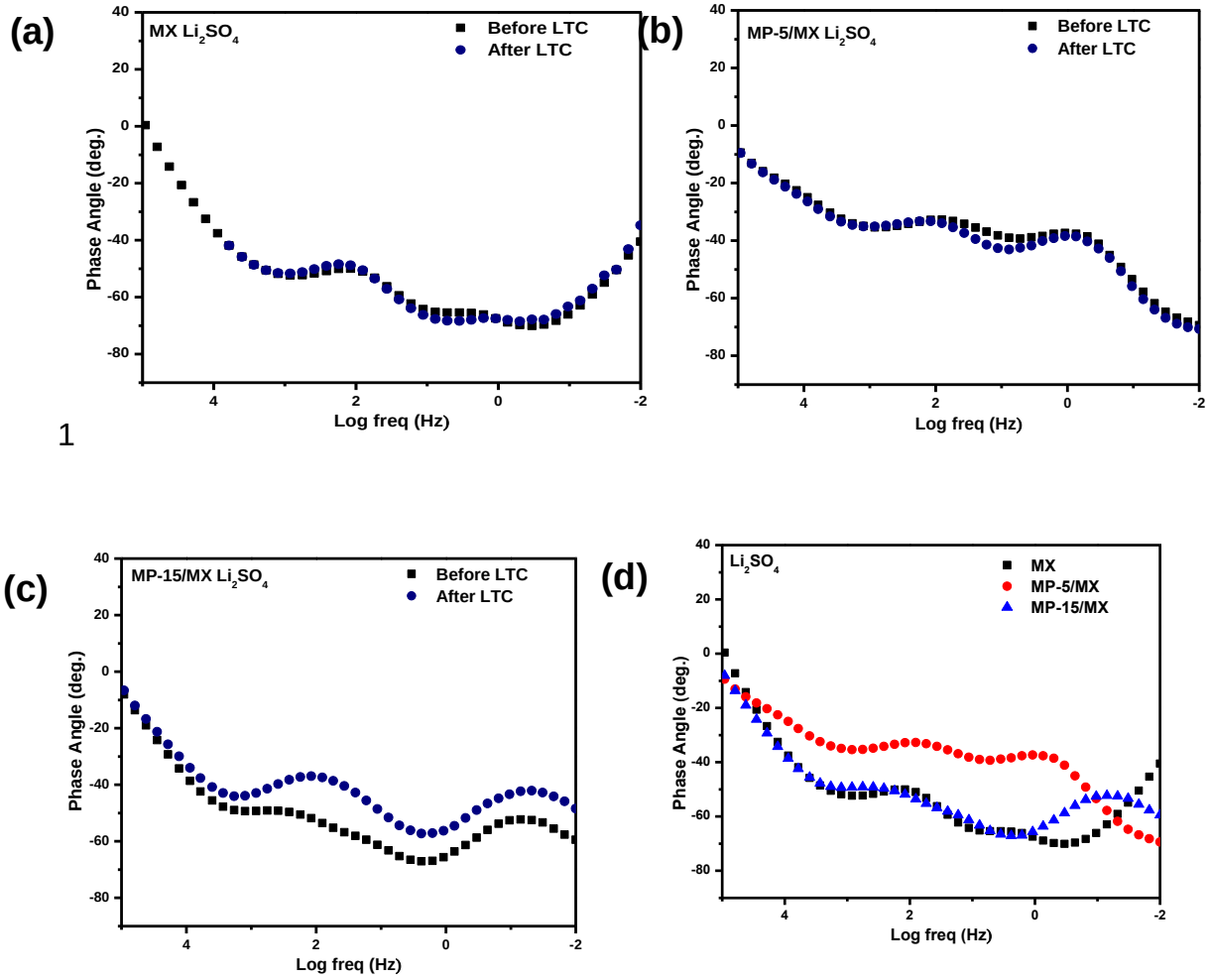

1

Figure 6.8: Phase angle Bode plot of (a) MX, (b) MP-5/MX, (c) MP-15/MX, and (d) an overlay of respective materials in 1 M Li_2SO_4 systems

6.3. Reference List

[1] Fic, K., Lota,G., Mellera, M., and Frackowiak, E. (2012). 'Novel insight into neutral medium as electrolyte for high-voltage supercapacitors', *Energy and Environmental Science*, 5(2), pp. 5842–5850. doi: 10.1039/c1ee02262h.

[2] Melchior S.A., Raju, K., Ike, I.S., Erasmus R.M., Kabongo, G., Sigalas, I., Iyuke, S.E., and Ozoemena, K.I. (2018). 'High-Voltage Symmetric Supercapacitor Based on 2D Titanium Carbide (MXene, Ti_2CT_x)/Carbon Nanosphere Composites in a Neutral Aqueous Electrolyte ', *Journal of The Electrochemical Society*, 165(3), pp. A501–A511. doi: 10.1149/2.0401803jes

[3] Naguib, M., Come, J., Dyatkin, B., Presser, V., Tabern, P-L, Simon, P., Barsoum, M.W., and Gogotsi, Y. (2012) 'MXene: A promising transition metal carbide anode for lithium-ion batteries', *Electrochemistry Communications. Elsevier B.V.*, 16(1), pp. 61–64. doi: 10.1016/j.elecom.2012.01.002.

CHAPTER 7

ELECTROCHEMICAL PERFORMANCE EVALUATION

ALKALINE ELECTROLYTE

It is known that alkaline electrolyte shows inferior electrochemical performance for MXenes [1]. So, this chapter is special in a sense because unlike work done on previous chapters for acidic and neutral electrolyte, it was performed at the advanced stages of the research after the materials, have oxidized due to ambient storage conditions. The aim was to attempt to explore the performance of oxidized MXenes in alkaline media as well as evaluate the role of MP in this exploration. To confirm oxidation, XPS was employed to assess chemical bonding, while SEM and TEM provided the morphology and microstructural transformations as presented in chapter 4. The electrochemical charge storage mechanisms of the MX, MP-5/MX, and MP-15/MX were assessed in three-electrode configuration systems in alkaline electrolyte. This part of our study presents the electrochemical evaluation of our materials in 1 M LiOH based cells. This chapter is divided into two sections. Section 7.1 is focused on three electrode cells while section 7.2 is focused on symmetrical cells where the CV, GCD, and PEIS results are presented and compared.

The pH of the 1 M LiOH electrolyte was: 11.93.

7.1. Half-Cell Cyclic Voltammetry Studies – Alkaline Electrolyte

In 7.1.1. the general three electrode CV analysis will be discussed. In 7.1.2., according to the current (I) and scan rate (v) relationship, the charge storage mechanism kinetics will be studied. In 7.1.3. capacitive contributions will be quantified using total current (I) as a function of potential (V) related to the scan rate dependencies.

7.1.1 General Evaluation –Alkaline Electrolyte

To gain insight on the electrochemical activity of the as-synthesized materials in alkaline electrolyte, cyclic voltammetry scans were looped at the potential range of – 0.4 V to 0.4 V giving us a window potential of 1.0 V at scan rates 3 to 100 mV/s as depicted on Figure 7.1.

The rectangular shaped CV curve of MX Figure 7.1a indicates the capacitive behaviour of MX in 1 M LiOH as opposed to the shapes of MP-5/MX Figure 7.1b and MP-15/MX Figure 7.1c which present distorted rectangular CV evolutions. MXenes in alkaline media exhibit a capacitive behaviour [2]. So, the distorted curves can be attributed to the addition of MP to MX. They indicate the pseudocapacitive effects introduced by the nitrogen rich, metallo-complex as well as the resistance ions must overcome to access redox active sites on the material surface as material is added to MX. Furthermore, MX is known to have weak electrochemical performance in basic environments because of the low conductivity of hydroxyl electrolyte [3]. It is also suggested that in the presence of

the electrolyte with excess hydroxylated groups, MXene titanium oxides surfaces cannot interact with the dissociated hydroxyl anions to effect changes in the oxidation state of the material surface, and hydroxylated groups are known to destabilize host material by substituting F in the Ti-F bond with -OH. Cations are intercalating, not anions [4].

Figure 7.1d shows the specific gravimetric capacitance calculated from CV curves and show that the addition of MP to MX increased the specific gravimetric capacitance.

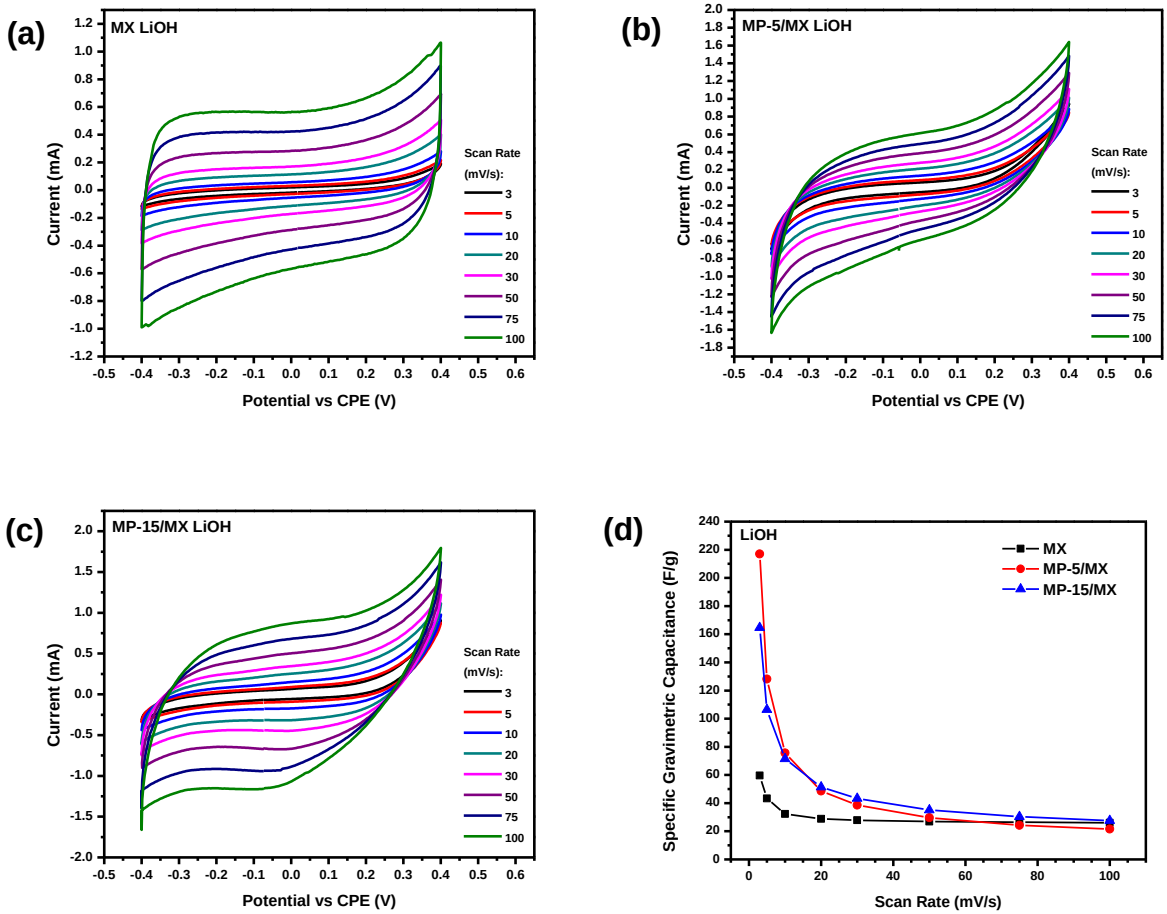

Figure 7.1: Cyclic voltammograms of (a) MX, (b) MP-5/MX, and (c) MP-15/MX in 1 M LiOH electrolyte, and (d) the specific gravimetric capacitance comparison calculated from CV at different scan rates

7.1.2. Mechanism Studies: Charge Storage Kinetics – Alkaline Electrolyte

To get insight into the mechanisms at play in the supercapacitive performance of the MX, MP-5/MX and MP-15/MX materials in alkaline solution, the power law dependence of the peak and scan rate method used in chapters 5 and 6 was used to establish the b-value of the materials. Figure 7.2a,c,e shows the current vs scan rate peak fittings. A b-value of 0.96 showed on Figure 7.2b, that is very close to 1.0 was determined for MX. When b = 1, the mechanism that controls the charge storage is highly capacitive. MP-5/MX and MP-15/MX showed b-values that are intermediate ranging from 0.67 to 0.85 showed on Figure 7.2d,f, also classified as ‘transitional’. This proves that the presence of MP enhances the pseudocapacitance of charge storage. Also, important to note is although MX is highly capacitive, the anodic and cathodic processes are the same, implying good reversibility whereas there is significant difference on MP-15/MX meaning that the redox reactions involved are not entirely the same as the cathodic b-value is more towards a capacitive behaviour than the anodic b-value.

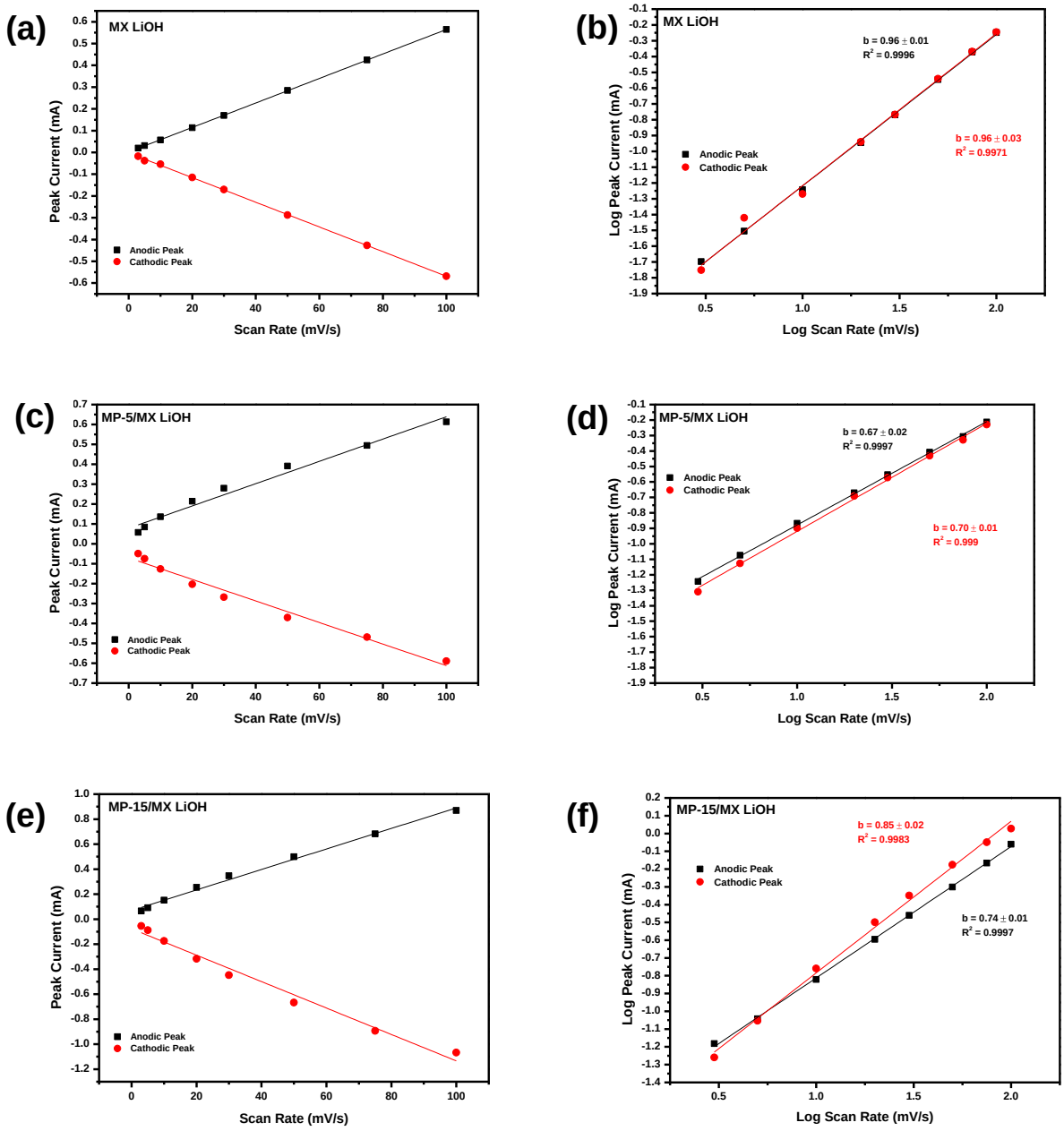

Figure 7.2: Linear power dependence plots, current (i) vs scan rate (v); log current (i) vs log scan rate (v) of: MX (a;b), MP-5/MX (c;d), and MP-15/MX (e;f) in 1 M LiOH electrolyte

7.1.3. Mechanism Studies: Capacitive Contributions – Alkaline Electrolyte

Presented in this subsection is the assessment of the capacitive and diffusion-controlled contributions. The scan rate of 20 mV/s was chosen for the estimation of the extent of each contribution for the materials of study. Figure 7.3a,c,e depict the CV evolutions of the materials and the capacitive approximated capacitive contribution. Figure 7.3b,d,e present the resulting contribution by percentages. MX in LiOH is highly capacitive with only 15.2% of capacitance emerging from diffusion-controlled charge storage mechanism and processes. This finding corresponds well to the b value obtained on Figure 7.2b and proves that in basic media, MXene is highly capacitive than pseudocapacitive. We can therefore, based on this behaviour expect low capacitance from alkaline media than acidic media. The addition of MP effects a decline in the capacitance contribution. Pristine MX has a high 84.8% surface-controlled capacitance that declines to 57.4% for MP-5/MX and further low to 47.2% for MP-15/MX. Figure 7.3b and c show that as MP is added, the charge storage mechanism becomes more diffusion controlled. From this behaviour, we can deduce that the MP enhancement might be useful for improving on the capacitance of MXenes in aqueous, alkaline electrolyte to modify redox activity. Also, the increase in diffusion-controlled charge storage contribution as MP is increased may be due to the increase in the interlayer spacing of MX, thus enabling cations to have more access to active sites.

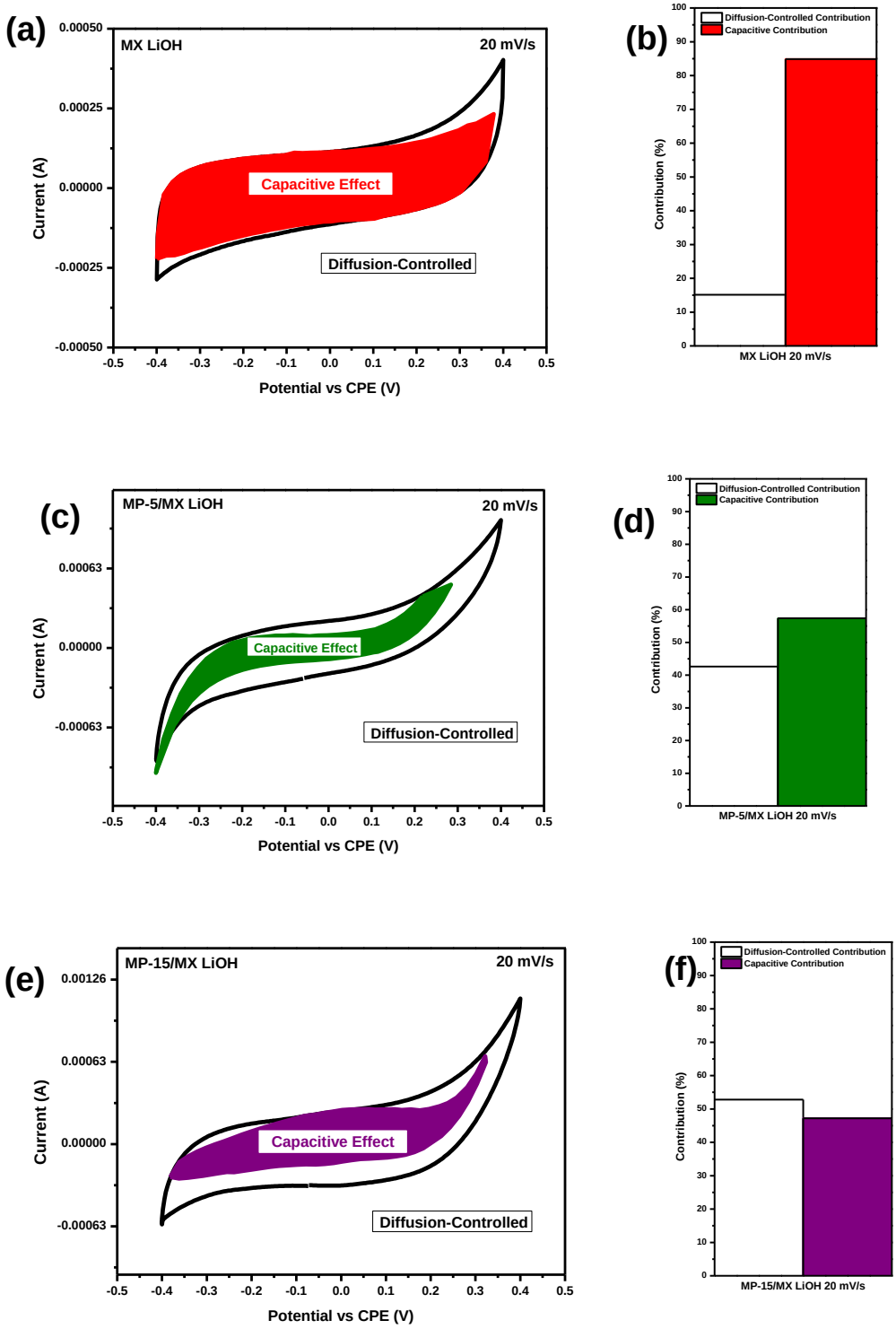

Figure 7.3: Diffusion-controlled and capacitive contribution determination cyclic voltammogram at 20 mV/s of (a) MX, (c) MP-5/MX, and (e) MP-15/MX at 20 mV/s for contribution studies; and corresponding bar graphs showing the contribution of different processes at 20 mV/s scan rate of (b) MX, (d) MP-5/MX, and (f) MP-15/MX in 1 M LiOH electrolyte

7.2. Symmetrical Cell: Cyclic Voltammetry – Alkaline Electrolyte

The quasi-rectangular CV evolutions of MX, MP-5/MX and MP-15/MX symmetrical cell tests shown in Figure 7.4 show a capacitive behaviour-like CV evolutions. One feature that modestly stands out is the resistance on the MX CV Figure 7.4a. The absence of the CV tailing at anodic sweeps for the doped material voltammograms as shown in Figure 7.4c,e implies that the non-oxidative property is induced by the presence of the nitrogen rich MP. The narrow voltage window of LiOH based symmetrical cells and the respective current response compared to the acidic and neutral media tested in this confirmed in this work. This inferior performance does not vary much for all materials tested. This may indicate that, unlike in acidic and neutral electrolyte where MX was in its prime quality, alkaline media has extremely little to no effect on the inferior electrochemical performance of oxidized MX even in the presence of MP. GCD tests presented on Figure 7.4b,d,f show that at 0.025 A/g, although with great resistance and coulombic efficiency of 109%, MP-15/MX could charge whereas MX was able to charge at 0.1 A/g. MX and MP-5/MX show comparable capacitances but a trend cannot be derived from this study.

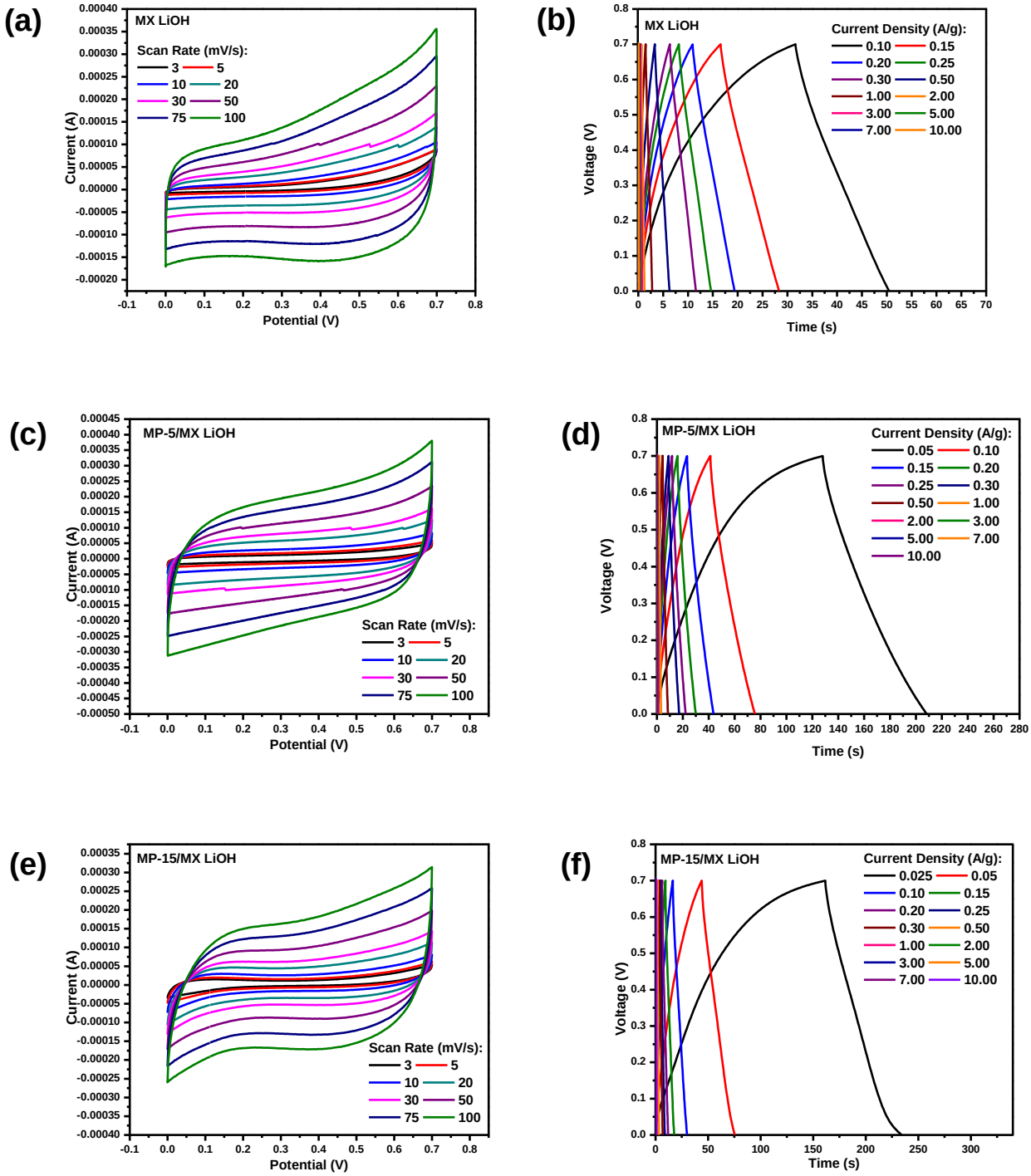

Figure 7.4: Two-electrode cyclic voltammograms of (a) MX, (c) MP-5/MX, and (e) MP-15/MX; and galvanostatic charge discharge profiles of (b) MX, (d) MP-5/MX, and (f) MP-15/MX in 1 M LiOH electrolyte

Figure 7.5 presents a summary of CV and GCD results, as well as the Ragone plot. On Figure 7.5a the CV evolutions of the three materials at 3 mV/s suggests that MP-15/MX has high resistance and is more prone to electrolyte/material degradation. This implies that the presence of MP is does not play an advantageous role in terms of cell performance. This is confirmed by the presented power and energy performance of MP-15/MX on Figure 7.5e MP-15/MX gives the most inferior energy and power densities than MX and MP-5/MX. According to Figure 7.5b, at 0.1A/g MP-5/MX has the highest capacitance of 19.7 F/g followed by 10.7 and 7.80 F/g for MX and MP-15 F/g respectively. When evaluating the performance of MX and MP-5/MX on Figure 7.5c and d, inconsistencies in terms of capacitance are realized. This can be indicative of cell instabilities as various tests are performed. However, MP-5/MX has the highest energy density of all materials.

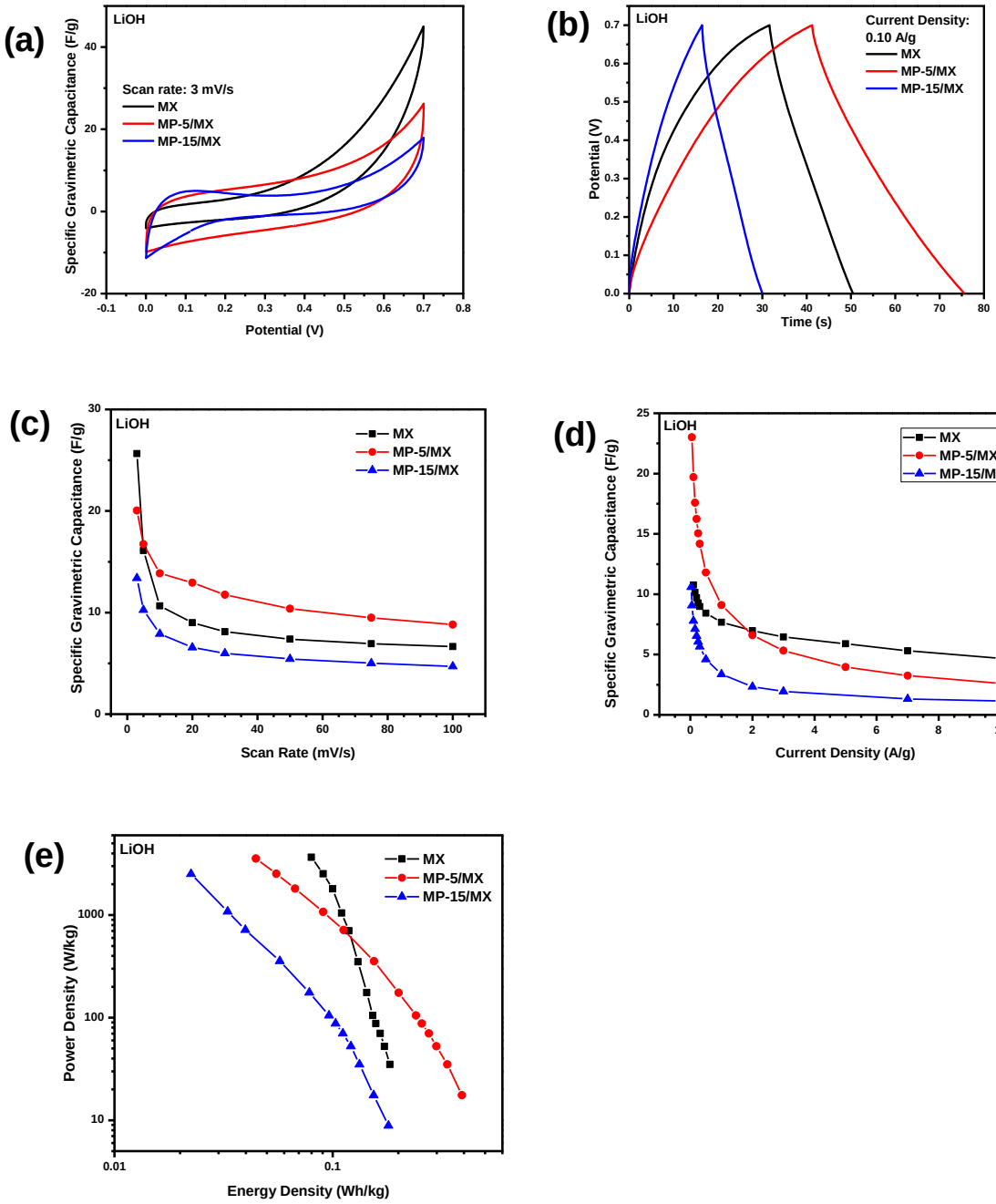

Figure 7.5: (a) Cyclic voltammogram specific gravimetric capacitance comparison of MX, MP-5/MX, and MP-15/MX at 3 mV/s; (b) Constant current charge/discharge profile comparison of MX, MP-5/MX, and MP-15/MX at 0.10 A/g; (c) Specific gravimetric capacitance comparison of MX, MP-5/MX, and MP-15/MX calculated from cyclic voltammogram areas at sweep rate range 3 to 100 mV/s; (d) Specific gravimetric capacitance comparison of MX, MP-5/MX, and MP-15/MX calculated from discharge time at constant current range 0.10 to 10.00 A/g; and (e) the Ragone plot of MX, MP-5/MX, and MP-15/MX in 1 M LiOH system

Figure 7.6 shows stability test profiles of MX, MP-5/MX and MP-15/MX full cell systems studied via constant current charge/discharge long term cycling for a minimum of 5000 cycles at a 0.50 A/g current density. Figure 7.6a and 7.6b show a similar performance trend in a sense that there is a drastic capacitance fall off as cycling proceeds, more especially at 2000 cycles onwards. This may indicate the effect of MP in delaying Ti-OH saturation as MP-15/MX exhibits an opposite behaviour. Figure 7.6c for MP-15/MX shows low capacitance retention and lower coulombic efficiency as the long-term cycling starts till about 1000 cycles, followed by higher capacitance retention as well as coulombic efficiency. This is suggestive of Li ions diffusing more effectively as more ion transport channels are created in the electrode material as more cycles accumulate.

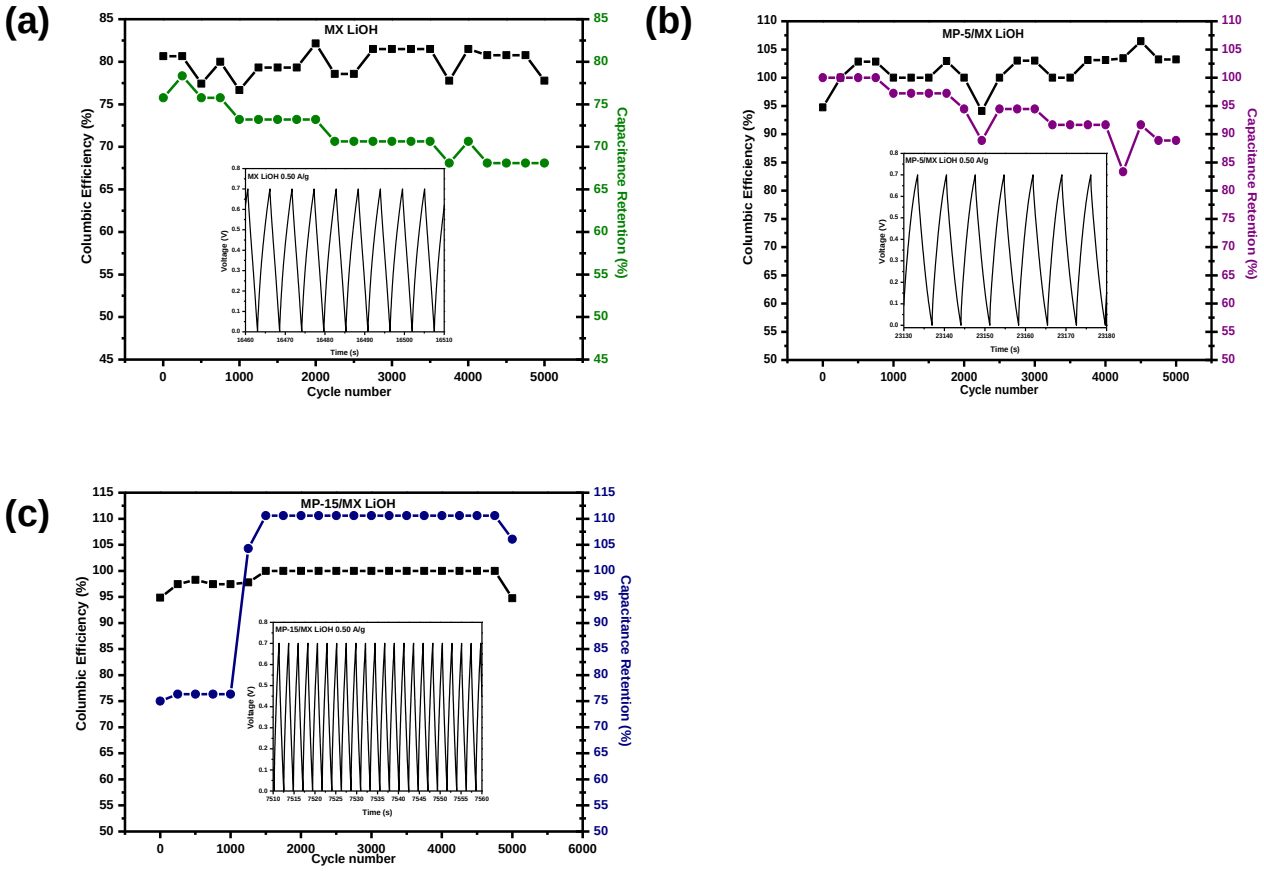

Figure 7.6: Long term cycling tests of (a) MX, (b) MP-5/MX, and (c) MP-15/MX of LiOH devices (c)

For LiOH based symmetrical electrode devices, EIS was used to analyse ion kinetics for characterizing the charge storage processes. This impedance test was done undertaken at the 200 kHz to 10 mHz frequency range with a 0.003 V applied open circuit potential. Figure 7.7 demonstrates the Nyquist EIS data of the MX, MP-5/MX and MP-15/MX prior and post galvanostatic charge/discharge long term cycling tests. Presented in Figure 7.7a and b is the generated Nyquist empirical and fitted plot for MX for comparing the alterations in the impedance parameters effected by stability testing. The obtained Nyquist curves are typical of capacitive charge processes. The curve interception of the real impedance at high frequencies is attributed to the equivalent series resistance of the electrochemical device. The pre and post LTC ESR responses for MX are 0.4423 Ω and 0.4405 Ω, MP-5/MX 0.4359 Ω and 0.4324 Ω, MP-15 0.4309 Ω and 0.4159 Ω. These ESR values are extremely close to each other. However, the stark differences between the pre and post LTC tests for the three materials are in the diagonal line in low frequencies. Interestingly the apparent transformation is in how steep the line becomes after long term charge and discharge processes. This might mean the electrolyte – electrode surface interaction becomes more capacitive as a result of possibly the degradation of the electrolyte or non-reversibly redox processes. Table 7.1 provides the fitting data according to the circuit on Figure 7.6 g.

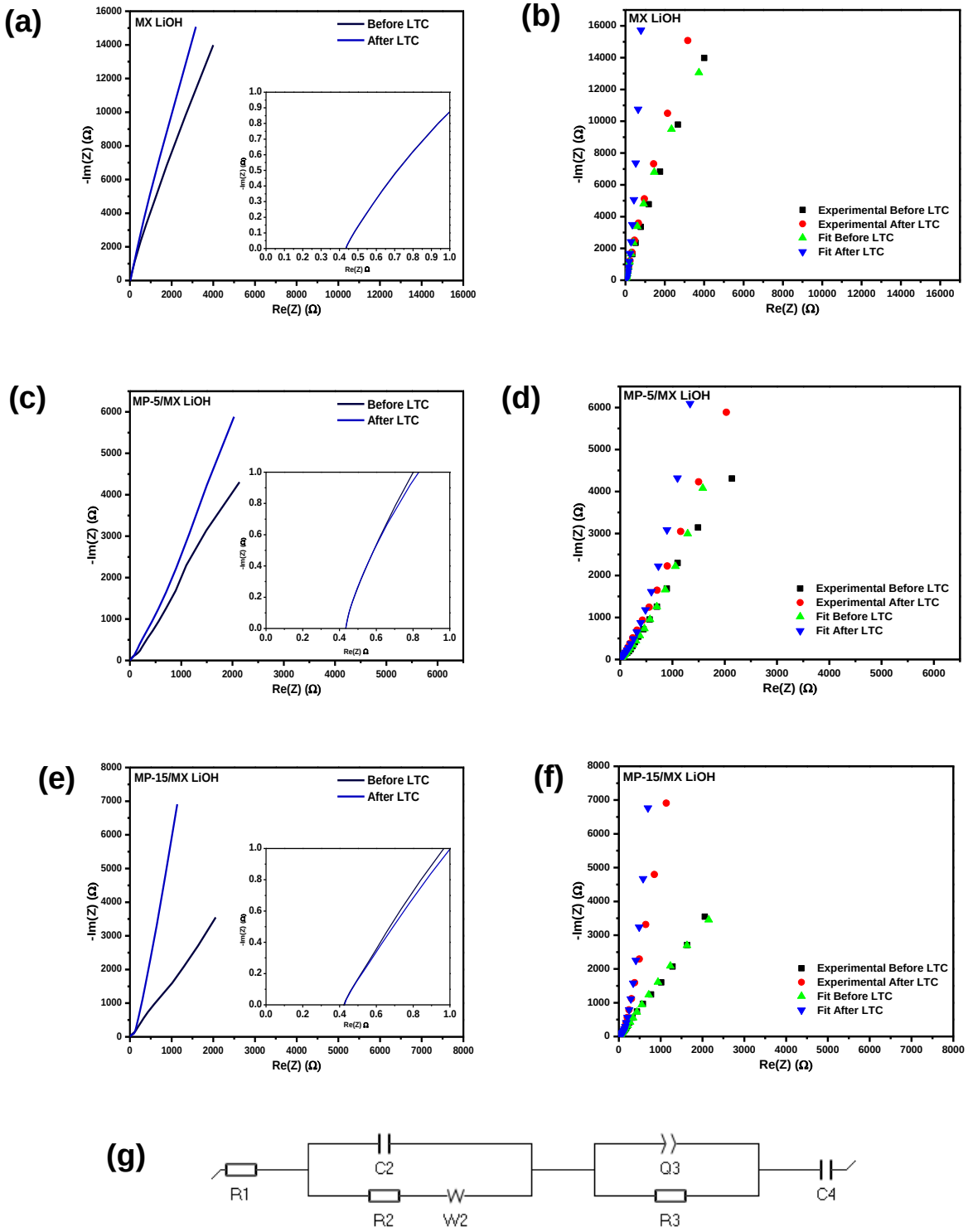

Figure 7.7: The Nyquist spectra of (a) MX, (b) MX fit, (c) MP-5/MX, (d) MP-5/MX fit, (e) MP-15/MX, (f) MP-15/MX fit, and (g) equivalent electric circuit used for the fitting of the 1 M LiOH electrolyte based symmetrical devices before and after the stability tests to observe the changes in material impedance characteristics

Table 7.1: EIS fitting data for MX, MP-5/MX, and MP-15/MX in LiOH electrolyte - symmetrical cell electrochemical performance (amplitude 3 mV, frequency) – before and after long term cycling as extraopolated from Nyquist plots.

	MX		**MP-5/MX**		**MP-15/MX**	
Parameters	**Before Cycling**	**After Cycling**	**Before Cycling**	**After Cycling**	**Before Cycling**	**After Cycling**
R1 (Ohm)	0.4684 ± 0.3898	0.4332 ± 0.5523	0.4297 ± 0.4427	0.4322 ± 0.4219	0.3528 ± 0.25	0.459 ± 1
C2 (F)	0.02639 e-3 ± 0.0593 e-3	0.2203 e-3 ± 0.04345	0.1438 e-3 ± 8.149 e-3	0.1482 e-3 ± 9.548 e-3	1.666 e-3 ± 2.379	0.0174 e-6 ± 1
R2 (Ohm)	0.7857 ± 1.332	0.1457 ± 3494	0.6317 ± 2660	0.3717 ± 2225	0.2824 ± 41690	0.7049 ± 1
s2 (Ohm.s $^{-1/2}$)	90.36 ± 4.383	201.1 ± 1.001	406.3 ± 1.336	342.8 ± 1.123	936 ± 121	163.4 ± 1
Q3 (F.s $^{a-1}$)	1.653 e-3 ± 9.967 e-6	0.5642 e-3 ± 0.01013	0.4143 e-3 ± 5.15 e-3	0.2246 e-3 ± 3.122 e-3	1.973 e-3 ± 1.2.4 e-3	0.8335 e-3 ± 1
**C3 (F)*	2.293 e-3	0.06454 e-3	0.1029 e-3	0.06672 e-3	1.68 e-3	0.8335 e-3
n3	0.9094 ± 0.5246	0.7494 ± 1	0.8208 ± 1	0.8546 ± 1	0.6025 ± 0.6101	1 ± 0.5
R3 (Ohm)	16.16 ± 1.051	2.709 ± 26.51	4.096 ± 32.14	3.549 ± 20.43	397.3 ± 389	44.47 ± 0.568
C4 (F)	2.213 e-3 ± 22.49 e-6	1.067 e-3 ± 0.3338 e-6	6.476 e-3 ± 13.46 e-6	3.369 e-3 ± 3.45 e-6	0.06981 ± 0.06779	2.604e-3
Chi ^{2}	0.1380	0.1759	0.2036	0.1699	0.468	0.1345

The Bode representations on Figure 7.8 provide an overview of the capacitance behaviour of the materials. Figure 7.8a shows that MX has the least variation in its capacitive performance even after LTC tests. Figures 7.8b and c are more active similarly to their CV evolutions as a result of the MP presence. This MP presence in LiOH media contributes to the overall cell performance but yields to sluggish power performance.

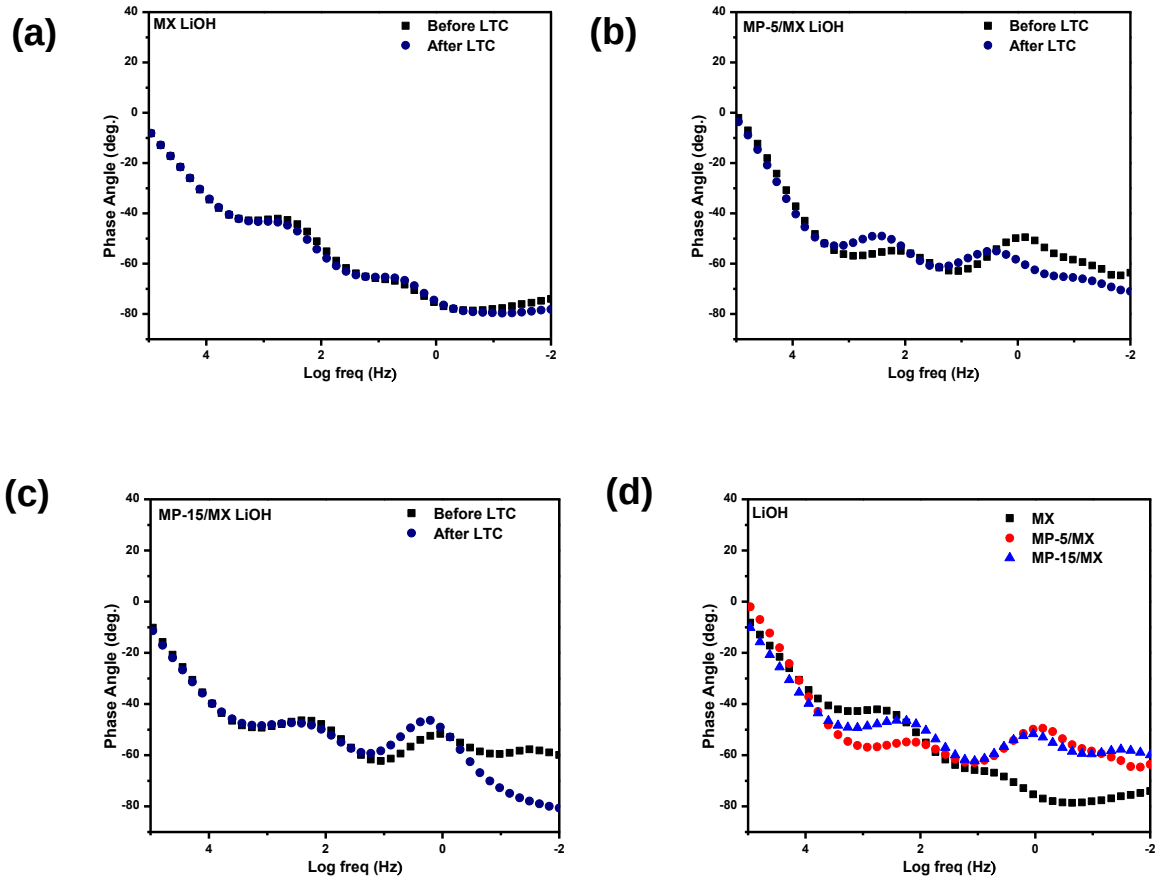

Figure 7.8: Phase angle Bode plot of (a) MX, (b) MP-5/MX, (c) MP-15/MX, and (d) an overlay of respective materials in 1 M LiOH systems

7.3. Reference List

[1] Shan, Q., Mu, X., Alhabeb, M., Shuck, C.E., Pang, D., Zhao, X., Chu, X-F., Weia, Y., Du, F., Chen, G., Gogotsi, Y., Gao, Y., and Dall'Agnese, Y. (2018). 'Two-dimensional vanadium carbide (V_2C) MXene as electrode for supercapacitors with aqueous electrolytes', *Electrochemistry Communications. Elsevier*, 96(September), pp. 103–107. doi: 10.1016/j.elecom.2018.10.012.

[2] Lukatskaya M.R., Mashtalir, O., Ren, C.E., Dall'Agnese, Y., Rozier, P., Taberna, P.L., Naguib, M., Simon, P., Barsoum, M.W., and Gogotsi, Y. (2013). 'Cation intercalation and high volumetric capacitance of two-dimensional titanium carbide', *Science*, 341(6153), pp. 1502–1505. doi: 10.1126/science.1241488.

[3] Pal, B., Yang, S., Ramesh, S., Thangadurai, V., and Jose, R. (2019).'Electrolyte selection for supercapacitive devices: A critical review', *Nanoscale Advances. Royal Society of Chemistry*, 1(10), pp. 3807–3835. doi: 10.1039/c9na00374f.

[4] Li, J., Yuan, X., Lin, C., Yang, Y., Xu, L., Du, X., Xie, J., Lin, J., and Sun, J. (2017). 'Achieving High Pseudocapacitance of 2D Titanium Carbide (MXene) by Cation Intercalation and Surface Modification', Advanced Energy Materials, 7(15). doi: 10.1002/aenm.201602725.

CHAPTER 8

CONCLUSION, RECOMMENDATIONS AND FUTURE PERSPECTIVES

Conclusion

The in-situ HF synthesis of MXenes from their MAX precursors is simple, less harmful and effective. However, high fluorine surface termination content might have an adverse effect on the electrochemical performance of the MXene materials. The integration of NiTpyzPz into the MXene sheets can be facilitated as the delamination step in the synthesis protocol of MXenes to avoid multiple steps in the intercalation process. The assorted chemical properties of MXenes and metallotetrazinopophyrazines have synergistic effect in supercapacitive performance of materials in aqueous electrolyte. Aqueous electrolyte can be used in MXene-Metallotetrazinoporphyrazine electrochemical storage research for supercapacitor application. Light MXenes are susceptible to oxidation at ambient and therefore need to be stored in controlled environments. The MP intercalation as a wet chemical post-synthesis treatment step has boosted the electrochemical capacitance performance of MX in acidic electrolyte, caused sluggish reactions in near-neutral electrolyte systems, and inferior capacitive performance in alkaline electrolyte. The disappearance of Ti_2AlC trace peaks on the XRD spectra and corresponding EDS results prove that Al was successfully removed by LiF-HCl synthesis further terminating the MX surfaces with OH, O, and F functionalities. H_2SO_4 electrolyte provides the highest capacitance. LiOH electrolyte is inferior and Li_2SO_4 has potential for high energy storage supercapacitor storage devices.

Recommendations

The synthesis of MXenes should involve a thorough method of washing of F terminates surface functionalities. The exfoliation parameters should be varied to optimize the MXene synthesis method that will yield MXene sheets with less titanium oxidation and graphitic carbon. In terms of storage, the environment should be controlled to prevent the oxidation of MXenes. It would be ideal to study the oxidation process of the MXenes at all stages of the research with in-situ electrochemical-spectroscopic techniques to understand the effect oxidation on performance and vice versa. For the metallotetrapyrazinoporphyrazine involved in the intercalation study, the chemical of highest should be commercially obtained and thoroughly characterized before any electrochemical performance study is undertaken. The construction of cells, asymmetrical systems should be considered for wider operating potential cells.

Future Perspectives

The combination of MXenes and MN4 chemistries should be intensively researched in the electrocatalysis field for hydrogen evolution reaction and oxygen reduction reaction application. In supercapacitor studies, an involvement of carbonaceous or highly capacitive materials can well synergize with the highly pseudocapacitive nature of MXene-MN4 composites.